Dissertation

Modeling, Analysis, and Control of High Thrust Tubular Magnetic Geared Linear Motor

(高推力円筒磁気ギア内蔵リニアモータのモデル化、解析および制御)

by

Nguyen Duc Khuong
(グエンドゥッククオン)

Dissertation submitted to the
Department of Mathematics, Physics, Electrical Engineering and Computer Science
In partial fulfillment of the requirements
For the Ph.D. degree in
Electrical and Computer Engineering

Graduate School of Engineering Science
Yokohama National University

Advisor:
Associate Professor Tomoyuki Shimono

September 2023

Declaration

I hereby declare that I am the sole author of this bona fide Doctoral Thesis entitled **"Modeling, Analysis, and Control of High Thrust Tubular Magnetic Geared Linear Motor"**. This is a true copy of the thesis, including any required final revisions, as accepted by my examiners.

I hereby consent to my doctoral dissertation being registered and published in the YNU Repository in accordance with the *YNU Repository Guidelines*. I also consent to the National Die Library receiving a copy of the published file from the YNU Repository for the purpose of archiving and providing it for public viewing within the library facilities.

I hereby confirm that the details quoted or reprinted within the doctoral dissertation are not in violation of the Copyright Atc.

Yokohama, Wednesday, September 6, 2023

Nguyen Duc Khuong

Members of Ph.D. Dissertation Committee:

- Associate Professor Tomoyuki Shimono, *Yokohama National University.*
- Professor Yasutaka Fujimoto, *Yokohama National University.*
- Professor Kan Akatsu, *Yokohama National University.*
- Associate Professor Takao Tsuji, *Yokohama National University.*
- Associate Professor Takashi Otsuki, *Yokohama National University.*

Abstract

Nowadays, linear actuators have been widely used in industrial systems such as the train propulsion, the aircraft launch system, and the industrial gantry. Therefore, an increasing number of researchers pay attention to linear permanent magnet (LPM) machines. There are various studies aim to achieve high thrust force, high thrust density, and low thrust ripple of LPM motor. Methods such as a double-layer end-iron-free structure that has higher thrust force in the same motor volume, using halbach permanent magnet with a semi-closed structure, the E-core winding topology, double-stator tubular vernier permanent magnet have been proposed.

Beside those solutions, magnetic gear (MG) and magnetic geared motor (MGM) have been proposed to achieve high thrust force from linear system. There are some distinct advantages of MG over the mechanical ones, such as higher reliability, higher efficiency, inherent overload protection, free from maintenance, lower acoustic noise, and physical isolation between input and output shafts. Therefore, MGs are expected to be applied to numerous industrial systems. Various topologies and solutions for computation of flux distribution in magnetic gear have been published. Methods such as circuit-field-motion solution, magnetic circuit modeling, and lumped parameter magnetic circuits technique for tubular magnetic gear (TMG), or the resolution of Laplace's and Poisson's equations for coaxial magnetic gear have been proposed. However, the previous methods focus on model and analysis of magnetic flux densities, thrust force, and force ripple but model for machines control purpose.

In this dissertation, a magnetic geared linear motor which combines a tubular linear motor and a tubular magnetic gear for high thrust force and downsizing of motor is presented. The motor has two movers which attract together through two-way transmission force in comparing with one mover of traditional linear actuators. One mover has higher speed and lower thrust force, meanwhile, another one has lower speed and higher thrust force.

In addition, a mathematical model and solution for flux density distribution will be newly established in this study. In comparison with finite element solution, this method consumes less computing time. In addition, this method provides both radial and axial components of flux densities in comparing with only radial component in previous studies which were applied for tubular structure. Basing on the calculated flux density, force transmission capacity of the MG and the motor thrust force are predicted. The accuracy of the method is confirmed by finite element analysis and experimental results. The predicted results can be used as a simple tool for optimization geometrical parameters of the motor.

Furthermore, this study presented a mathematical model of the motor which aims to control position of the motor's mover. The main idea of the mathematical model is that consider reaction forces between the two movers in their motion equations. A position controller which is applied for the motor is developed. Simulation and experiment are employed to confirm the accuracy of the motor model. The accurately experimental trajectory response results validate the controller performance.

Acknowledgements

This dissertation is the summary of my researches from October 2020 to September 2023 as a member of the Shimono laboratory in Yokohama National University.

I would like to extend my gratitude first and foremost to my thesis advisor Prof. Tomoyuki Shimono, for having accepted me in his laboratory as a doctoral student, and providing me with great opportunities and directions, motivating ideas, and invaluable advice without which this work would not have been possible. He has helped me through extremely difficult times over the course of the analysis and the writing of the dissertation and for that, I sincerely thank him for his confidence in me. In additions, I thank all of my thesis committees for their advice and guidance.

I would like to extend my heartfelt appreciation to all Shimono laboratory members with whom we shared a lot of knowledge forging one another. Particularly, I would like to thank Kaino-san, Kase-san, Kanai-san, Hasegawa-san, Shibata-san, and Hayashi-san who willing supported whenever I faced troubles. I also want to thank Mitutoyo Association for Science and Technology (MAST) for supporting in part of producing the experimental prototype. I would like to thank to Electrical Engineering section, faculty of Electrical and Electronic Engineering, university of Transport and Communications, Vietnam for allowing me to go for doctoral program. Thank to the Kogyokai Scholarship for supporting me a part while I study in Japan.

Especially, I would also like to thank my beloved wife Nguyen Thi Oanh. Thank you for supporting me for everything and especially I can't thank you enough for encouraging me throughout this experience. To my beloved daughter Nguyen Khanh Van, I would like to express my thanks for being such a good girl always cheering me up, she always makes me happy.

Finally, I would like to extend my deepest gratitude to my parents Nguyen Duc Pho, Hoang Thi My without whose love, support, and understanding I could never have completed this doctoral degree. I always remember and head to you wherever I go in my life.

September 2023
Nguyen Duc Khuong

Table of Contents

List of Tables

List of Figures

Chapter 1

Introductions

Chapter 1 presents the detail of background, objective, and approaches of this dissertation. This chapter ends by giving the chapter organization.

1.1 Background

Currently, linear motors have been widely used in industrial systems such as the train propulsion, the aircraft launch system, and the industrial gantry [1–3]. Therefore, linear permanent magnet (LPM) machines have received much attention from researchers. There are various studies aim to achieve high thrust force, high thrust density, and low thrust ripple of LPM motor. Methods such as a double-layer end-iron-free structure that has higher thrust force in the same motor volume [4], using halbach permanent magnet with a semi-closed structure [5, 6], the E-core winding topology [7, 8], double-stator tubular vernier permanent magnet [9–11] have been proposed. Beside those solutions, magnetic gear (MG) and magnetic geared motor (MGM) have been proposed as an advance solution for achieving high thrust force from linear system. In comparing with mechanical gear, MGs provides some distinct advantages. For instant, MGs can achieve higher reliability, higher efficiency, and lower acoustic noise. In addition, MGs do not face with overload circumstantial like mechanical ones. Further more, MGs less required maintenance because the input and output shafts are isolated [12–14]. Because of these above distinct advantages, MGs are expected to replace traditional mechanical ones in numerous industrial systems as an advanced solutions of power transmission.

Various topologies and solutions for calculation of magnetic flux distribution in magnetic gear have been published [15–21]. Basing on the designing, MGs can be classified into two main categories: The first type is the traditional magnetic gears which can be achieved by replacing steel teeth with permanent magnets pole pairs. The second one is flux-modulated magnetic gears which work based on magnetic flux modulation effect. Following, the development of magnetic gears, the disadvantages and advantages of using these technologies will be presented.

1.1.1 Magnetic Gear Based on Mechanical Gear Topology

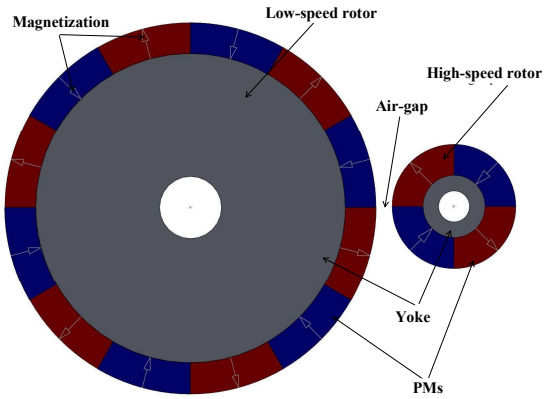

Figure 1.1: Magnetic spur gear [22].

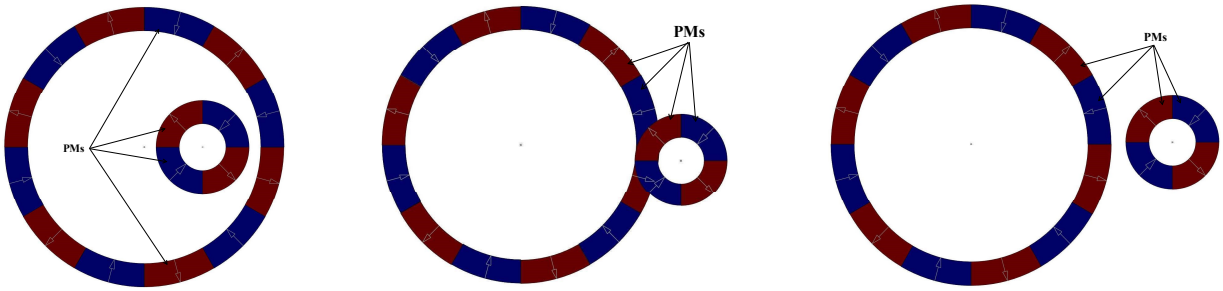

(a) Internal coupling topology

(b) Axial coupling topology

(c) External coupling topology

Figure 1.2: Topologies of magnetic spur gear [24].

The first idea using magnetic material to replace mechanical gear has been applied in mechanical power transmission systems since early decades of the 20th century. At first, these magnetic gears were very similar to mechanical ones. A spur MG which was created by replacing mechanical steel teeth with permanent magnetic pole pairs is shown in Fig. 1.1. In 1941, Faus invented a MG which quite analogy to a mechanical spur gear [22]. However, this topology was not strong enough because of low performance and the weakness of permanent magnetic energy. Thus, it was impossible to widely applied in the industry, even if this topology seemed quite effective. Later, using ferrite magnets to manufacturer a non-contact magnetic gear was proposed by Ikuta *et al.* in 1991 [23]. Fig. 1.2 shows some different topologies that later were developed from a simple parallel-axis MG: Internal coupling topology with radial magnetization direction in Fig. 1.2a, axial magnetization direction coupling topology in Fig. 1.2b, and external coupling topology with radial magnetization direction in Fig. 1.2c [24].

Using the same replacing method, other structures of MG were produced. In 1974, Baermann invented a magnetic worm drive using barium-ferrite magnets as presented in Fig. 1.3a [25]. In 1993, the basic design, working principle, and effectiveness of a new worm magnetic gear topology (Fig. 1.3a) using samarium-cobalt PMs were presented by Tsurumoto and Kikuchi [26]. Later, in 1994, Tsurumoto and Kikuchi also developed magnetic gear which similar to bevel gears (Fig. 1.3b) [27]. To convert rotational to linear motion, a prototype of rack-pinion magnetic gear has been published [28]. Fig. 1.3c shows this rack-pinion topology.

Similar to mechanical planetary gear, a planetary magnetic gear, which has higher power transmission capacity and torque density than previous topologies, has also proposed as shown in Fig. 1.4 [29, 30]. In another research on planetary MG, from simulation results, Huang *et al.*,

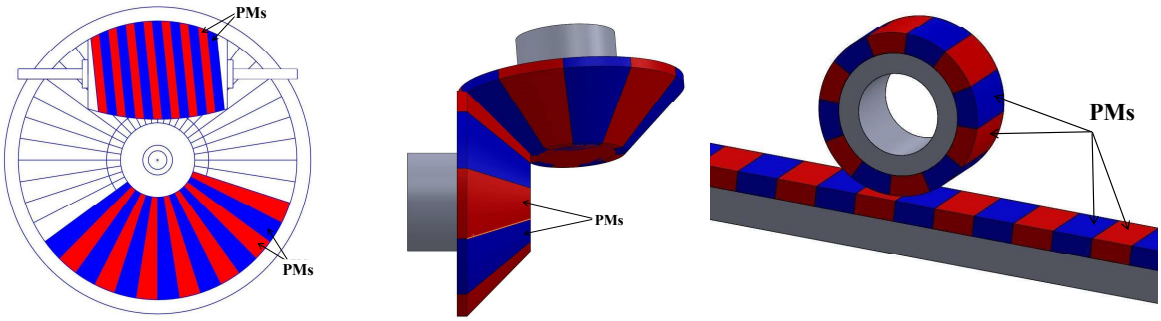

(a) Worm structure [26] (b) Bevel [27] (c) Rack-Pinion structure [28]

Figure 1.3: Some other topologies of MG.

indicated that this planetary gears prototype can be obtained 48.3 kNm/m^3 of torque density in comparison with 100 kNm/m^3 torque density of six planetary gears topology.

In general, MGs can be obtained from mechanical gears by replacing the steel teeth with the permanent magnet poles pairs. These MG topologies possible to transmit mechanisms power without contact between input and output shafts, avoiding the disadvantages of mechanical ones. In addition, these MG technologies are quite acceptable dynamic performances and mechanical characteristics. However, except planetary magnetic gear, the drawback of these topologies is the low torque density because of only some PMs participate simultaneously in transmission of power. Consequently, these topologies are unattractive for large-scale industrial power applications.

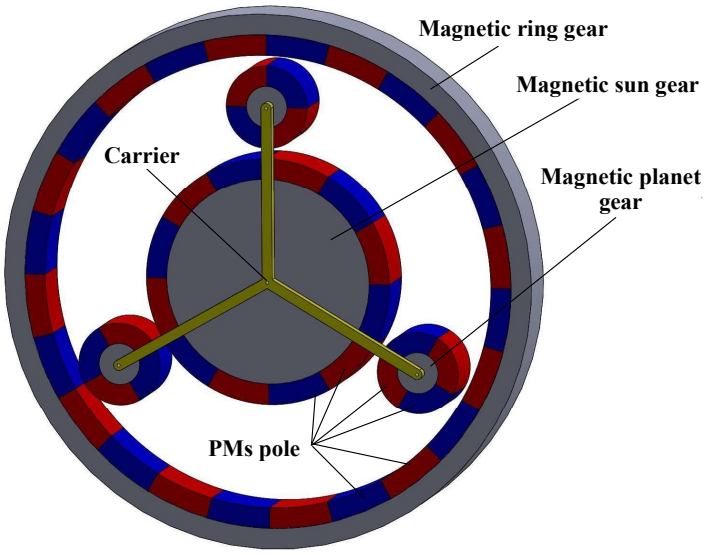

Figure 1.4: Magnetic planetary gear [29].

1.1.2 Flux Modulating Magnetic Gear

In another approach, a new type of MG topology which works basing on flux modulation effect was proposed by Atallah and Howe in 2001 [31]. The design of Atallah and Howe consists of three main parts: a high-speed rotor, a low-speed rotor, and a stationary ring of ferromagnetic

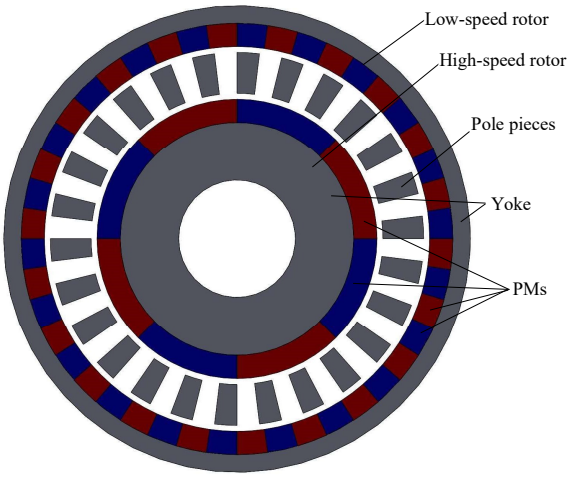

Figure 1.5: Flux modulating magnetic gear [32].

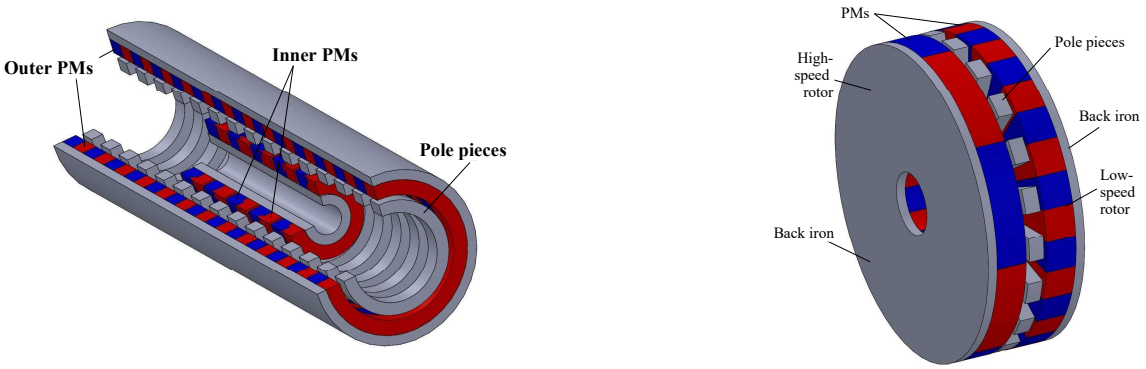

(a) MG with linear structure [36]

(b) MG with axial flux structure [43]

Figure 1.6: Topology with linear and axial flux design of gears.

pole pieces. Both of the two rotors have radially magnetized permanent magnets and iron cores. Pole pieces are placed between the two rotors, formed the modulator. Function of the pole pieces is to modulate the magnetic flux which established by the permanent magnets into different frequency. This new magnetic gear prototype is known as simply flux-modulated or flux-modulated magnetic gear [32]; its basic structure is shown in Fig. 1.5.

Based on this approach, to obtain higher efficiency and better torque density, numerous topologies have been proposed, which aim to optimize the magnetic gear parameters [33–35]. There are two different outstanding configurations are the linear structure and axial flux design as shown in Fig. 1.6a and Fig. 1.6b, respectively.

Fig. 1.6a shows the linear magnetic gear which has a tubular topology [36]. It works similar to operating principle of the coaxial magnetic gear in [37]. According this study, from simulation results, authors pointed that this topology can achieve greater than 1.7MN/m^3 of transmitted force density. On other studies, by combining with a PM linear machine, authors showed that, the magnetic gear with linear structure can achieve amount benefit, and it can be applied for the energy generation from the sea waves application [38–42]. In comparison with tubular topology, there is a ferromagnetic modulated pole pieces which located in the middle of two disk-shaped rotors as represented in Fig. 1.6b [43].

Then, there were many efforts which aim to reduce volume and obtain higher force density

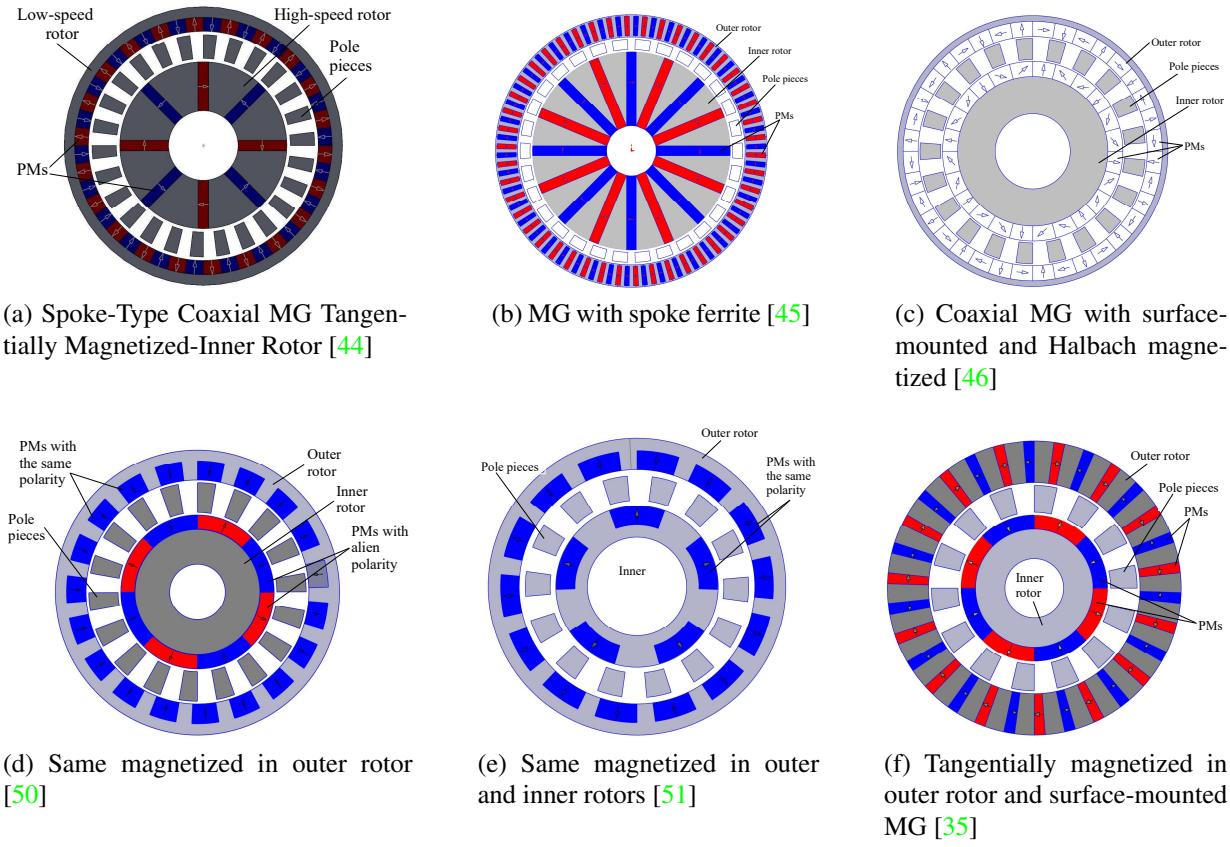

(a) Spoke-Type Coaxial MG Tangentially Magnetized-Inner Rotor [44]

(b) MG with spoke ferrite [45]

(c) Coaxial MG with surface-mounted and Halbach magnetized [46]

(d) Same magnetized in outer rotor [50]

(e) Same magnetized in outer and inner rotors [51]

(f) Tangentially magnetized in outer rotor and surface-mounted MG [35]

Figure 1.7: Coaxial flux-modulated magnetic gear.

by changing direction of the magnetic magnetization and the exploration of new geometric prototype. Rasmussen *et al.* presented measurement and calculation results of a 5.5 gear ratio high performance PM gear as shown in Fig. 1.7a [44]. This topology, the inner rotor is the high speed rotor which configuring of tangential magnetized direction in the rectangular PMs form. However, efficiency for the actual gear was 81% instead of 96% of theoretical. Later, with this same scheme, Uppalapati *et al.* [45] introduced a 1:4.25 ratio, torque density of 239 Nm/L magnetic gearbox using ferrite magnet and Nd-Fe-B magnet flux-focusing to decrease torque ripple as shown in Fig. 1.7b.

In 2010, Jian *et al.* [19,34], used a surface-mounted PM Halbach array for a coaxial MG aims to achieve higher flux intensity and increase flux density of the topology which were proposed in [46,47]. The configure of this topology is shown in Fig. 1.7c. The authors indicated that the MG can increase torque density, decrease iron losses and cogging torque. From FEA results, authors verified that the gear obtained 13% of torque density higher, the maximum transmission torque improved by approximately 7% when comparing to the normal condition.

In 2012, still using halbach array, combing with optimal magnet arrangement and the shape of stationary pole pieces to increase transmission torque, Fujita *et al.* developed a high speed magnetic gear [48]. With this designed, it can provide the powerful (torque of 8 through 15 N.m) and high speed (about 3000 rpm), the transmission torque improved by 15% or more in comparing to the conventional pole pieces.

In 2017, Som *et al.* presented a new type of FCH-MG by incorporating the ferromagnetic flux concentration poles within the Halbach type structure [49]. From experimentally tested, this prototype obtained a 112Nm/L of torque density but it still faced difficult to implement in

practice. In 2009, a new structure of axial magnetic gears was proposed and implemented by

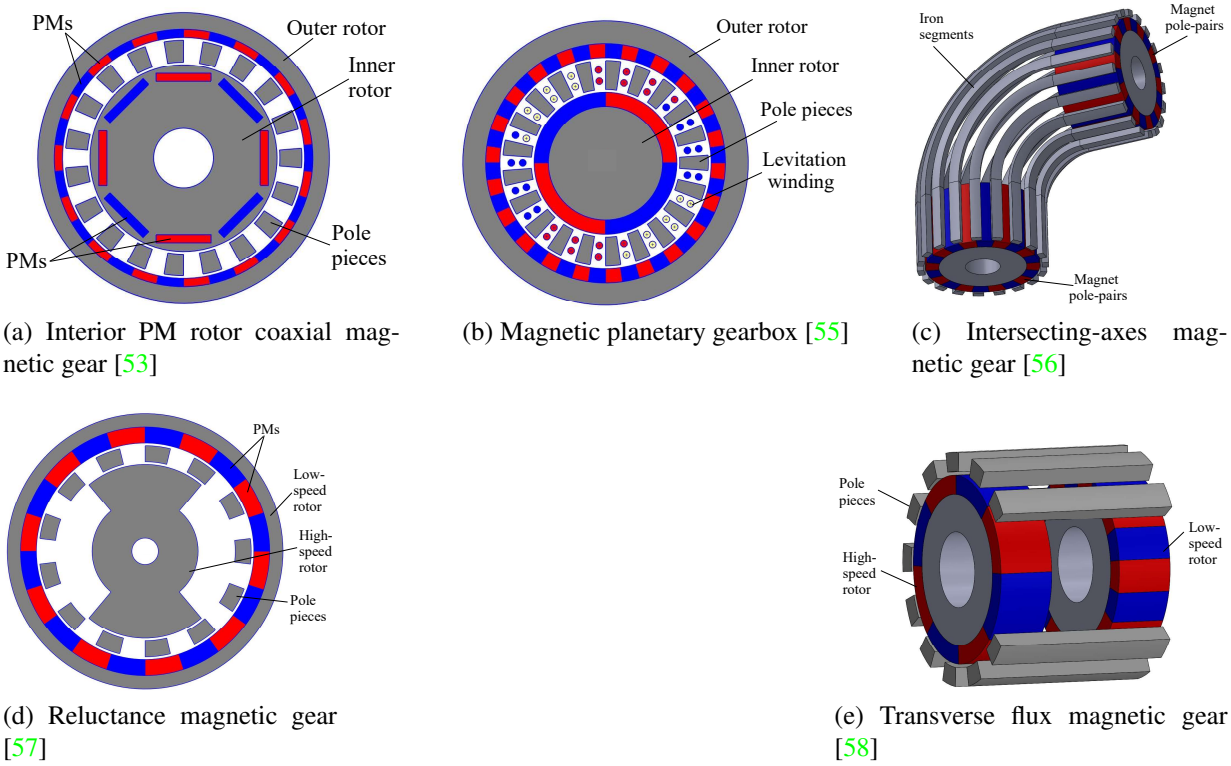

(a) Interior PM rotor coaxial magnetic gear [53]

(b) Magnetic planetary gearbox [55]

(c) Intersecting-axes magnetic gear [56]

(d) Reluctance magnetic gear [57]

(e) Transverse flux magnetic gear [58]

Figure 1.8: Some special structure of flux modulated magnetic gearboxes.

Liu *et al.* as shown in Fig. 1.7d [50]. The proposed gear was designed with gear ratio of 7.33 and optimized by using the three-dimensional finite element analysis (3D-FEA). In comparison with traditional MG, the proposed one can reduce volume by 16.5% but the torque capability decreased by 5.3%. Fig. 1.7e shows the proposed topology with both permanent magnet and consequent poles are employed on the inner and outer rotors by Shen *et al.* [51]. By increasing the effective magnetic flux and offering additional reluctance torque, the MG improved torque density of 24% meanwhile reduced the permanent magnets volume 75% and 80% in the external and the internal rotors, respectively.

Fig. 1.7f shows a tangentially magnetized-outer rotor coaxial MG which was developed from the Rasmussen's topology [44], by Li *et al.* [35]. From 2D FEA results, the study pointed that the gear can decrease ripples torque while increase 25% of torque density than that of conventional topology. In a later study, Jing *et al.* proposed a high torque density and high mechanical properties MG by changing the inner permanent magnet shape and the outer permanent magnet magnetization [52]. From 2D FEA results, the outer rotor torque increased from 74.52 N.m to 140.40 N.m and the inner rotor torque is increased from 12.96 N.m to 24.39 N.m.

By modifying the geometry or arrangement of the MG's components, various coaxial topologies which work basing on flux modulation effect have been proposed. Many studies aim to achieve a high-performance magnetic gear even if some of these topologies do not provide high torque densities. In 2011, Frank *et al.* proposed a concentric planetary MG for renewable energy application [53, 54]. This topology with strengthened stator and interior permanent magnet (IPM) inner rotor, it consist: parallel magnetization PM in rectangular form of inner rotor and reinforced stationary ring as shown in Fig. 1.8a.

Fig. 1.8b shows a 3 kW magnetic planetary gear with gear ratio equals to 9.5 for transmitting power in Helicopter [55]. The gear includes a levitation winding aims to generate an average unbalanced magnetic pull in the air gap. From simulation results, authors showed that suspension winding does not affect on performance and torque transmission. In 2014, Liu *et al.* proposed a novel magnetic gear with intersecting shaft axes as shown in Fig. 1.8c [56]. Basing on special structure, this MG can achieve flexible transmission direction where the axes do not intersect. In 2016, Aiso *et al.* presented a novel reluctance magnetic gear as shown in in Fig. 1.8d [57]. In difference with both PM pole pairs in inner and outer rotor of the other MGs, there is only PM in the outer rotor (low-speed rotor). The inner rotor is the high speed rotor which is constructed by only iron core. This structure make the gear become much more simple. Consequently, this reluctance MG possible to operate in very high speed region. Fig. 1.8e presents the design of a magnetic gear with transversal-flux topology [58]. This structure achieve flexible transmission ratio and large torque.

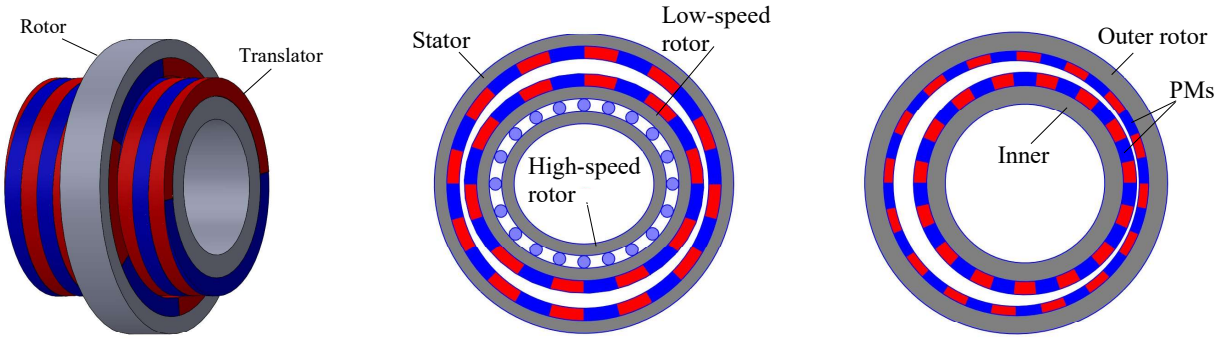

(a) Trans-Rotatory Magnetic gear [59]

(b) Harmonic Magnetic gear [63]

(c) Cycloidal Magnetic gear [65]

Figure 1.9: Some other special magnetic gearboxes.

Some other special topologies such as trans-rotary, a mechanical harmonic, and cycloid MG have been proposed in Fig. 1.9a, Fig. 1.9b, and Fig. 1.9c, respectively. In 2012, Pakdelian *et al.* presented and experimentally analyzed the trans-rotary magnetic gear which was designed to convert linear to rotary motion [59–62]. A magnetic harmonic gear, was proposed by Rens *et al.*, aims to apply for a high gear ratio systems [63, 64]. In addition, a cycloidal MG which can provide an extreme torque density and a very high gearing ratio was designed by Jorgensen *et al.* [65]. Summary of the main MG technologies illustrated in Table 1.1.

Table 1.1: Summary on magnetic gear topologies

MG Topology	Performance	Gear ratio	Figure
Linear MG	Transmitted force density ~ 1.7 MN/m^3	3.25	Fig. 1.6a
Axial MG	Torque density: 70–289.8 kNm/m^3	5.75	Fig. 1.6b
Spoke-Type Coaxial MG Tangentially Magnetized-Inner Rotor	Torque density: 92 kNm/m^3	5.5	Fig. 1.7a
Spoke Ferrite MG	Torque density: 84.4 kNm/m^3	1:4.25	Fig. 1.7b
Coaxial MG with surface mounted and Halbach magnetized	Torque density: 110.7 kNm/m^3	4.25	Fig. 1.7c
Coaxial MG Same-Polarity Magnetized-Outer Rotor	Torque density: 55.8 kNm/m^3	7.33	Fig. 1.7d
Same magnetized in outer and inner rotors	Torque density: 35.4 kNm/m^3	17:5	Fig. 1.7e
Tangentially magnetized in outer rotor and surface-mounted MG	Torque density: 98.1 kNm/m^3	5.5	Fig. 1.7f
Interior PM rotor coaxial magnetic gear	Torque density: 64 kNm/m^3	5.5	Fig. 1.8a
Reluctance MG	Torque density: 29.4 kNm/m^3	0.125	Fig. 1.8d
Transverse Flux MG	Torque density: 80.6 kNm/m^3	6.5	Fig. 1.8e
Trans-Rotatory MG	Force density: 10 MN/m^3	~156	Fig. 1.9a
Magnetic Harmonic Gear	Torque density: 110 kNm/m^3	20	Fig. 1.9b
Cycloidal MG	Torque density: 141.9 kNm/m^3	44/42	Fig. 1.9c

1.2 Objectives

There are two main objectives of this dissertation. They are stated as follows:

- Solution for flux density in both axial and radial components in TMGLM.
- Modeling and control the TMGLM.

1.3 Approach

In this dissertation, a solution for flux density distribution in TMGLM which based on solving Laplace and Poisson equations was newly established. In addition, mathematical model that consider reaction forces between the two movers in their motion equations and a motion controller were developed.

1.4 Chapter Organization

This doctoral dissertation consists of five chapters described as follows.

- Chapter 1 - Introduction and background of my research were summarized.
- Chapter 2 - The structure and working principle of the TMGLM are presented.
- Chapter 3 - Mathematical model and solution for flux density distribution will be presented in this chapter. In comparison with finite element method, the presented method consume less computing time. In addition, this method provides both radial and axial components of flux densities in comparing with only radial component in previous studies which were applied for tubular structure. Basing on the calculated flux density, force transmission capacity of the MG and the motor thrust force are predicted. The accuracy of the method is confirmed by finite element analysis and experimental results. The calculated results used to determine the optimization geometrical parameters of the gear.
- Chapter 4 - This chapter presented a solution for modeling of a high thrust tubular magnetic geared linear motor aims to control the motor position. In addition, a controller was developed by comparing PI and DOB methods. From simulation and experimental results, it was verified that the motor model is accurately. Effectiveness of the controller was confirmed by experimental results under both cases of pulse and sinusoidal references.
- Chapter 5 - Finally, this dissertation is summarized.

Chapter 2

Tubular Magnetic Geared Linear Motor

2.1 Abstract

In this chapter, structure and working principle of the Tubular magnetic geared linear motor will be explained, briefly.

2.2 Structure of the TMGLM

Fig. 2.1a, Fig. 2.1b, and Fig. 2.2 show the 3-D, 2-D, and manufacturing structure of the TMGLM, respectively. The TMGLM consists of four main parts: Inner PMs, outer PMs, pole pieces, and three-phase coils.

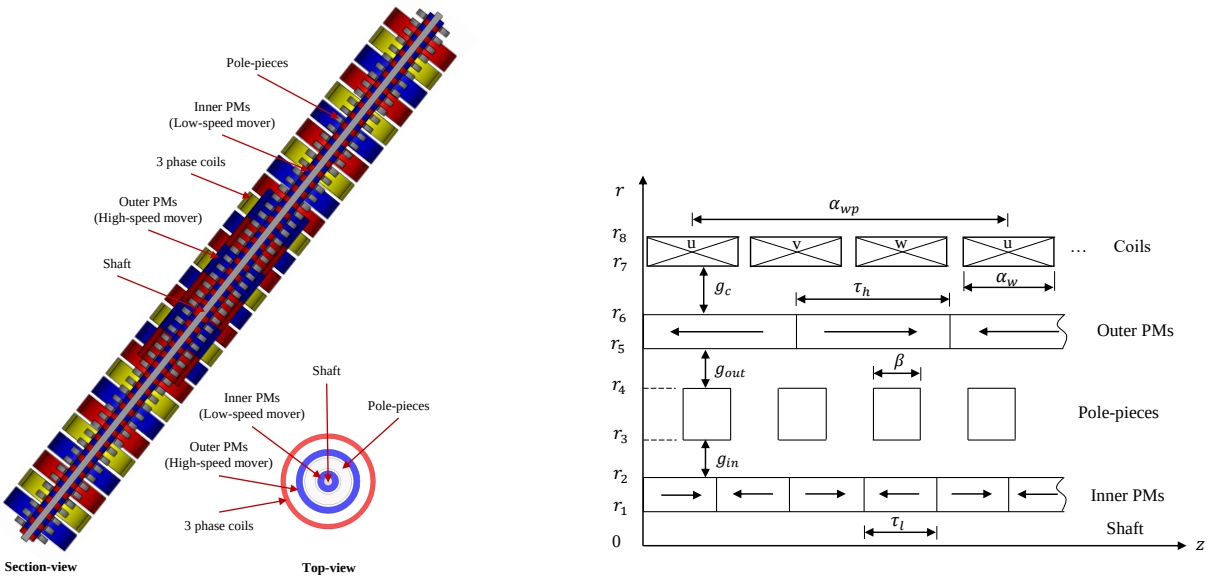

(a) 3-D model (b) 2-D model

Figure 2.1: Structure of the TMGLM

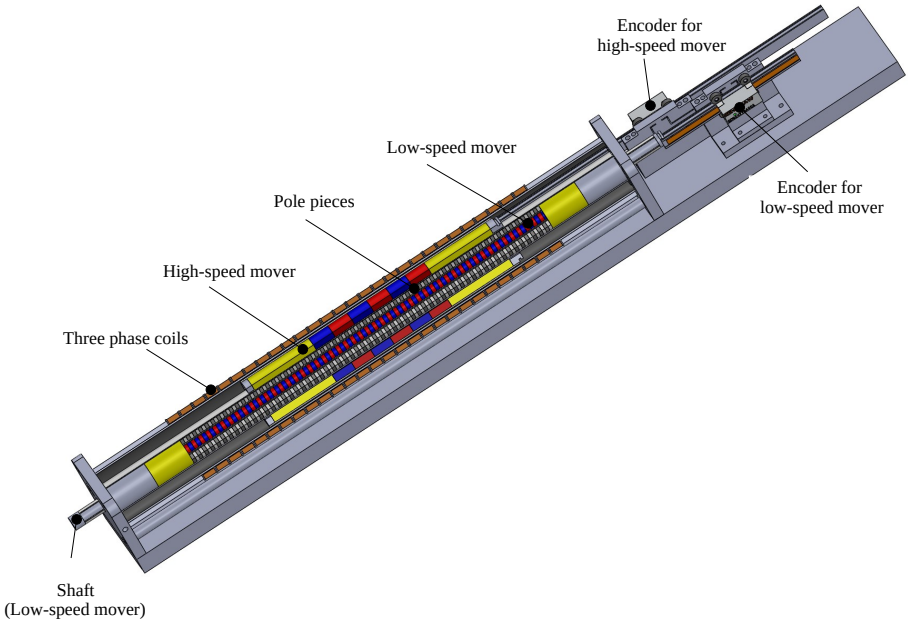

Figure 2.2: Manufacturing topology.

- The inner PMs represent the low-speed mover of the gear. The mover was made from Neodymium magnet N-42 and it has inner diameter, outer diameter, and thickness equal to 4.0 mm, 10.0 mm, and 3.75 mm, respectively. Stroke length of the low-speed mover equals to 40.0 mm. High thrust force is generated on the low-speed mover as the output force of the motor. To measure displacement of the mover, an encoder is assembled as shown in Fig. 2.3a. The encoder consists of a scale and a reader. The scale part is connected to the low-speed mover and guided by 4 rollers which ensuring the scale can move with the same velocity and direction of the mover. The reader part is connected to the controller (PE-Expert4) aims to feedback position of the mover when motor working. On the opposite side where assembled the encoder, a force sensor is configured to achieve thrust on the inner mover, as illustrated in Fig. 2.3b. Fig. 2.3c shows the manufacturing draw of the mover.

- The outer PMs represent high-speed mover of the magnetic gear. The mover was made from Neodymium magnet N-42 and it has inner diameter, outer diameter, and thickness equal to 24.0 mm, 30.0 mm, and 20.0 mm, respectively. Stroke length of high-speed mover equals to 215.0 mm. Similarly to the inner mover, the outer mover also consists of an encoder aims to feedback its displacement. Fig. 2.4a illustrates how the scale and reader parts of the encoder setups on the experiment model. The outer mover is connected to an extension part which exerted to encoder scale part. Two above and two bellow rollers guide the direction for the extension part. In the case of response thrust on the high-speed mover, a force sensor will be inserted as shown in Fig. 2.4b. This configuration provides an ability to measure force when the mover is stationary, not for moving circumstances. The retaining sleeve plays a role as an orientation part for the high-speed mover as show in Fig. 2.4c.

- The pole pieces play a role as a modulation effect part. In the experiment motor, the pole pieces were made from steel S45C and has inner diameter, outer diameter, and thickness equal to 12.0 mm, 22.0 mm, 3.16 mm, respectively. The B-H characteristic of S45C steel and manufacturing draw of the pole pieces are shown in Fig. 2.5a and Fig. 2.5b.

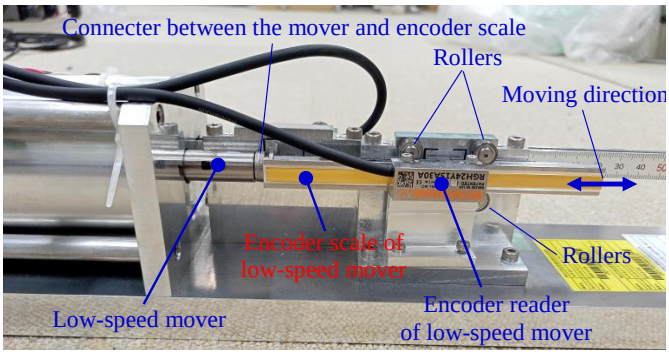

(a) Setup for low-speed mover's encoder

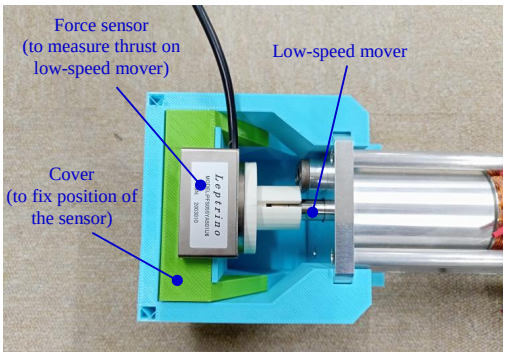

(b) Setup to measure force on the low-speed mover

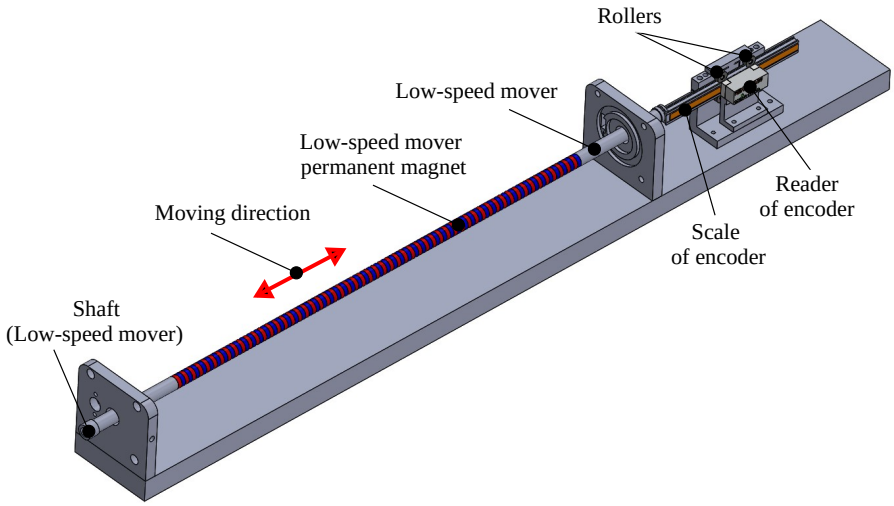

(c) 3D view of low-speed mover

Figure 2.3: The low-speed mover.

- The coils are three phase windings. They were made from copper and have its inner diameter, outer diameter, and thickness equal to 53.0 mm, 57.5 mm, and 11.33 mm, respectively. There are total nine coils in each phase, and all of them are connected to the power supply when the motor operates.

The TMGLM can be consider as a combination of a tubular linear motor and a tubular magnetic gear as shown in Fig. 2.6. The tubular linear part consists of three phase coils and outer PMs. Meanwhile, the inner PMs, the pole pieces, and the outer PMs are combined to form a magnetic gear. There are air-gaps with a length of 1 mm between the high-speed mover and the pole pieces, as well as between the low-speed mover and the pole pieces. Parameters of the TMGLM are specified in Table 2.1.

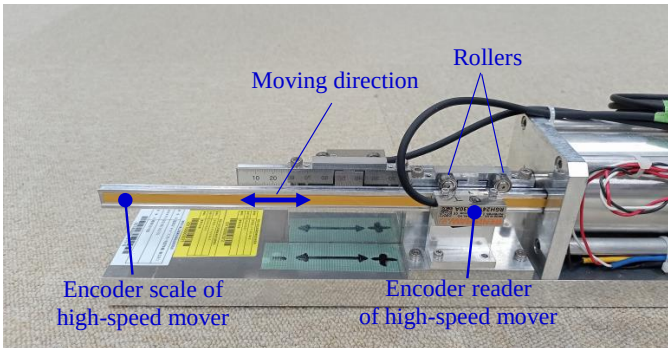

(a) Setup for high-speed mover's encoder

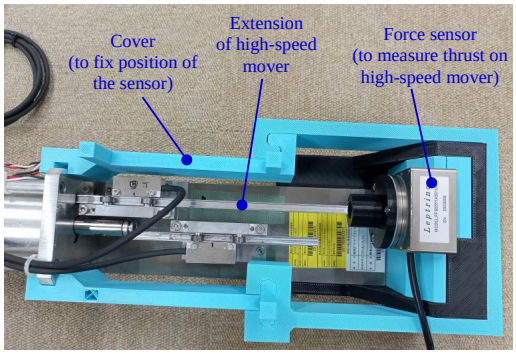

(b) Setup to measure force on the high-speed mover

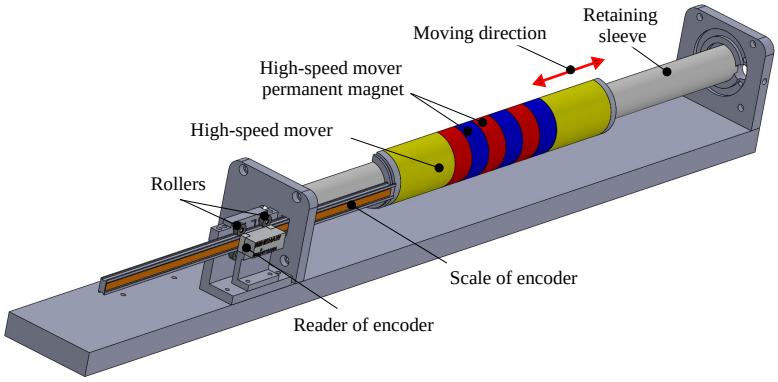

(c) 3D view of high-speed mover

Figure 2.4: The high-speed mover.

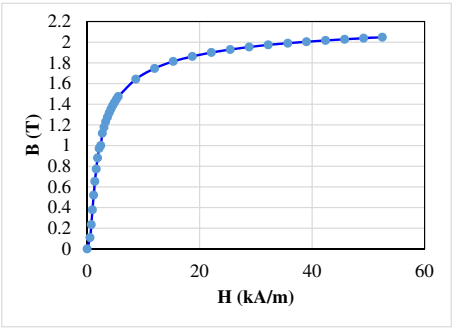

(a) Magnetic property of S45C steel

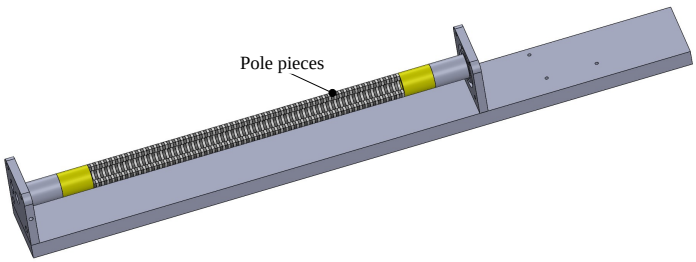

(b) 3D view of the pole pieces

Figure 2.5: The pole pieces.

Table 2.1: Parameters of the TMGLM

Symbol	Meaning	Value
r_1	Inside radius of inner PMs	2.0 mm
r_2	Outside radius of inner PMs	5.0 mm
τ_l	Pole pitch of inner PMs	3.75 mm
r_3	Inside radius of pole pieces	6.0 mm
r_4	Outside radius of pole pieces	11.0 mm
β	Thickness of pole pieces	3.16 mm
r_5	Inside radius of outer PMs	12.0 mm
r_6	Outside radius of outer PMs	15.0 mm
τ_h	Pole pitch of outer PMs	20.0 mm
r_7	Inside radius of winding coil	26.5 mm
r_8	Outside radius of winding coil	28.75 mm
α_w	Thickness of a single coil	11.33 mm
g_{in}	Inner air gap length of the magnetic gear	1.0 mm
g_{out}	Outer air gap length of the magnetic gear	1.0 mm
g_c	Air gap length between high-speed mover and the coils	11.5 mm
α_{wp}	Distance between two coil groups in one phase	34.33 mm
L	Active length	120 mm
B_{rem}	Remanence of PMs	1.15 T
N_{hpm}	Number of high-speed mover pole pairs	3
N_{lpm}	Number of low-speed mover pole pairs	16
N_{pp}	Number of ferromagnetic pole pieces	19
N_w	Number coils of each phase	9
N_c	Number of turns per stator coil	90
F_{max}	Maximal thrust force	103.41 N
L_{lmax}	Stroke length of low-speed mover	40.0 mm
L_{hmax}	Stroke length of high-speed mover	215.0 mm
R_s	Winding resistance of each phase	11.0 Ω
L_s	Winding inductance of each phase	8.5 mH
m_h	Mass of the high-speed mover	0.3 Kg
m_l	Mass of the low-speed mover	0.5 Kg
ψ_p	Permanent magnet flux linkage	0.165 Wb

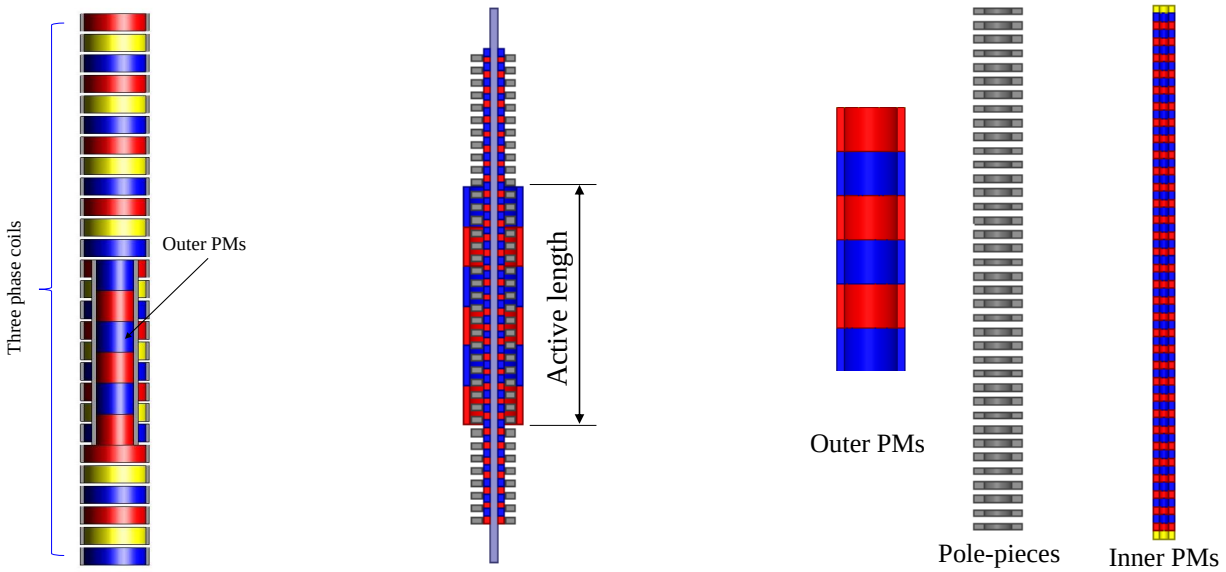

(a) Linear motor part (b) MG part (c) Components of MG

Figure 2.6: Components of the TMGLM

2.3 Working Principle of the TMGLM

As described about structure of the TMGLM in Section 2.2, the machine can be considered as contributing from a tubular linear motor and a tubular magnetic gear together. The linear motor part works as a conventional tubular linear motor. When current is applied to the coils, a thrust force is generated on the high-speed mover (Outer PMs). This force makes the high-speed mover travels along z-axis. Meanwhile, the magnetic gear part works basing on the magnetic flux modulation effect. This MG can be worked under 2 different modes. The first case, the pole pieces are fixed while the outer and inner PMs are allowed to travel. In this mode, the gear ratio G_r is given by:

$$G_r = -\frac{N_{lpm}}{N_{hpm}} \tag{2.1}$$

Minus sign in (2.1) denotes that the two movers have opposite direction.

Secondly, if the inner mover is held on stationary, the outer PMs and pole pieces are allowed to move, the gear ratio is given by

$$G_r = \frac{N_{pp}}{N_{lpm}} \tag{2.2}$$

In this operating mode, the outer mover and pole pieces have the same direction. To obtained maximal transmission force, under active length, the relationship among three type of segments should follow as:

$$N_{pp} = N_{hpm} + N_{lpm} \tag{2.3}$$

where: N_{pp} denotes number of pole pieces; N_{hpm} is inner mover pole pairs number; N_{lpm} is outer mover pole pairs number.

For the experimental motor in this thesis, stationary part is the pole pieces and the active ferromagnetic pole piece number $N_{pp} = 19$, the active poles on the high-speed mover of the outer PMs $N_{hpm} = 3$, and the active poles on the low-speed mover of the inner PMs $N_{lpm} = 16$. Thus, the ratio the magnetic gear part is obtained as $G_r = 16/3$. As a consequence, the low and high-speed movers travel in opposite directions. The output force which exerted on the low-speed mover, can be achieved by 16/3 times greater than that on the high-speed mover. The frequency of the current flowing in the three-phase coil determines the synchronous velocity of the high-speed mover.

2.4 Summary

This chapter briefly explains the structure and working principle of the TMGLM which can generate high thrust force for linear motion. For specification parameters, MG of the motor has gear ratio equals to 16/3; maximal thrust force equals to 103.4 N; output stroke length equals to 40.0 mm. For working principle, a thrust force is generated on the outer PMs when current is applied to the coils. The magnetic flux which excited by outer PMs is modulated by the pole pieces; the amplified flux attracts the magnetic flux excited by inner PMs. Thus, a thrust force is generated on the inner PMs. Similarly, a reaction force which exerts on the outer PMs is produced when inner PMs travels, through pole pieces. In this topology, under active length, number pole pairs of the outer PMs, pole pieces, and inner PMs equal to 3, 19, and 16, respectively. Consequently, the inner PMs mover has slower speed but it can generate higher thrust force than outer PMs do.

Chapter 3

Magnetic Flux Density Distribution and Thrust Force

3.1 Abstract

Flux density distribution in the air-gap and thrust force play an important role to advance the design and development of new generation motors. Various methods for this problem have been proposed. As for coaxial magnetic gear, the resolution of Laplace and Poisson equations solution has been introduced [18, 19]. For tubular magnetic gear (TMG), there were several methods such as circuit-field-motion solution [15], magnetic circuit modeling [66], and lumped parameter magnetic circuits technique [17] have been proposed. However, the previous methods which were applied for TMG, only can calculate radial component of flux density. In this section, basing on Laplace's equation in the air- gap region and Poisson's equation in the permanent magnet region, general solution for flux density of the magnetic gear is calculated. Then, particular solution for magnetic flux respect with the topology of the tubular magnetic gear in this study is predicted by solving boundary conditions. In addition, maximal force that the gear can be transmitted is also calculated based on the predicted flux density. Further mover, thrust force exerted on the high speed mover which generated by the three-phase coils are calculated. The maximal predicted forces on the movers are important parameters to design the controller in the next section. In comparison with previous methods, the solution in this study is solved in cylindrical coordinates and applied for TMG. The method provides both radial and axial components of flux densities. The calculated flux densities are compared with FEA results to confirm the accuracy of the predict method. Hence, the force transmission and thrust force are experimentally studied to verify the calculated results.

3.2 Mathematical Modeling of the Tubular Magnetic Gear

3.2.1 2-D Model of the TMG

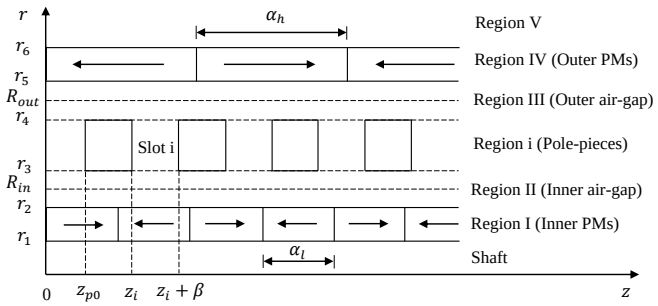

Figure 3.1: 2-D model of tubular magnetic gear.

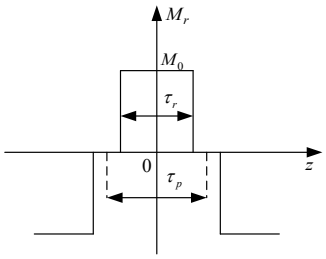

Figure 3.2: Magnetization.

The flux density predicted method is based on the 2-D magnetic gear model in cylindrical coordinates as shown in Fig. 3.1. The magnetic gear can be divided into total six regions: regions I and IV are the PM regions; regions II, III, V, and slot-i are the air gap regions.

The governing partial differential equations in each region are as follows [13].

$$\begin{cases} \nabla^2 A = -\mu_0 \nabla \times M & \text{In PMs regions (Poisson equation)} \\ \nabla^2 A = 0 & \text{In air-gap regions (Laplace equation)} \end{cases} \tag{3.1}$$

where A is the magnetic potential vector, μ_0 is vacuum permeability, and M is the magnetization vector which can be expressed as follows.

$$\vec{M} = M_r \vec{e_r} + M_z \vec{e_z} \tag{3.2}$$

In a cylindrical structure, the magnetization vector $\vec{M}$ has only M_r component in the z directions as shown in Fig. 3.2. In addition, M_r is a non-continuous function with a period of $2\tau_p$; thus, it can be represented as a harmonic expansion [67].

$$M_r = \sum_{n=1}^{\infty} \frac{4B_{rem}}{\mu_0 \pi (2n-1)} \sin\left(\frac{\pi(2n-1)}{2}\alpha_p\right) \cos(k_n z) \tag{3.3}$$

where $\alpha_p = \tau_r/\tau_p$ and $k_n = (2n-1)\pi/\tau_p$. In this research $\tau_r = \tau_p$.

The position z_i of the $i-th$ slot as shown in Fig. 3.1 is defined as follows.

$$\begin{cases} z_i = (2i-1)\beta + z_{p0} \\ 1 \le i \le N_{pp} \\ -\beta \le z_{p0} \le 0 \end{cases} \tag{3.4}$$

where z_{p0} denotes the initial position of the ferromagnetic pole pieces.

To calculate the flux density distribution in each region, Laplace equation (in the air gap regions) and Poisson equation (in PM regions) are solved directly using the separation of variables method as follows.

3.2.2 Solution for Laplace Equation

From Laplace equation in the air gap regions (region II, III, V and slot i):

$$\nabla^2 A = 0 \tag{3.5}$$

In cylindrical coordinates (3.5) can be written as follows.

$$\frac{\partial^2 A}{\partial z^2} + \frac{1}{r}\frac{\partial}{\partial r}(r\frac{\partial A}{\partial r}) - \frac{A}{r^2} = 0 \tag{3.6}$$

Using method of separation variables, assuming that

$$A = R(r)\,Z(z) \tag{3.7}$$

Substituting (3.7) into (3.6), obtained

$$\frac{1}{Z(z)}\frac{\partial^2 Z(z)}{\partial z^2} + \frac{1}{R(r)\,r}\frac{\partial R(r)}{\partial r} + \frac{1}{R(r)}\frac{\partial^2 R(r)}{\partial r^2} - \frac{1}{r^2} = 0 \tag{3.8}$$

Separating variables for (3.8), obtained

$$\begin{cases} \frac{1}{Z(z)}\frac{\partial^2 Z(z)}{\partial z^2} = -k^2 \\ \frac{1}{R(r)r}\frac{\partial R(r)}{\partial r} + \frac{1}{R(r)}\frac{\partial^2 R(r)}{\partial r^2} - \frac{1}{r^2} = k^2 \end{cases} \tag{3.9}$$

Or

$$\begin{cases} Z'' + k^2 Z = 0 \\ R'' + \frac{1}{r}R' - \frac{1}{r^2}R - k^2 R = 0 \end{cases} \tag{3.10}$$

- Solving $Z'' + k^2 Z = 0$ has solution

$$Z = C\sin(kz) + D\cos(kz) \tag{3.11}$$

  where C and D are integral constants.

- Solving $R'' + \frac{1}{r}R' - \frac{1}{r^2}R - k^2 R = 0$
  Or

$$r^2 R'' + rR' - \left(r^2 k^2 + 1\right)R = 0 \tag{3.12}$$

  Assuming $x = kr; dx = kdr; dx^2 = dx * dx = k^2 dr^2$, (3.12) leads to

$$x^2 R'' + xR' - \left(x^2 + 1\right)R = 0 \tag{3.13}$$

  (3.13) is the modified Bessel function and has solution as follows.

$$R = E.I_1(x) + F.K_1(x) \tag{3.14}$$

  Or

$$R = E.I_1(kr) + F.K_1(kr) \tag{3.15}$$

where $I_1(kr)$ is the modified Bessel function of the first kind for order one; $K_1(kr)$ is modified Bessel function of the second kind for order one; E and F are integral constants.

Substituting (3.11) and (3.15) into (3.7), obtained

$$A = \left\{C.E.I_1(kr) + C.F.K_1(kr)\right\}\sin(kz) + \left\{D.E.I_1(kr) + D.F.K_1(kr)\right\}\cos(kz) \tag{3.16}$$

Because the axial component of flux density is antisymmetry on $z = 0$, so $B_z\big|_{z=0} = 0$, it leads to $D.E = 0$ and $D.F = 0$.

Finally obtained solution for Laplace equation as follows.

$$A = \left\{aI_1(kr) + bK_1(kr)\right\}\sin(kz) \tag{3.17}$$

In fourier series

$$A = \sum_{n=1}^{\infty}\{a_nI_1(k_nr) + b_nK_1(k_nr)\}\sin(k_nz) \tag{3.18}$$

where a_n and b_n are integral constants that can be determined by solving the boundary conditions.

3.2.3 Solution for Poisson Equation

From Poisson equation in the magnet regions (region I and IV):

$$\nabla^2 A = -\mu_0 \nabla \times M \tag{3.19}$$

Poisson equation in the PM regions can be written in cylindrical coordinates as follows.

$$\frac{\partial^2 A}{\partial z^2} + \frac{1}{r}\frac{\partial}{\partial r}(r\frac{\partial A}{\partial r}) - \frac{A}{r^2} = -\mu_0 \nabla \times M \tag{3.20}$$

General solution for (3.20) is

$$A = \sum_{n=1}^{\infty}\left\{\left[a_nI_1(k_nr) + b_nK_1(k_nr)\right]\sin(k_nz) + S\ (r,z)\right\} \tag{3.21}$$

where $\sum_{n=1}^{\infty}\left[a_nI_1(k_nr) + b_nK_1(k_nr)\right]\sin(k_nz)$ is the general solution of Laplace equation $\nabla^2 A = 0$ and $S\,(r,z)$ is a particular solution of Poisson equation (3.20)

Using method of separation variables, assuming that

$$S\,(r,z) = R(r).Z(z) \tag{3.22}$$

Substituting M from (3.3) into (3.20), obtained

$$\frac{\partial^2 A}{\partial z^2} + \frac{1}{r}\frac{\partial}{\partial r}(r\frac{\partial A}{\partial r}) - \frac{A}{r^2} = -\mu_0 \frac{4B_{rem}}{\mu_0\pi(2n-1)}\sin\left(\frac{\pi(2n-1)}{2}\alpha_p\right)(-k.sin(kz)) \tag{3.23}$$

Substituting (3.22) into (3.23), we have

$$\frac{1}{Z(z)}\frac{\partial^2 Z(z)}{\partial z^2}+\frac{1}{R(r)\,r}\frac{\partial R(r)}{\partial r}+\frac{1}{R(r)}\frac{\partial^2 R(r)}{\partial r^2}-\frac{1}{r^2} = \frac{1}{R(r)Z(z)}\frac{4B_{rem}}{\tau_p}\sin\left(\frac{\pi(2n-1)}{2}\alpha_p\right)\sin(kz) \quad (3.24)$$

Assuming

$$P_n = \frac{4B_{rem}}{\tau_p}\sin\left(\frac{\pi(2n-1)}{2}\alpha_p\right) \quad (3.25)$$

Now, (3.24) becomes

$$\frac{1}{Z(z)}\frac{\partial^2 Z(z)}{\partial z^2}+\frac{1}{R(r)\,r}\frac{\partial R(r)}{\partial r}+\frac{1}{R(r)}\frac{\partial^2 R(r)}{\partial r^2}-\frac{1}{r^2} = \frac{1}{R(r)Z(z)}P_n\sin(\mathrm{kz}) \quad (3.26)$$

Assuming

$$\frac{1}{Z(z)}\frac{\partial^2 Z(z)}{\partial z^2} = -k^2 \quad (3.27)$$

(3.27) has solution as

$$Z = sin(kz) \quad (3.28)$$

Substituting (3.27) and (3.28) into (3.26), we have

$$\frac{1}{R}R'' + \frac{1}{Rr}R' - \frac{1}{r^2} - k^2 = \frac{1}{R}P_n \quad (3.29)$$

Or

$$r^2R'' + rR' - (r^2k^2 + 1)R = r^2P_n \quad (3.30)$$

(3.30) is the modified Struve function, thus the solution for it is

$$R = \frac{\pi L_1(kr)}{2k^2}P_n \quad (3.31)$$

where $L_1(kr)$ is the modified Struve function for the first order.
Next, substituting (3.28) and (3.31) into (3.22), we have

$$S = R.Z = \frac{\pi L_1(kr)}{2k^2}P_n\sin(kz) \quad (3.32)$$

Finally, the general solution for Poisson equation (3.20), in fourier series, can be obtained as follows.

$$A = \sum_{n=1}^{\infty}\left\{a_nI_1(k_nr) + b_nK_1(k_nr) + \frac{\pi L_1(k_nr)}{2k_n^2}P_n\right\}\sin(k_nz) \quad (3.33)$$

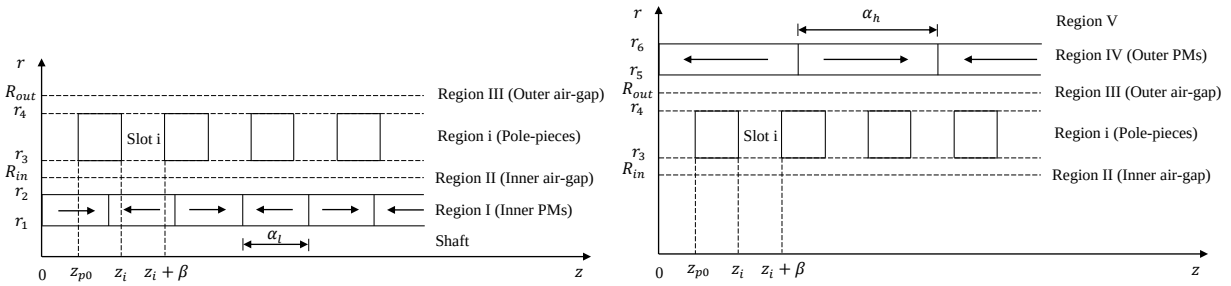

(a) Inner mover and pole pieces

(b) Outer mover and pole pieces

Figure 3.3: 2-D model of movers and pole pieces.

3.2.4 Magnetic Flux Density Distribution

The magnetic flux density B can be determined from the magnetic potential vector A as follows.

$$B = \nabla \times A \tag{3.34}$$

For radial B_r and axial B_z components of magnetic flux density

$$B_r = -\frac{\partial A}{\partial z}; B_z = \frac{1}{r}\frac{\partial}{\partial r}(rA) \tag{3.35}$$

In the air gap regions (regions II, III, and V and slot i), from (3.18) and (3.35), we have

$$\begin{cases} B_r = \sum_{n=1}^{\infty} -\{a_n I_1(k_n r) + b_n K_1(k_n r)\}\cos(k_n z) \\ B_z = \sum_{n=1}^{\infty} \{a_n I_0(k_n r) - b_n K_0(k_n r)\}\sin(k_n z) \end{cases} \tag{3.36}$$

where $I_0(k_n r)$ is the modified Bessel function of the first kind for order zero, and $K_0(k_n r)$ is the modified Bessel function of the second kind for order zero.
In the PM regions (regions I and IV), from (3.33) and (3.35), we obtain the solution for flux density as follows.

$$\begin{cases} B_r = \sum_{n=1}^{\infty} -\left\{a_n I_1(k_n r) + b_n K_1(k_n r) + \frac{\pi L_1(k_n r)}{2k_n^2} P_n\right\}\cos(k_n z) \\ B_z = \sum_{n=1}^{\infty} \left\{a_n I_0(k_n r) - b_n K_0(k_n r) + \frac{\pi L_0(k_n r)}{2k_n^2} P_n\right\}\sin(k_n z) \end{cases} \tag{3.37}$$

where $L_0(k_n r)$ is the modified Struve function for order zero. (3.36) and (3.37) present general solution for flux densities distribution in air-gap and PMs regions.

To predict the flux densities in the inner and outer air gaps of the model in Fig. 3.1, the outer PMs and inner PMs are removed as shown in Fig. 3.3(a) and Fig. 3.3(b), respectively.

For the model in Fig. 3.3(a), from the general solution for Laplace equation in (3.36) and for Poisson equation in (3.37), we have

- Magnetic flux density distribution in Region I.

$$\begin{cases} B^I_{r\_in} = \sum_{n=1}^{\infty} -\left\{a^I_n I_1(k_n r) + b^I_n K_1(k_n r) + \frac{\pi L_1(k_n r)}{2k_n^2} P_n\right\}\cos(k_n z) \\ B^I_{z\_in} = \sum_{n=1}^{\infty} \left\{a^I_n I_0(k_n r) - b^I_n K_0(k_n r) + \frac{\pi P_n}{2k_n^2} L_0(k_n r)\right\}\sin(k_n z) \end{cases} \tag{3.38}$$

- Magnetic flux density distribution in Region II.

$$\begin{cases} B^{II}_{r\_in} = \sum\limits_{n=1}^{\infty} -\left\{a^{II}_n I_1(k_n r) + b^{II}_n K_1(k_n r)\right\}\cos(k_n z) \\ B^{II}_{z\_in} = \sum\limits_{n=1}^{\infty} \left\{a^{II}_n I_0(k_n r) - b^{II}_n K_0(k_n r)\right\}\sin(k_n z) \end{cases} \tag{3.39}$$

- Magnetic flux density distribution in Region III.

$$\begin{cases} B^{III}_{r\_in} = \sum\limits_{h=1}^{\infty} -b^{III}_h K_1(k_h r)\cos(k_h z) \\ B^{III}_{z\_in} = \sum\limits_{h=1}^{\infty} -b^{III}_h K_0(k_h r)\sin(k_h z) \end{cases} \tag{3.40}$$

  Note that $I_1(kr)\big|_{r\to\infty} = 0$ and $I_0(kr)\big|_{r\to\infty} = 0$.

- Magnetic flux density distribution in slot-i.

$$\begin{cases} B^{i}_{r\_in} = \sum\limits_{m=1}^{\infty} -\left\{a^{i}_m I_1(k_m r) + b^{i}_m K_1(k_m r)\right\}\cos(k_m z) \\ B^{i}_{z\_in} = \sum\limits_{m=1}^{\infty} \left\{a^{i}_m I_0(k_m r) - b^{i}_m K_0(k_m r)\right\}\sin(k_m z) \end{cases} \tag{3.41}$$

Similarly, solution for magnetic flux densities of the model in Fig. 3.3(b) obtained as follows.

- Magnetic flux density distribution in Region V.

$$\begin{cases} B^{V}_{r\_out} = \sum\limits_{h=1}^{\infty} -b^{V}_h K_1(k_h r)\cos(k_h z) \\ B^{V}_{z\_out} = \sum\limits_{h=1}^{\infty} -b^{V}_h K_0(k_h r)\sin(k_h z) \end{cases} \tag{3.42}$$

- Magnetic flux density distribution in Region IV.

$$\begin{cases} B^{IV}_{r\_out} = \sum\limits_{h=1}^{\infty} -\left\{a^{IV}_h I_1(k_h r) + b^{IV}_h K_1(k_h r) + \frac{\pi L_1(k_h r)}{2k_h^2} P_n\right\}\cos(k_n z) \\ B^{IV}_{z\_out} = \sum\limits_{h=1}^{\infty} \left\{a^{IV}_h I_0(k_h r) - b^{IV}_h K_0(k_h r) + \frac{\pi P_h}{2k_h^2} L_0(k_h r)\right\}\sin(k_n z) \end{cases} \tag{3.43}$$

- Magnetic flux density distribution in Region III.

$$\begin{cases} B^{III}_{r\_out} = \sum\limits_{h=1}^{\infty} -\left\{a^{III}_h I_1(k_h r) + b^{III}_h K_1(k_h r)\right\}\cos(k_h z) \\ B^{III}_{z\_out} = \sum\limits_{h=1}^{\infty} \left\{a^{III}_h I_0(k_h r) - b^{III}_h K_0(k_h r)\right\}\sin(k_h z) \end{cases} \tag{3.44}$$

- Magnetic flux density distribution in slot-i.

$$\begin{cases} B^{i}_{r\_out} = \sum\limits_{m=1}^{\infty} -\left\{a^{i}_m I_1(k_m r) + b^{i}_m K_1(k_m r)\right\}\cos(k_m z) \\ B^{i}_{z\_out} = \sum\limits_{m=1}^{\infty} \left\{a^{i}_m I_0(k_m r) - b^{i}_m K_0(k_m r)\right\}\sin(k_m z) \end{cases} \tag{3.45}$$

- Magnetic flux density distribution in Region II.

$$\begin{cases} B^{II}_{r\_out} = \sum_{n=1}^{\infty} -a^{II}_n I_1(k_n r)\cos(k_n z) \\ B^{II}_{z\_out} = \sum_{n=1}^{\infty} a^{II}_n I_0(k_n r)\sin(k_n z) \end{cases} \tag{3.46}$$

  Note that $K_1(kr)\big|_{r\to 0} = 0$ and $K_0(kr)\big|_{r\to 0} = 0$.

where a_n, b_n, a_h, b_h, a_m and b_m are calculated based on the boundary conditions as shown in Section 3.2.5.

Finally, the magnetic flux densities in the inner and outer air gaps of the MG can be obtained when the nonlinear factor of the magnetic path is ignored, as follows.

$$\begin{cases} B^{II}_r = B^{II}_{r\_in} + B^{II}_{r\_out} \\ B^{II}_z = B^{II}_{z\_in} + B^{II}_{z\_out} \end{cases} \tag{3.47}$$

$$\begin{cases} B^{III}_r = B^{III}_{r\_in} + B^{III}_{r\_out} \\ B^{III}_z = B^{III}_{z\_in} + B^{III}_{z\_out} \end{cases} \tag{3.48}$$

3.2.5 Boundary Condition

To obtain the particular solution for the flux density with respect to the geometry, coefficients a and b from (3.38) to (3.46) need to be employed by solving the boundary conditions. This model has three different types of boundary conditions: Neumann, continuous, and combined boundary condition.

When a region has a surface that is in contact with the soft-magnet material, it has Neumann boundary conditions (the axial magnetic flux strength must be zero, $H_z = 0$). For the continuous boundary condition, the radial component of the magnetic flux density (B_r) as well as the axial component of the magnetic flux strength (H_z) need to be continuous between two regions. If the interface between regions that have an unequal width and/or unequal offsets, a combination of the continuous and Neumann boundary conditions can be applied [68].

Boundary conditions for the model shown in Fig. 3.3(a). Region I (inner PMs) has a surface that contacts the soft-magnet material (shaft) along $r = r_1$. Thus, the Neumann boundary condition holds at $r = r_1$. Axial component of the magnetic flux strength excited by only the inner mover in region I at $r = r_1$ equals to zero.

$$H^{I}_{z\_in}\big|_{r=r_1} = 0 \tag{3.49}$$

Besides, we have

$$\vec{B} = \mu_0\mu_r\vec{H} + \mu_0\vec{M} \tag{3.50}$$

In a cylindrical structure, the magnetization vector $\vec{M}$ has only M_r components as shown in Fig. 3.2. Therefore,

$$B^{I}_{z\_in} = \mu_0\mu_r H^{I}_{z\_in} \tag{3.51}$$

From (3.49) and (3.51), the axial component of the magnetic flux density excited by only the inner mover in region I at $r = r_1$ equals to zero.

$$B^I_{z\_in}\Big|_{r=r_1} = 0 \tag{3.52}$$

Or

$$\mathrm{a}^I_n I_0(k_n r_1) - b^I_n K_0(k_n r_1) + \frac{\pi P_n}{2k_n^2} L_0(k_n r_1) = 0 \tag{3.53}$$

Applying boundary conditions at $r = r_2$, $r = r_3$, and $r = r_4$, we have

- Radial component along $r = r_2$

$$B^I_{r\_in} = B^{II}_{r\_in}\Big|_{r=r_2} \tag{3.54}$$

  Or

$$\mathrm{a}^I_n I_1(k_n r_2) + b^I_n K_1(k_n r_2) - \mathrm{a}^{II}_n I_1(k_n r_2) - b^{II}_n K_1(k_n r_2) + \tfrac{\pi P_n}{2k_n^2} L_1(k_n r_2) = 0 \tag{3.55}$$

- Axial component along $r = r_2$

$$B^{II}_{z\_in} = \frac{B^I_{z\_in}}{\mu_r}\Big|_{r=r_2} \tag{3.56}$$

  Or

$$\mathrm{a}^I_n I_0(k_n r_2) - b^I_n K_0(k_n r_2) - \mu_r \mathrm{a}^{II}_n I_0(k_n r_2) + \mu_r b^{II}_n K_0(k_n r_2) + \tfrac{\pi P_n}{2k_n^2} L_0(k_n r_2) = 0 \tag{3.57}$$

- Axial component along $r = r_3$

$$B^{II}_{z\_in}\Big|_{r=r_3} = \begin{cases} B^i_{z\_in}\Big|_{r=r_3} \forall \mathrm{z} \in [z_i, z_i + \beta] \\ 0 \text{ else} \end{cases} \tag{3.58}$$

  Or

$$\mathrm{a}^{II}_n I_0(k_n r_3) - b^{II}_n K_0(k_n r_3) = \sum_{i=1}^{N_{pp}} \sum_{m=1}^{M} \left[\mathrm{a}^i_m I_0(k_m r_3) - b^i_m K_0(k_m r_3)\right] \kappa(n, m, i) \tag{3.59}$$

  where

$$\kappa(n, m, i) = \frac{2}{\tau_p} \int_{z_i}^{z_i+\beta} \sin(k_m (x - z_i)) \sin(k_n x)\, dx \tag{3.60}$$

- Radial component along $r = r_3$

$$B^{II}_{r\_in}\Big|_{r=r_3} = B^i_{r\_in}\Big|_{r=r_3} \forall \mathrm{z} \in [z_i, z_i + \beta] \tag{3.61}$$

  Or

$$\mathrm{a}^i_m I_1(k_m r_3) + b^i_m K_1(k_m r_3) = \sum_{n=1}^{N} \left[\mathrm{a}^{II}_n I_1(k_n r_3) + b^{II}_n K_1(k_n r_3)\right] \eta(m, n, i) \tag{3.62}$$

  for $i = 1, \ldots, N_{pp}$

  where

$$\eta(m, n, i) = \frac{2}{\beta} \int_{z_i}^{z_i+\beta} \cos(k_n x) \cos(k_m (x - z_i))\, dx \tag{3.63}$$

- Axial component along $r = r_4$

$$B^{III}_{z\_in}\Big|_{r=r_4} = \begin{cases} B^i_{z\_in}\Big|_{r=r_4} \forall z \in [z_i, z_i + \beta] \\ 0 \text{ else} \end{cases} \tag{3.64}$$

Or

$$-b^{III}_h K_0(k_h r_4) = \sum_{i=1}^{N_{pp}} \sum_{m=1}^{M} \left[a^i_m I_0(k_m r_4) - b^i_m K_0(k_m r_4) \right] \kappa(h, m, i) \tag{3.65}$$

- Radial component along $r = r_4$

$$B^{III}_{r\_in}\Big|_{r=r_4} = B^i_{r\_in}\Big|_{r=r_4} \forall z \in [z_i, z_i + \beta] \tag{3.66}$$

Or

$$a^i_m I_1(k_m r_4) + b^i_m K_1(k_m r_4) = \sum_{h=1}^{H} b^{III}_h K_1(k_h r_4) \eta(m, h, i) \text{ for } i = 1, \ldots, N_{pp} \tag{3.67}$$

Similarly, boundary conditions for the model shown in Fig. 3.3(b) can be obtained as follows.

- Axial component along $r = r_3$

$$B^{II}_{z\_out}\Big|_{r=r_3} = \begin{cases} B^i_{z\_out}\Big|_{r=r_3} \forall z \in [z_i, z_i + \beta] \\ 0 \text{ else} \end{cases} \tag{3.68}$$

Or

$$a^{II}_n I_0(k r_3) = \sum_{i=1}^{N_{pp}} \sum_{m=1}^{M} \left(a^i_m I_0(k_m r_3) - b^i_m K_0(k_m r_3) \right) \kappa(n, m, i) \tag{3.69}$$

- Radial component along $r = r_3$

$$B^{II}_{r\_out}\Big|_{r=r_3} = B^i_{r\_out}\Big|_{r=r_3} \forall z \in [z_i, z_i + \beta] \tag{3.70}$$

Or

$$a^i_m I_1(k_m r_3) + b^i_m K_1(k_m r_3) = \sum_{n=1}^{N} \left(a^{II}_n I_1(k_n r_3) \right) \eta(m, n, i) \text{ for } i = 1, \ldots, N_{pp} \tag{3.71}$$

- Axial component along $r = r_4$

$$B^{III}_{z\_out}\Big|_{r=r_4} = \begin{cases} B^i_{z\_out}\Big|_{r=r_4} \forall z \in [z_i, z_i + \beta] \\ 0 \text{ else} \end{cases} \tag{3.72}$$

Or

$$a^{III}_h I_0(k_h r_4) - b^{III}_h K_0(k_h r_4) = \sum_{i=1}^{N_{pp}} \sum_{m=1}^{M} \left(a^i_m I_0(k_m r_4) - b^i_m K_0(k_m r_4) \right) \kappa(h, m, i) \tag{3.73}$$

- Radial component along $r = r_4$

$$B^{III}_{r\_out}\Big|_{r=r_4} = B^{i}_{r\_out}\Big|_{r=r_4} \forall \mathrm{z} \in [z_i, z_i + \beta] \tag{3.74}$$

Or

$$\mathrm{a}^{i}_{m} I_1(k_m r_4) + b^{i}_{m} K_1(k_m r_4) = \sum_{h=1}^{H} \left(\mathrm{a}^{III}_{h} I_1(k_h r_4) + b^{III}_{h} K_1(k_h r_4)\right) \eta\,(m, h, i) \tag{3.75}$$

for $i = 1, \ldots, N_{pp}$

- Radial component along $r = r_5$

$$B^{III}_{r\_out} = B^{IV}_{r\_out}\Big|_{r=r_5} \tag{3.76}$$

Or

$$I_1(k_h r_5)\mathrm{a}^{III}_{h} + K_1(k_h r_5) b^{III}_{h} - I_1(k_h r_5)\mathrm{a}^{IV}_{h} - K_1(k_h r_5) b^{IV}_{h} = \tfrac{\pi P_h}{2k_h^2} L_1\,(k_h r_5) \tag{3.77}$$

- Axial component along $r = r_5$

$$B^{III}_{z\_out} = \left.\frac{B^{IV}_{z\_out}}{\mu_r}\right|_{r=r_5} \tag{3.78}$$

Or

$$\mu_r I_0(k_h r_5)\mathrm{a}^{III}_{h} - \mu_r K_0(k_h r_5) b^{III}_{h} - I_0(k_h r_5)\mathrm{a}^{IV}_{h} + K_0(k_h r_5) b^{IV}_{h} = \tfrac{\pi P_h}{2k_h^2} L_0\,(k_h r_5) \tag{3.79}$$

- Radial component along $r = r_6$

$$B^{V}_{r\_out} = B^{IV}_{r\_out}\Big|_{r=r_6} \tag{3.80}$$

Or

$$-I_1(k_h r_6)\mathrm{a}^{IV}_{h} - K_1(k_h r_6) b^{IV}_{h} + K_1(k_h r_6) b^{V}_{h} = \tfrac{\pi P_h}{2k_h^2} L_1\,(k_h r_6) \tag{3.81}$$

- Axial component along $r = r_6$

$$B^{V}_{z\_out} = \left.\frac{B^{IV}_{z\_out}}{\mu_r}\right|_{r=r_6} \tag{3.82}$$

Or

$$-I_0(k_h r_6)\mathrm{a}^{IV}_{h} + K_0(k_h r_6) b^{IV}_{h} - \mu_r K_0(k_h r_6) b^{V}_{h} = \tfrac{\pi P_h}{2k_h^2} L_0\,(k_h r_6) \tag{3.83}$$

where $r_1 - r_6$ are the radii of inner PMs, pole pieces, and outer PMs as shown in Fig. 3.1.

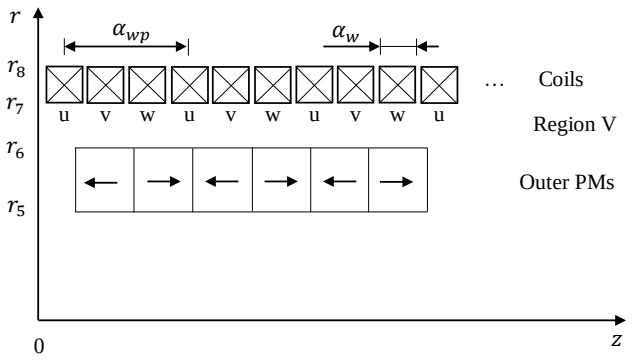

Figure 3.4: 2-D model of high-speed mover and winding coils.

3.2.6 Force Transmission of the TMG

In this section, we discuss the thrust force on the high-speed and low-speed movers of the MG part. The average magnetic thrust force on the low-speed mover (F_{in}) and high-speed mover (F_{out}) can be obtained by calculating the Maxwell stress tensor in cylindrical coordinates [20].

$$F_{in} = \frac{\pi R_{in}}{2\mu_0} \int_{z-L/2}^{z+L/2} B_r^{II}(R_{in})\, B_z^{II}(R_{in})\, dz \tag{3.84}$$

$$F_{out} = \frac{\pi R_{out}}{2\mu_0} \int_{z-L/2}^{z+L/2} B_r^{III}(R_{out})\, B_z^{III}(R_{out})\, dz \tag{3.85}$$

Subsequently, force transmission capacity can be analyzed by moving the low-speed mover while maintaining the high-speed mover stationary.

3.2.7 Thrust Force

To calculate the thrust force generated by the winding coil on the high-speed mover, we consider model shown in Fig. 3.4. The thrust force exerted on the high-speed mover, which is produced by a single coil when it carries a current density J, can be obtained from the following integration [69].

$$F_s = -\int_{z-\alpha_w/2}^{z+\alpha_w/2} \int_{r_7}^{r_8} 2\pi r J B_r^V \, dr dz \tag{3.86}$$

where

$$B_r^V = \sum_{m=1}^{\infty} -b_m^V K_1(k_m r)\cos(k_m z) \tag{3.87}$$

$$J = \sqrt{2} J_{rms} \sin(\omega t) \tag{3.88}$$

and let:

$$K_{sm} = \int_{r_7}^{r_8} b_m^V K_1(k_m r) r dr \tag{3.89}$$

Thus, the thrust force produced by only a single coil can be expressed as follows.

$$F_s = 4\sqrt{2}\pi J_{rms} \sum_{m=1}^{\infty} K_{sm} \cos(k_m z) \sin\left(\frac{k_m \alpha_w}{2}\right) \sin(\omega t) \tag{3.90}$$

Finally, the thrust force on the high-speed mover produced by a single phase (F_{sp}) and the total of the three phase (F_{total}) can be obtained as follows.

$$F_{sp} = \sum_{n=1}^{N_w} F_s\left(z + n\alpha_{wp}\right) \tag{3.91}$$

$$F_{total} = F_{spu} + F_{spv} + F_{spw} \tag{3.92}$$

where N_w is the number of winding coils in each single phase, F_{spu} is the thrust force produced by phase u, F_{spv} is the thrust force produced by phase v, and F_{spw} is the thrust force produced by phase w.

3.3 Results and Discussion

Fig. 3.5 shows the experimental model. It consists of some main parts as follows:

- A tubular MGLM as shown in Fig. 3.6;
- A three-phase inverter as shown in Fig. 3.7 and Table 3.1;
- A PE-Expert4 controller as shown in Fig. 3.8 and Table 3.2;
- Two position sensors (encoder) as shown in Fig. 3.9 and Table 3.3;
- Two force sensors as shown in Fig. 3.10 and Table 3.4.

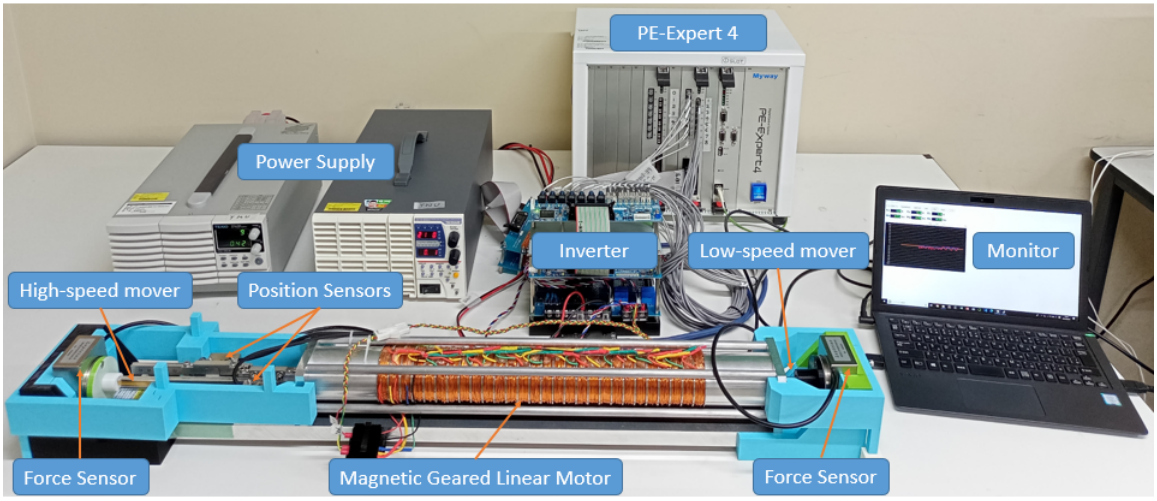

Figure 3.5: Experiment model.

Figure 3.6: Experiment TMGLM.

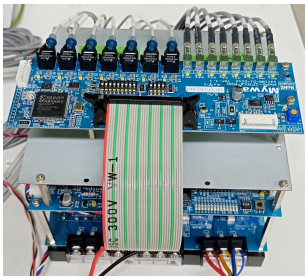

Figure 3.7: The inverter.

Table 3.1: Parameters of the inverter

Explanation	Value	Unit
Model	MWINV-1R022	-
Power supply	200	VAC
Output current	2.88	Arms
Switching frequency	~20	kHz
Dead time	3.0	μs

Figure 3.8: The PE-Expert4 controller.

Table 3.2: Parameters of the PE-Expert4 controller

DSP board (MWPE4-C6657)		**PEV board (MWPE4-PEV)**	
Item	**Specification**	**Item**	**Specification**
DSP	TMS320C6657	3-phase PWM	6 gates and 1 brake
On chip RAM	1024KB/32KB	Modulation	Voltage triangular wave, Voltage space vector
Ext. RAM	512MB	Carrier (Dead time)	1kHz ∼ 500kHz
EEPROM	128KB	PWM precision	14bit (10kHz carrier)
PC interface	Ethernet (optical)	ADC	14bit 8ch
Isolated RS232C	2 sets Dsub-9pin	Digital input/output	16ch ea.
CAN port speed	125kbps ∼ 1Mbps	Input capture	32bit 4ch
CAN port connector	1set Dsub-9pin	Up/Down counter	32bit 1set

Figure 3.9: Position sensor.

Table 3.3: Parameters of the position sensor

RGH24 Readhead			**RGH24 Scale**		
Explanation	Value	Unit	Explanation	Value	Unit
Power supply	5	V	Scale period	20	μs
Acceleration	500	m/s^2	Linearity	±3	μm/s
Maximum frequency	500	KHz	Scale length	< 50	m

Figure 3.10: Force sensor.

Table 3.4: Parameters of the force sensor

Explanation	**Value**	**Unit**
Model	PFS055YA501U6	-
Rate output		
F_x, F_y, F_z	±500	N
M_x, M_y	±10	Nm
M_z	±8	Nm
Nonlinearity	±1%	R.O
Resolution	±1/4000	R.O

3.3.1 Magnetic Flux

Fig. 3.11 shows the flux density distribution excited by the low-speed mover in the middle of the inner air gap. The results show a good agreement between the 3-D FEA results (Analyzed) and 2-D model calculation (Calculated) results for both radial and axial components. Furthermore, good agreement is obtained in the case of the flux density caused by the high-speed mover for both radial and axial components, as shown in Fig. 3.12. The axial component of the magnetic flux density is approximately 80% greater than the radial one.

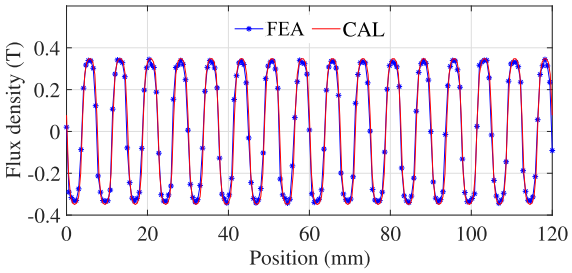

(a) Radial component

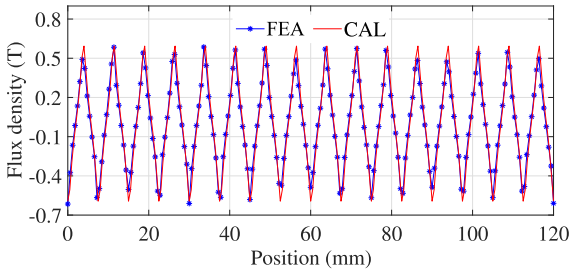

(b) Axial component

Figure 3.11: Flux density distributions in the middle of inner air-gap excited by low-speed mover.

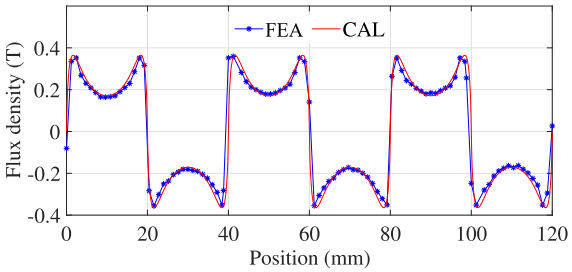

(a) Radial component

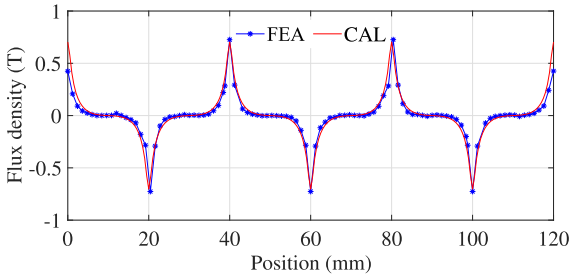

(b) Axial component

Figure 3.12: Flux density distributions in the middle of outer air-gap excited by high-speed mover.

Fig. 3.13 and Fig. 3.14 show the distributions of the magnetic flux density produced by the low-speed mover modulated by the pole pieces and the magnetic flux density excited by the high-speed mover modulated by the pole pieces, respectively. The results clearly show the modulation effect of the ferromagnetic pole pieces on the flux distribution. The magnetic flux densities are amplified into different waveform from the initial ones shown in Fig. 3.11 and Fig. 3.12.

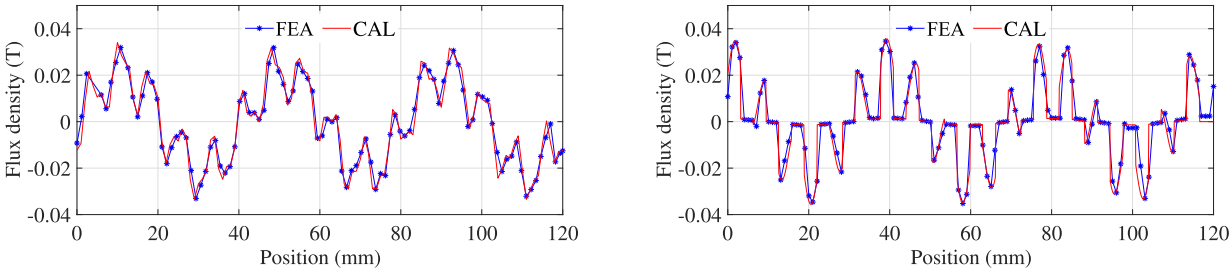

(a) Radial component (b) Axial component

Figure 3.13: Flux density distributions in the middle of outer air-gap excited by low-speed mover modulated by pole pieces.

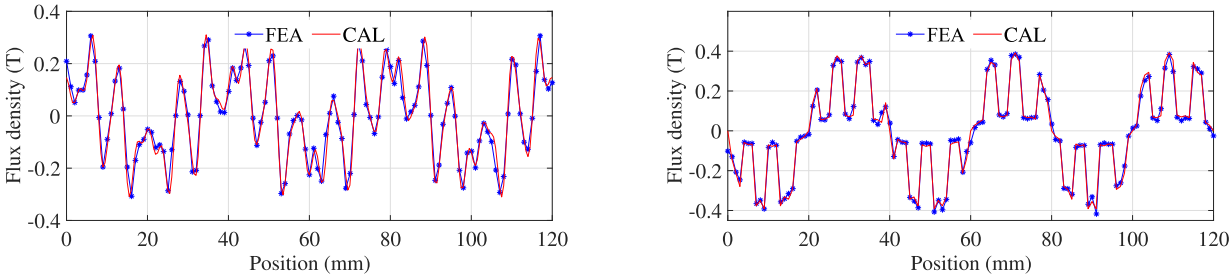

(a) Radial component (b) Axial component

Figure 3.14: Flux density distributions in the middle of inner air-gap excited by high-speed mover modulated by pole pieces.

The magnetic flux density distributions at the middle of the outer air gap region ($r = R_{out}$) and the middle of the inner air gap region ($r = R_{in}$) excited by both the high-speed and low-speed movers are shown in Fig. 3.15 and Fig. 3.16, respectively. Good agreement between the 2-D calculated and 3-D FEA analysis results is observed for both radial and axial components.

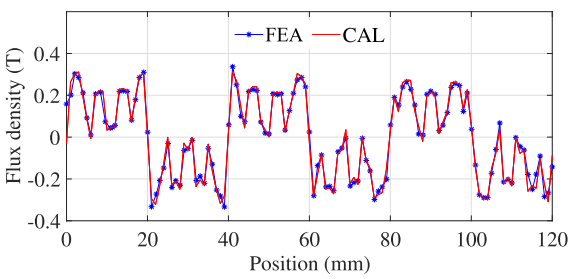

(a) Radial component

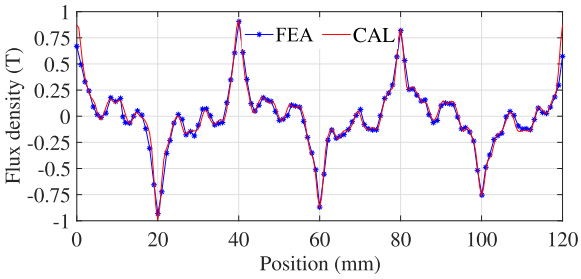

(b) Axial component

Figure 3.15: Flux density distributions in the middle of outer air-gap excited by high-speed and low-speed movers.

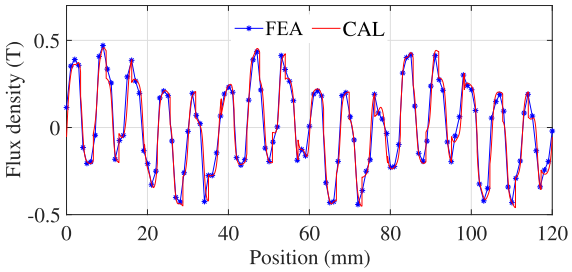

(a) Radial component

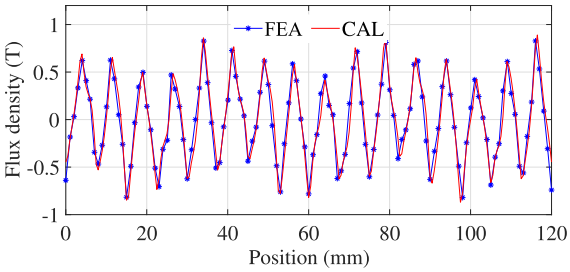

(b) Axial component

Figure 3.16: Flux density distributions in the middle of inner air-gap excited by both high-speed and low-speed mover.

The flux density distributions in the middle of air gaps, which were only excited by the coils carrying a three-phase current (amplitude 2 A, frequency 2 Hz) are shown in Fig. 3.17 and Fig. 3.18. Fig. 3.19a shows the flux distributions of the motor, and Fig. 3.19b shows the flux distribution of the coils when a three-phase current (amplitude 2 A, frequency 2 Hz) is applied. These results show that the flux density distributions excited by the coils are significantly weaker than those excited by the PMs.

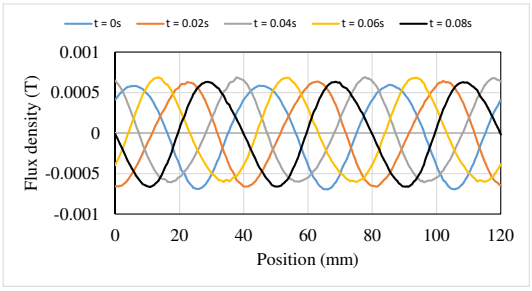

(a) Radial component

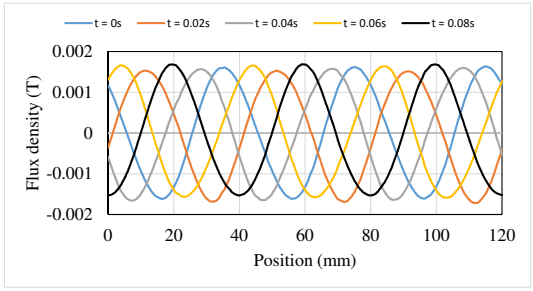

(b) Axial component

Figure 3.17: Flux density distribution in the middle of the inner air gap excited by the coils.

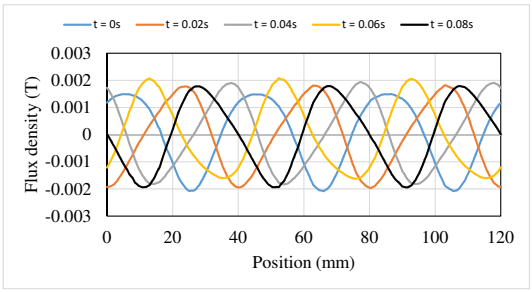

(a) Radial component

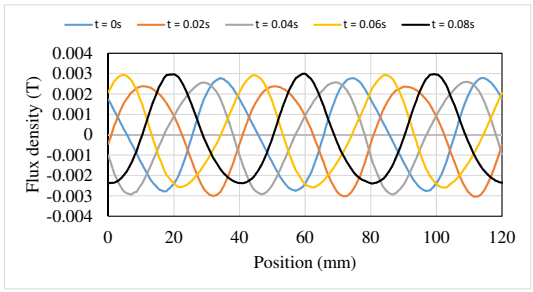

(b) Axial component

Figure 3.18: Flux density distribution in the middle of the outer air gap excited by the coils.

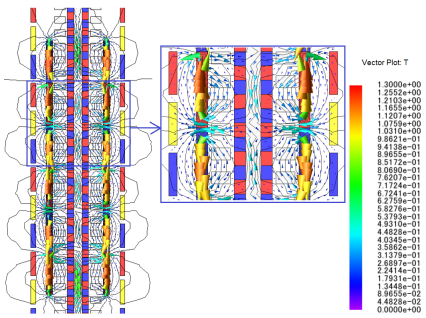

(a) Flux distribution of the MGLM

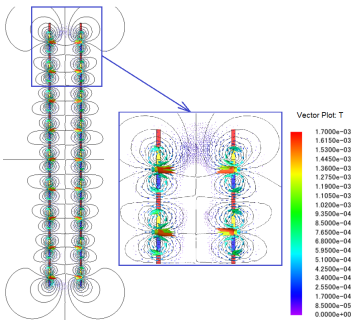

(b) Flux distribution of the coils

Figure 3.19: Flux distribution.

3.3.2 Thrust Force

Fig. 3.20a shows the force transmission capacity when the high-speed mover is fixed at z = 3.05 mm, low-speed mover travels with a velocity 0.375 mm/s from 0 mm, and the pole piece is stationary at 2.05 mm. The maximum forces on the high-speed and low-speed mover are approximately -19.29 N and -103.41 N, respectively. Furthermore, the calculation, FEA, and experimental results are in good agreement. From these results, gear ratio of the MG can be determined to be approximately 5.36.

For investigating thrust force generated by the winding coil on the high-speed mover, three-phase excited currents (frequency 1 Hz, amplitudes 1.5 A and 2 A) are applied to the coil while keeping the high-speed mover fixed. The results of the thrust force are presented in Fig. 3.20b and Table 3.5. The maximum thrust force exerted on the high-speed mover depends on the current carried in the coil; the values are 13.82 N and 18.39 N for currents of 1.5 A and 2 A, respectively. The calculation and FEA results are in close agreement. However, there are differences between the experimental and calculated results, which may be due to manufacturing factors as the coils are not exactly identical in terms of resistances, inductances, etc.

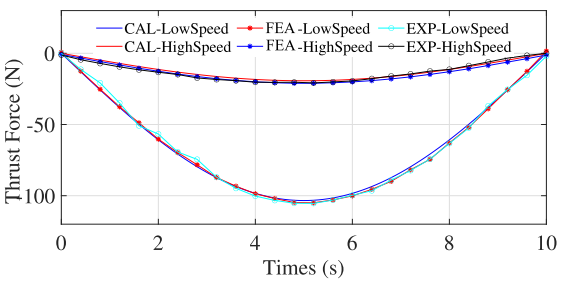

(a) Force transmission capacity

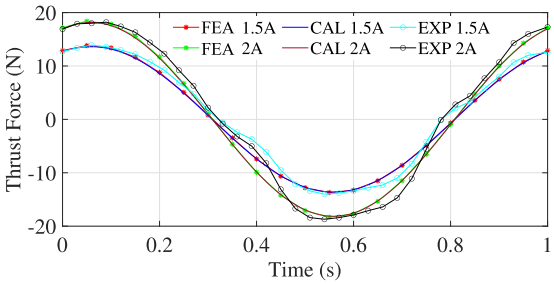

(b) Force produced by three phases

Figure 3.20: Force

Table 3.5: Summary of thrust force results

Current[A]	Phase	Maximum force[N]
1.5	U	3.27
1.5	V	5.67
1.5	W	9.22
1.5	U-V-W	13.82
2	U	4.34
2	V	7.53
2	W	12.27
2	U-V-W	18.39

To obtain thrust force versus current, a simple PI controller is designed to track reference current applied into the three phase coils. Thrust force generated by the mover is measured by a force sensor. Fig. 3.21 shows an example to achieve thrust force on the low-speed mover at I_q = 2.2 A.

Fig. 3.22 shows the thrust force on the low-speed and high-speed movers versus current I_q. There is agreement between calculation, experiment and FEA results of thrust force generated on the high-speed mover (F_h). However, calculated force on the low-speed mover (F_l) significantly greater than experimental and FEA results. The difference is due to ignore of resistant force in the calculated model. In addition, if the two movers travel at the same time, thrust forces which estimated by FEA only depend on the difference in initial positions between the two movers. Therefore, there is a different in FEA and calculation methods.

It also can be observed that, if the applied current is greater than 2.6 A, the generated force on the low-speed mover maintains approximate 100 N. It is because of the maximal force the gear can be transmitted. The two movers slide together when the force exerted on the high-speed mover generated by the coils beyond 19.29 N (at I_q approximate 2.6 A). This situation will make mistake if thrust force on the low-speed mover is calculated through gear ratio and thrust force on the high-speed mover ($F_l = G_r F_h$). This error can be solved if estimated thrust force on the mover by maximal force and the difference positions between the two movers in (4.17). On the other hand, low-speed mover force significantly decreases if input current less than 2.0 A. From this results, it can be concluded that the motor should operate with current varies from 2.0 to 2.6 A.

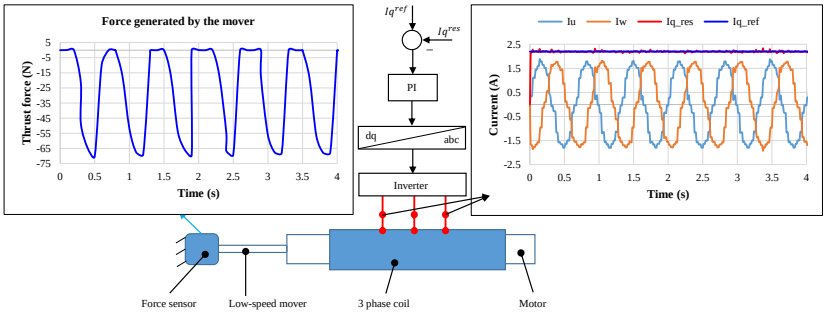

Figure 3.21: Example to obtain thrust force on the low-speed mover at I_q = 2.2 A.

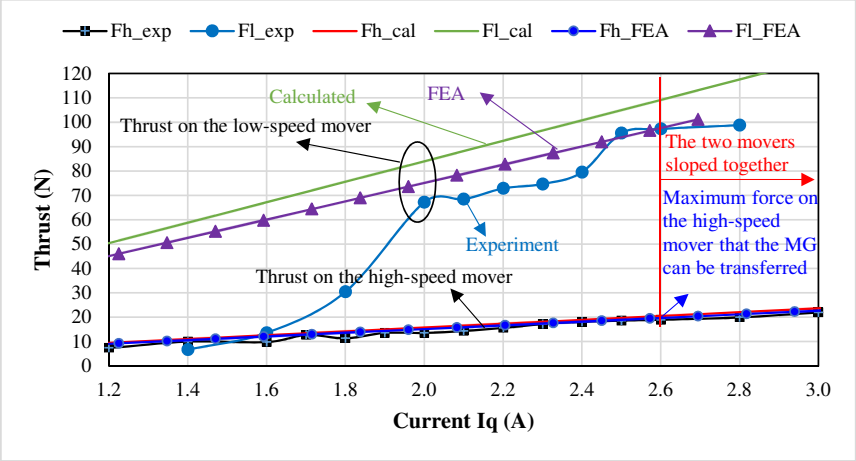

Figure 3.22: Thrust characteristic.

In comparison on thrust force density, some topologies can provide both linear and rotary motions, meanwhile the other motors only provide linear motion. Some structures can achieve high/very high thrust force which maybe require wider air-gap length than structure of lower thrust force output. Therefore, high/very high thrust force motors have smaller thrust force density. In addition, some topologies have been developed for high/super high speed applications and some other for lower range of velocity. Thus, it is difficult to obtain conclusion on superiority because various design conditions differ. If only consider thrust force density, the presented motor achieves 31.1% higher than TL-HPM and 20.1% less than BSA1. Table 3.6 shows the summary on thrust force per active volume of some highlight topologies.

Table 3.6: Comparison of thrust force capabilities

Topologies	**Rate thrust force (N)**	**Thrust force per active volume (MN/m^3)**	**Reference**
TL-SPM	-	0.225	[70]
TL-IPM	-	0.258	[70]
TL-HPM	254	0.324	[71]
The motor in this study	-	0.469	
BSA1	804	0.588	http://www.thk.com/
DCP-TFLM	853	0.615	[72]
Helical motion motor	200	0.64	[73]
FSTFPMLM	570	0.712	[74]

TL-SPM: tubular linear surface-mounted permanent magnet motor

TL-IPM: tubular linear interior permanent magnet motor

TL-HPM: tubular linear quasi-Halbach magnetized permanent magnetic motor

BSA1: ballscrew actuator with lead length 10 mm

DCP-TFLM: dual-consequent-pole transverse flux machine

FSTFPMLM: flux switching transverse flux permanent magnet linear machine

3.3.3 Losses

Motor loss is dominated by copper loss, iron loss, and mechanical losses. Copper loss can be more or less known from the current flowing in the coils. However, iron loss depends on material properties, drive conditions, and geometry. Following, iron in magnetic material (pole-pieces and shaft) and Eddy current loss in permanent magnets are discussed.

Iron loss in magnetic material can be classified into Hysteresis and Joule losses (eddy current loss). Apply loop and FFT methods are used to account for Hysteresis and Joule losses, respectively.

- Apply loop method for Hysteresis loss conducted by formula as follows [75]

$$W_h = \sum_{e=1}^{nelem} \left\{ f \sum_{l=1}^{nloop} \left(Kh \times B_k^{\alpha} \times V_e \right) \right\} \tag{3.93}$$

  where:

  - W_h : Hysteresis loss
  - B_k^{α} : Amplitude of magnetic flux density of $k-th$ loop for each component
  - Kh : Coefficient of hysteresis loss
  - V_e : Volume of each element
  - f : Basic frequency
  - $nelem$: Number of element
  - α : Coefficient of the empiric formula
  - $nloop$: Number of loop

- FFT method for Joule loss conducted by formula as follows [75]

$$W_e = \sum_{e=1}^{nelem} \left\{ f \sum_{k=1}^{N} \left(Ke \times |B_k|^{\gamma} \times f_k^{\delta} \times V_e \right) \right\} \tag{3.94}$$

  where:

  - W_e : Joule loss
  - $|B_k|^{\gamma}$: Magnetic flux density at frequency order of k
  - Ke : Coefficient of Joule loss
  - V_e : Volume of each element
  - f_k : Frequency at frequency order: f_1, f_2,..., f_N
  - $nelem$: Number of element
  - γ, δ : Coefficient of the empiric formula
  - N : Maximum frequency order

Using FFT method to estimate Joule loss, basic frequency needs to determine. In tubular magnetic gear topology, the basic frequency can be obtained, as follows:

$$f_{pole-pieces} = \frac{v_h}{2\tau_h} N_{hpm} \tag{3.95}$$

where $f_{pole-pieces}$ denotes basic frequency; N_{hpm} is the number of high-speed mover pole pairs; v_h and τ_h are velocity and pole-pitch of high-speed mover, respectively.

Fig. 3.23a and Fig. 3.23b illustrate ratio between Joule and Hysteresis losses versus velocity of the high-speed mover. The both Joule and Hysteresis losses dramatically increase with mover's speed; Joule loss are significantly greater than Hysteresis loss. Fig. 3.23c shows the contribution of iron loss on the pole-pieces and shaft. This result indicates that almost iron loss is on the pole-pieces because of its greater volume. Hysteresis loss density distribution and Joule loss density distribution when v_h equals to 1.33 m/s are shown in Fig. 3.24a and Fig. 3.24b, respectively. The iron loss on the magnetic gear is summarized in Table 3.7.

* The iron losses analysis based on 50JN1000 steel due to lack of S45C steel loss database.

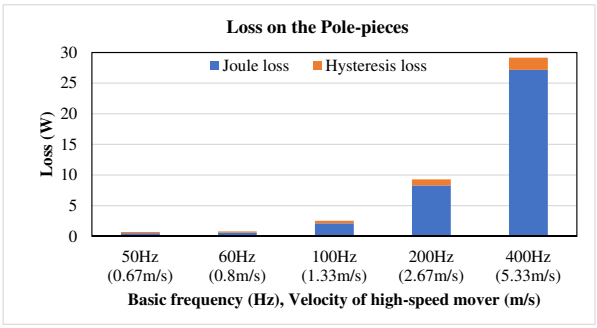

(a) Ratio of loss on the pole-pieces

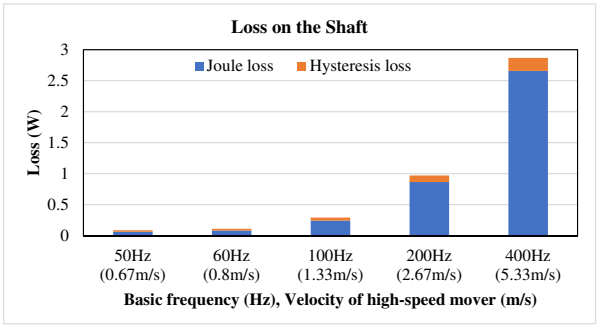

(b) Ratio of loss on the shaft

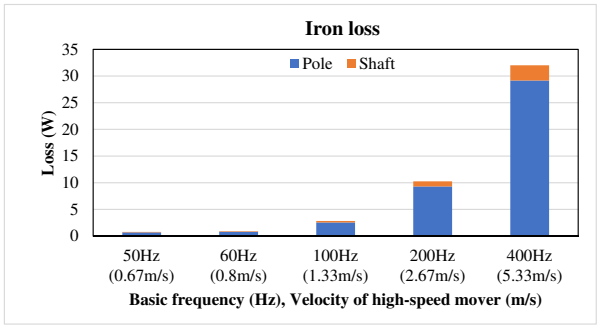

(c) Ratio of iron loss between pole-pieces and shaft

Figure 3.23: Iron loss in the magnetic gear (FEA).

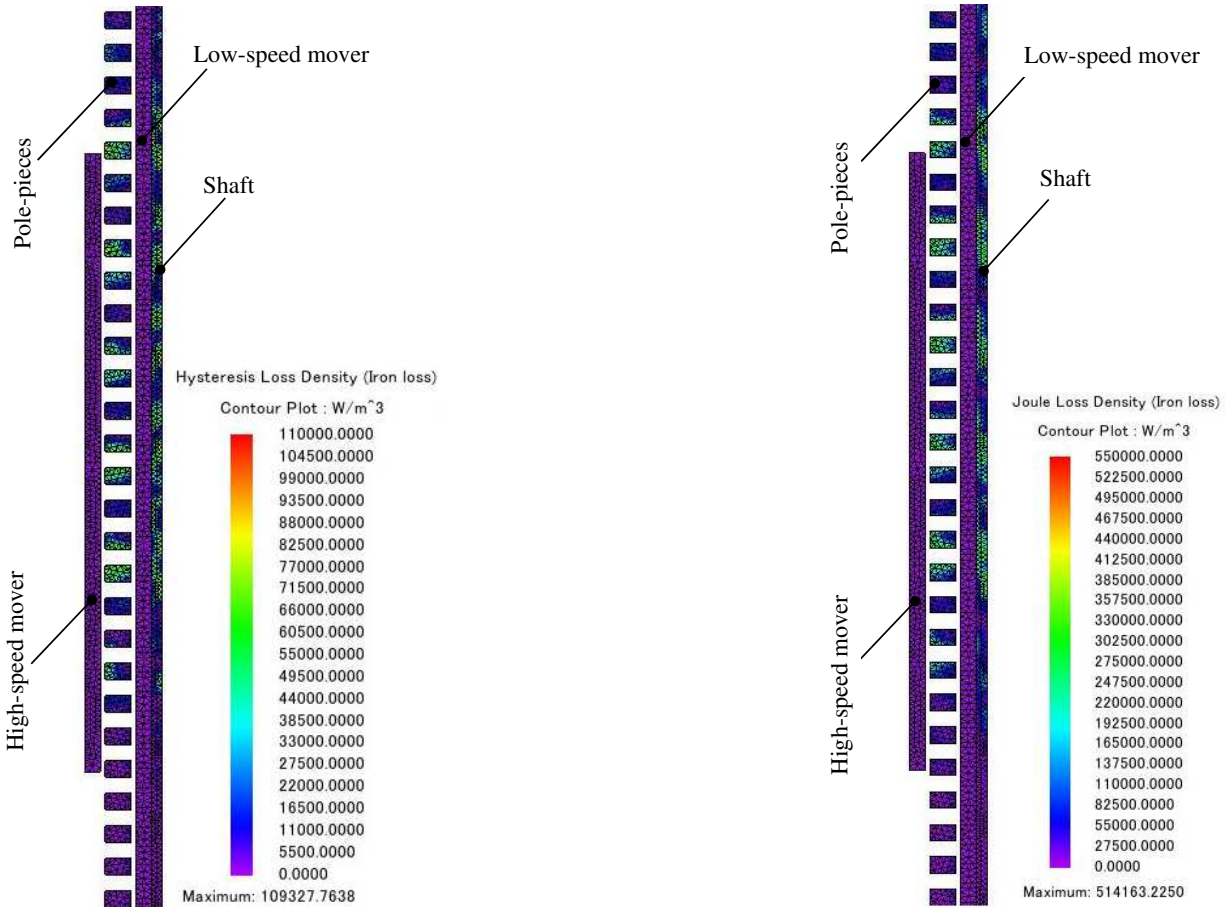

(a) Hysteresis loss density distribution

(b) Joule loss density distribution

Figure 3.24: Iron loss density distribution of the magnetic gear (FEA).

Table 3.7: Summary of iron loss in the magnetic gear

Basic frequency (Hz)	Velocity of high-speed mover (m/s)	Pole-pieces		Shaft	
		Hysteresis loss (W)	Joule loss (W)	Hysteresis loss (W)	Joule loss (W)
50	0.67	0.1900	0.5023	0.0228	0.0638
60	0.8	0.1868	0.6200	0.0260	0.0833
100	1.33	0.4195	2.1195	0.0494	0.2423
200	2.67	0.9875	8.3087	0.1061	0.8645
400	5.33	1.9840	27.1745	0.2102	2.6579
1000	13.33	5.3980	128.1301	0.5327	11.6476

Eddy current density and eddy current loss density distribution in the magnet, when high-speed mover travels with velocity of 1.33 m/s, are shown in Fig. 3.25a, 3.25b and Fig. 3.25c respectively. Fig. 3.26 shows the eddy current loss on the magnets of the two-movers versus speed. These results show that eddy current loss on the magnets significantly increase following the increasing of mover's velocity. In addition, losses on the magnets dramatically less than iron loss on the pole-pieces. From losses analysis results, we can ignore iron losses, magnet loss if velocity of the high-speed mover is small (total iron and magnet losses approximates 0.8164 W at v_h = 0.67 m/s).

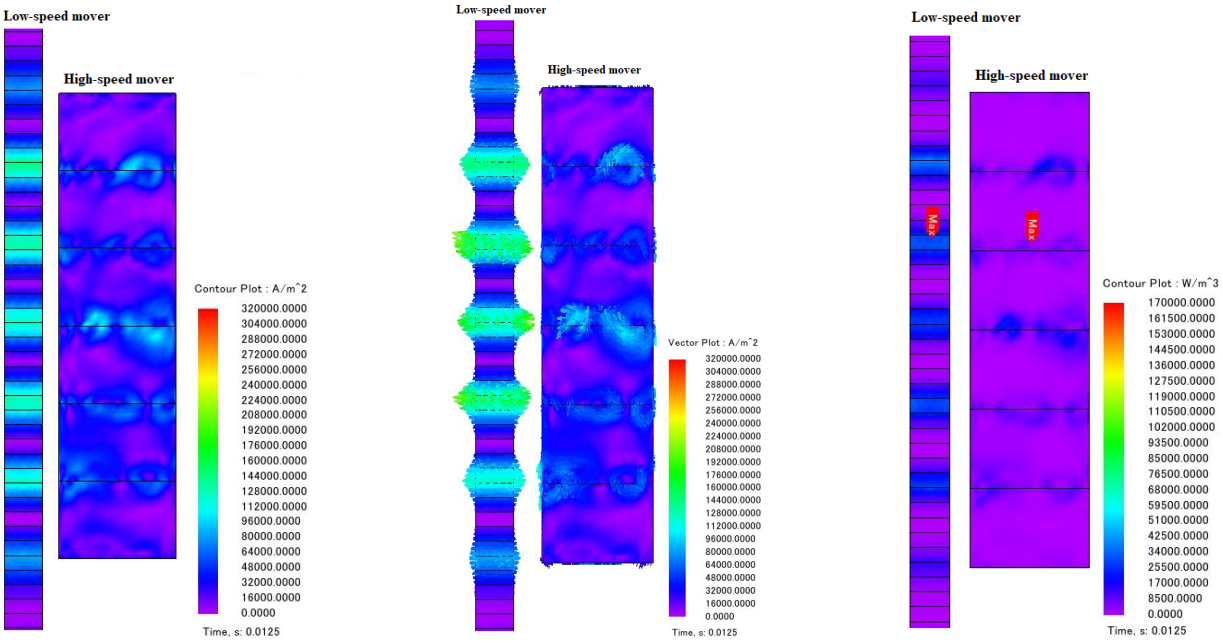

(a) Eddy current density distribution in the magnets

(b) Eddy current vector distribution in the magnets

(c) Eddy current loss density distribution in the magnet

Figure 3.25: Eddy current loss in the magnets of movers (FEA).

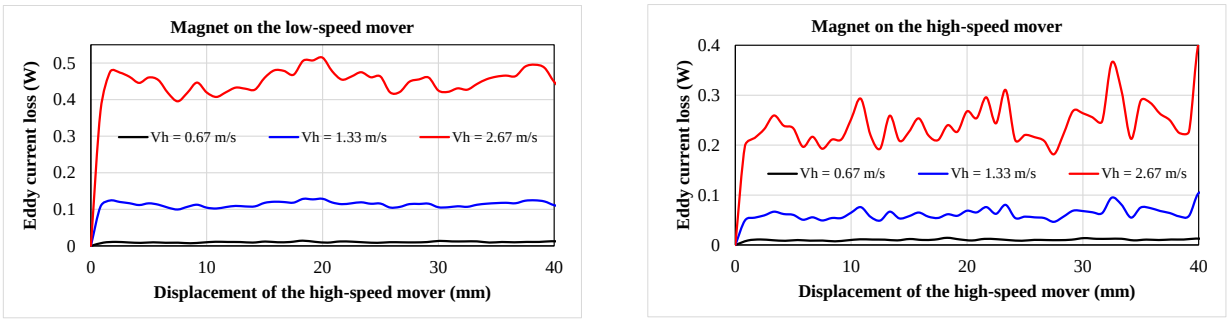

(a) Eddy current loss in the magnets of low-speed mover

(b) Eddy current loss in the magnets of high-speed mover

Figure 3.26: Eddy current loss in the magnets (FEA).

3.3.4 Effect of Geometrical Parameters on the Thrust Force

This section introduces an application of the calculated flux density as a simple tool for optimization design. For instance, investigating the influence of pole-pieces and magnet thicknesses on the output thrust force to determine their optimization parameters.

Fig. 3.27a shows the effect of the radial thickness of the pole-pieces on the thrust force value when the other geometrical parameters do not change. From this result, the maximal thrust force is obtained for a pole-pieces thickness of 6 mm.

To study effect of the PMs thickness on the thrust force when the other parametric do not change, the total magnet thicknesses of the low-speed and high-speed movers is fixed ($d_h + d_l = constant$).

Assuming,

$$K_{pm} = \frac{d_h}{d_h + d_l} \tag{3.96}$$

where d_h and d_l are the radial magnet thicknesses of the high-speed and low-speed movers respectively; K_{pm} denotes the ratio between magnet thicknesses of the two movers.

Fig. 3.27b illustrates effect of the PMs thicknesses on the thrust force values when the thickness ratio varies from 0.3 to 0.8. The result indicates that the thickness of the high-speed mover (3.6 mm) should be greater the thickness of the low-speed mover (2.4 mm) at thickness ratio $K_{pm} = 0.6$.

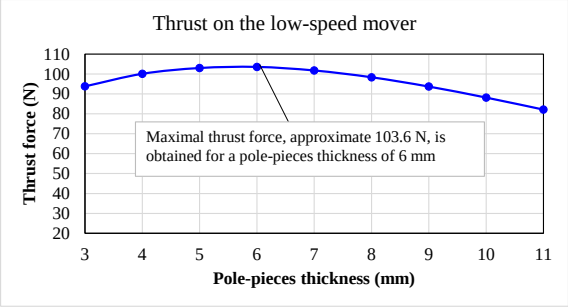

(a) Effects of the radial thickness of the pole-piece on the thrust force (calculation)

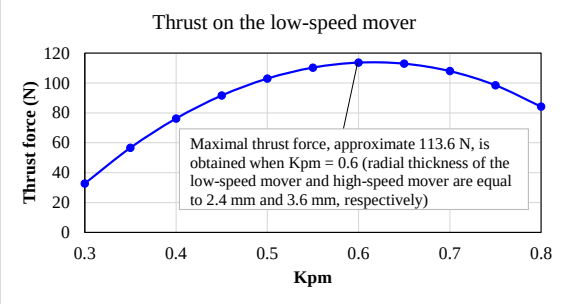

(b) Effects of the radial thickness of the PMs on the thrust force (calculation)

Figure 3.27: Effects of geometrical parameters on the thrust force.

3.4 Summary

In this chapter, a solution for calculating flux density distribution in a high thrust tubular magnetic gear is presented. Using separation variable method to solve Laplace's and Poisson's equations, general solution for magnetic fluxes in the gear are calculated. Particularly solutions of magnetic flux are predicted by find out integral coefficients based on boundary conditions. The advantages and disadvantages of the method are listed as follows:

Advantage

- In general, the method requires much less computational time than FEA (comparison of consuming time is shown in Table 3.8).
- The method in this study provides both radial and axial components of flux densities instead of only one component in previous method which applied for tubular magnetic gear as shown in Table 3.9.
- The method can be used as a simple tool for designing optimization such as investigate effect of thickness of magnet, pole-pieces, pole pitch on output thrust to choose the optimum geometrical parameters

Disadvantage

- Assuming permeability of the iron is infinite and characteristic of the material is linear;
- Saturation is ignored;
- 3-D effect, end effect are ignored, etc.

Table 3.8: Comparison of computation time

Method	**Hardware**	**Platform**	**Computing time/ Analysis time**
Method in this study	Intel(R) Core(TM) i9-10900K CPU @ 3.70GHz RAM 32.0GB Windows 10 Home x64	MATLAB R2023a	01 min 37.69 sec
FEA 3D model (Mesh size 1mm)	Intel(R) Xeon(R) CPU E5-2680 0 @ 2.70GHz RAM 64.0GB Windows 10 Pro x64	JMAG Designer 20.1	06 hour 57 min 28 sec
FEA 2D model (Mesh size 1mm)			30 min 05 sec

Table 3.9: Comparison of solutions for magnetic flux density distribution in magnetic gears

Method	Structure	Advantage	Disadvantage
Presented method	Tubular	Provide both axial and radial component of magnetic flux density	Neglected loss, saturation effect,⋯
Circuit-field-motion solution [16]	Tubular	Suitable for both nodal method and loop method, used to couple fields and circuits	Only provide radial component of magnetic flux density. So, the method cannot provide thrust on the mover. Neglected loss, saturation effect,⋯
Lumped parameter magnetic circuits technique [17]	Tubular	Consider both linear and nonlinear isotropic steel for the pole-pieces, and infinitely permeable high-speed armature and stator yokes	Only provide radial component of magnetic flux density
Magnetic circuit modeling [66]	Tubular	Provide fundamental mathematical model of tubular magnetic gear	Only provide radial component of magnetic flux density
Resolution of Laplace's and Poisson's equations [18]	Co-axial	Provide both axial and radial components of magnetic flux density	Neglected loss, saturation effect,⋯

Chapter 4

Modeling and Controller Design

4.1 Abstract

Accurately predict mathematical model is essential for designing and developing controller for new generation motor. Various topologies and solutions for computation of flux distribution in magnetic gear have been published. However, the previous methods do not focus on control purpose. This chapter presented a mathematical model of the motor which aims to control position of the motor's mover. The main idea of the mathematical model is that consider reaction forces between the two movers in their motion equations. Further more, a position controller which is applied for the motor is developed. Simulation and experiment are employed to confirm the accuracy of the motor model. The accurately experimental trajectory response results validate the controller performance.

4.2 Modeling of the Tubular Linear Motor Part

This section presents about modeling of the TLM part which included of winding coils and high-speed mover. Basing on Faraday's law, equivalent equation that describes the electric part of a permanent magnetic tubular linear synchronous motor (PM-TLSM) are given as follows.

$$\begin{cases} u_a = R_a i_a + \frac{d\psi_a}{dt} \\ u_b = R_b i_b + \frac{d\psi_b}{dt} \\ u_c = R_c i_c + \frac{d\psi_c}{dt} \end{cases} \tag{4.1}$$

where u_a, u_b, u_c; i_a, i_b, i_c; R_a, R_b, R_c, and ψ_a, ψ_b, ψ_c are the voltages, currents, winding resistances and linkage fluxes on phase a, b, c, respectively.

These linkage fluxes can be obtained as follows.

$$\begin{cases} \psi_a = L_a i_a + M_{ab} i_b + M_{ac} i_c + \psi_{ma} \\ \psi_b = L_b i_b + M_{ba} i_a + M_{bc} i_c + \psi_{mb} \\ \psi_c = L_c i_c + M_{ca} i_a + M_{cb} i_b + \psi_{mc} \end{cases} \tag{4.2}$$

where M_{ij} ($i = a, b, c$ and $j = a, b, c$) are the mutual inductances coefficients between i and j windings; L_a, L_b, and L_c are the self-inductances on phase a, b, c, respectively. The linkage fluxes ψ_{ma}, ψ_{mb}, and ψ_{mc} are established by permanent magnets on three phases windings, whose maximal value is represented by ψ_m as follows.

$$\begin{cases} \psi_{ma} = \psi_m cos(\frac{\pi}{\tau_h} z_h) \\ \psi_{mb} = \psi_m cos(\frac{\pi}{\tau_h} z_h - \frac{2\pi}{3}) \\ \psi_{mc} = \psi_m cos(\frac{\pi}{\tau_h} z_h + \frac{2\pi}{3}) \end{cases} \tag{4.3}$$

where τ_h is the pole pitch of the high-speed mover, z_h is the displacement of the high-speed mover.

Considering that the PM-TLSM stator have the same resistance value for all phase windings, as well as the same value for the self-inductances and mutual inductances coefficients.

$$\begin{cases} R_a = R_b = R_c = R_s \\ L_a = L_b = L_c = L_s \\ M_{ab} = M_{ba} = M_{ac} = M_{ca} = M_{bc} = M_{cb} = M_s \end{cases} \tag{4.4}$$

Hence, the linkage fluxes ψ_a, ψ_b, and ψ_c derivatives become:

$$\begin{cases} \frac{d\psi_a}{dt} = L_s \frac{di_a}{dt} + M_s \frac{di_b}{dt} + M_s \frac{di_c}{dt} - \frac{\pi}{\tau_h} \frac{dz_h}{dt} \psi_m sin(\frac{\pi}{\tau_h} z_h) \\ \frac{d\psi_b}{dt} = L_s \frac{di_b}{dt} + M_s \frac{di_a}{dt} + M_s \frac{di_c}{dt} - \frac{\pi}{\tau_h} \frac{dz_h}{dt} \psi_m sin(\frac{\pi}{\tau_h} z_h - \frac{2\pi}{3}) \\ \frac{d\psi_c}{dt} = L_s \frac{di_c}{dt} + M_s \frac{di_a}{dt} + M_s \frac{di_b}{dt} - \frac{\pi}{\tau_h} \frac{dz_h}{dt} \psi_m sin(\frac{\pi}{\tau_h} z_h + \frac{2\pi}{3}) \end{cases} \tag{4.5}$$

In order to simplify the linear motor part model, (4.1) - (4.5) can be written in matrix form as follows.

$$u_{abc} = R_s i_{abc} + L_{abc} \frac{di_{abc}}{dt} + \frac{dz_h}{dt} \frac{d\psi_{abc}}{dz_h} \tag{4.6}$$

where

$$u_{abc} = \begin{bmatrix} u_a \\ u_b \\ u_c \end{bmatrix} \qquad R_s = \begin{bmatrix} R_s & 0 & 0 \\ 0 & R_s & 0 \\ 0 & 0 & R_s \end{bmatrix} \qquad i_{abc} = \begin{bmatrix} i_a \\ i_b \\ i_c \end{bmatrix} \tag{4.7}$$

$$L_s = \begin{bmatrix} L_s & M_s & M_s \\ M_s & L_s & M_s \\ M_s & M_s & L_s \end{bmatrix} \qquad \psi_{abc} = \begin{bmatrix} -\frac{\pi}{\tau_h} \frac{dz_h}{dt} \psi_m sin(\frac{\pi}{\tau_h} z_h) \\ -\frac{\pi}{\tau_h} \frac{dz_h}{dt} \psi_m sin(\frac{\pi}{\tau_h} z_h - \frac{2\pi}{3}) \\ -\frac{\pi}{\tau_h} \frac{dz_h}{dt} \psi_m sin(\frac{\pi}{\tau_h} z_h + \frac{2\pi}{3}) \end{bmatrix} \tag{4.8}$$

Next, using Park's transform, (4.6) can be rewritten in $d-q$ coordinate as follows.

$$\begin{cases} \frac{di_d}{dt} = -\frac{R_s}{L_d} i_d + \frac{dz_h}{dt} \frac{\pi}{\tau_h} \frac{L_q}{L_d} i_q + \frac{1}{L_d} u_d \\ \frac{di_q}{dt} = -\frac{dz_h}{dt} \frac{\pi}{\tau_h} \frac{L_d}{L_q} i_d - \frac{R_s}{L_q} i_q + \frac{1}{L_q} u_q - \frac{dz_h}{dt} \frac{\pi}{\tau_h} \frac{\psi_p}{L_q} \\ \theta_{rl} = \frac{\pi}{\tau_h} z_h \end{cases} \tag{4.9}$$

where θ_{rl} is angular position given by rotary-linear geometric motor transformation; ψ_p represents permanent magnet flux linkage; u_d, u_q; i_d, i_q, and L_d, L_q denote the d-axis and q-axis voltages, currents, and winding inductances, respectively.

For mechanic equation, there is a different in comparing with conventional PM-TLSM. There is always reaction force between high-speed and low-speed movers in case of the TMGLM. Thus, the motion equation in case of TMGLM can be given by the second Newton's law as follows.

$$F_e - F_{rh} - F_{hm} = m_h \frac{d^2 z_h}{dt^2} \tag{4.10}$$

where F_e represents for electromagnetic force which generated by winding coils, F_{rh} is the resistant force, m_h is the mass of the high-speed mover, and F_{hm} is the force transmitted to the high-speed mover from low-speed mover which will be calculated in Section 4.3.

The resistant force F_{rh} in (4.10) can be expressed as follows.

$$F_{rh} = K_{dh} \frac{dz_h}{dt} + K_{eh} \tag{4.11}$$

where K_{dh} represents for dynamic attrition coefficient and K_{eh} is the static attrition coefficient on the high-speed mover.

The electromagnetic force F_e in (4.10), is described by using the principle of field oriented control as follows [76].

$$F_e = \frac{3}{2} \frac{\pi}{\tau_h} \psi_p i_q \tag{4.12}$$

Finally, the model of TLM part is described by (4.9) and (4.12) in field synchronous coordinate. Fig. 4.1 shows model block diagram of the TLM part.

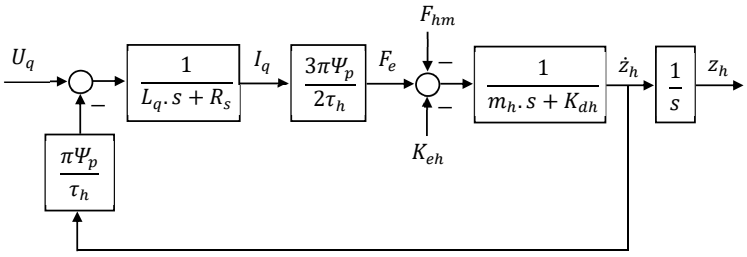

Figure 4.1: Model of the linear motor part.

4.3 Modeling of the Tubular Magnetic Gear Part

This section describes about modeling of the TMG part which combined of high-speed mover, pole-pieces, and low-speed mover. In this work, the pole-pieces is stationary, low-speed and high-speed mover travel in opposite direction, thus gear ratio G_r can be expressed as follows.

$$G_r = -\frac{N_{lpm}}{N_{hpm}} \tag{4.13}$$

If losses are neglected, the force transmission relationship between low-speed and high-speed movers is given by.

$$F_{lm}\dot{z}_l = F_{hm}\dot{z}_h \tag{4.14}$$

where z_l and F_{lm} are the displacement of low-speed mover and thrust force which transmitted to low-speed from high-speed movers, respectively.

Other hand, force transmitted to low-speed mover from high-speed mover, F_{lm}, can be given

$$F_{lm}(\theta) = F_{maxl}sin(\theta) \tag{4.15}$$

where F_{maxl} is the maximal transmission force from high-speed to low-speed movers which was solved in [77]; θ is the angular displacement between the two movers and it can be obtained by

$$\theta = \frac{2\pi(z_h - z_{h0})}{\tau_h} + \frac{2\pi(z_l - z_{l0})}{\tau_l} \tag{4.16}$$

where z_{h0} and z_{l0} denote initial position of low-speed and high-speed movers, respectively.

Similarly, force transmitted to high-speed mover from low-speed mover can be given

$$F_{hm}(\theta) = -F_{maxh}sin(\theta) \tag{4.17}$$

where F_{maxh} is the maximal transmission force to high-speed from low-speed movers.

In other word, applying equation of motion for low-speed and high-speed movers, we have

$$\begin{cases} m_l\ddot{z}_l = F_{lm}(\theta) - F_{load} - F_{rl} \\ m_h\ddot{z}_h = F_e - F_{rh} - F_{hm}(\theta) \end{cases} \tag{4.18}$$

where F_{load} is load exerted on low-speed mover. The resistant force on the low-speed mover F_{rl} can be expressed as follows.

$$F_{rl} = K_{dl}\frac{dz_l}{dt} + K_{el} \tag{4.19}$$

where K_{dl} represents for dynamic attrition coefficient and K_{el} is the static attrition coefficient on the low-speed mover.

Finally, model of the TMG part can be obtained as follows.

$$\begin{cases} \ddot{z}_l = \{F_{lm}(\theta) - F_{load} - F_{rl}\}/m_l \\ \ddot{z}_h = \{F_e - F_{rh} - F_{hm}(\theta)\}/m_h \\ F_{lm}(\theta) = F_{maxl}sin(\theta) \\ F_{hm}(\theta) = -F_{maxh}sin(\theta) \\ \theta = 2\pi(z_h - z_{h0})/\tau_h + 2\pi(z_l - z_{l0})/\tau_l \\ F_{rl} = K_{dl}\frac{dz_l}{dt} + K_{el} \\ F_{rh} = K_{dh}\frac{dz_h}{dt} + K_{eh} \end{cases} \tag{4.20}$$

Fig. 4.2 shows model block diagram of the TMG part.

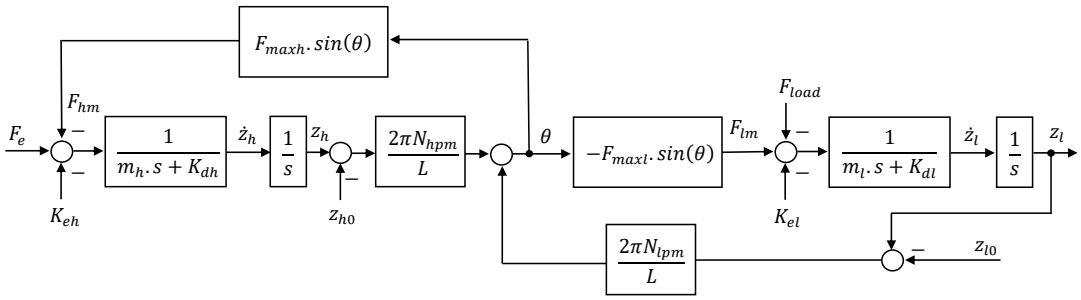

Figure 4.2: Model of the magnetic gear part.

4.4 Modeling of the Tubular Magnetic Geared Linear Motor

Firstly, we consider electrical part of the TMGLM. From (4.14) we have

$$\dot{z}_h = \frac{F_{lm}}{F_{hm}}\dot{z}_l \tag{4.21}$$

Other hand, from (4.15) and (4.17) we have

$$\frac{F_{lm}(\theta)}{F_{hm}(\theta)} = -\frac{F_{maxl}}{F_{maxh}} \tag{4.22}$$

Thus,

$$\dot{z}_h = -\frac{F_{maxl}}{F_{maxh}}\dot{z}_l \tag{4.23}$$

Substituting (4.23) into the first and second equations of (4.9), we have

$$\begin{cases} \frac{di_d}{dt} = -\frac{R_s}{L_d}i_d - \frac{F_{maxl}}{F_{maxh}}\frac{\pi}{\tau_h}\frac{L_q}{L_d}\frac{dz_l}{dt}i_q + \frac{1}{L_d}u_d \\ \frac{di_q}{dt} = \frac{F_{maxl}}{F_{maxh}}\frac{\pi}{\tau_h}\frac{L_d}{L_q}\frac{dz_l}{dt}i_d - \frac{R_s}{L_q}i_q + \frac{1}{L_q}u_q + \frac{F_{maxl}}{F_{maxh}}\frac{\pi}{\tau_h}\frac{\psi_p}{L_q}\frac{dz_l}{dt} \end{cases} \tag{4.24}$$

(4.24) can be written in state space model as follows.

$$\frac{di}{dt} = Ai + Bu + Niv_l + S\psi_p v_l \tag{4.25}$$

where

$$i = \left[i_d, i_q\right]^T ; u = \left[u_d, u_q\right]^T \tag{4.26}$$

System matrix:

$$A = \begin{bmatrix} -\frac{R_s}{L_d} & 0 \\ 0 & -\frac{R_s}{L_q} \end{bmatrix} \tag{4.27}$$

Input matrix:

$$B = \begin{bmatrix} \frac{1}{L_d} & 0 \\ 0 & -\frac{1}{L_q} \end{bmatrix} \tag{4.28}$$

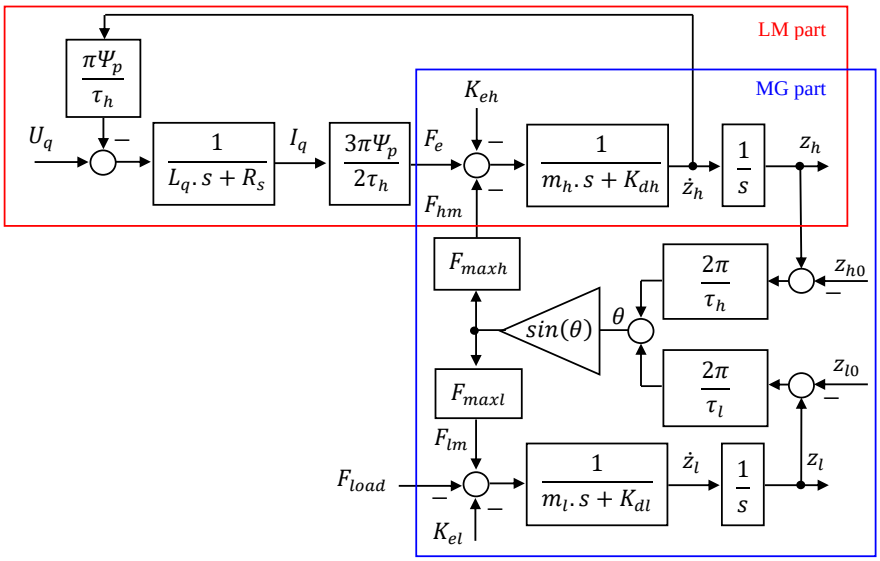

Figure 4.3: Model of the TMGLM.

Nonlinear coupling matrix:

$$N = \begin{bmatrix} 0 & -\frac{F_{maxl}}{F_{maxh}}\frac{\pi}{\tau_h}\frac{L_q}{L_d} \\ \frac{F_{maxl}}{F_{maxh}}\frac{\pi}{\tau_h}\frac{L_d}{L_q} & 0 \end{bmatrix} \tag{4.29}$$

Disturbance vector:

$$S = \begin{bmatrix} 0 \\ \frac{F_{maxl}}{F_{maxh}}\frac{\pi}{\tau_h}\frac{1}{L_q} \end{bmatrix} \tag{4.30}$$

In case of TMGLM, the state space description in (4.25) is characterized by a bilinear characteristic due to there is a multiple between the element v_l and vector i.

Secondly, combining (4.25), electromagnetic force F_e in (4.12), and equation of motion for low-speed and high-speed movers in (4.18), complete continuous model of the TMGLM can now be achieved as follows.

$$\begin{cases} \frac{di}{dt} = Ai + Bu + Niv_l + S\psi_p v_l \\ F_e = 3\pi\psi_p i_q / 2\tau_h \\ \ddot{z}_l = \{F_{lm}(\theta) - F_{load} - F_{rl}\} / m_l \\ \ddot{z}_h = \{F_e - F_{rh} - F_{hm}(\theta)\} / m_h \end{cases} \tag{4.31}$$

Through a control strategy, based on $i_d = 0$, the block structure of the model for TMGLM is shown in Fig. 4.3.

4.5 Controller Design

This section proposes a controller to demonstrate controllable ability of low-speed mover's position.

Changing coordinate system. Assuming that $v_l = dz_l/dt$; $x = \left[i_d, i_q, z_l\right]^T$; $u = \left[u_d, u_q, v_l\right]^T$; $y = \left[i_d, i_q, z_l\right]^T = I_{(3x3)}x$.

Now (4.24) becomes

$$\begin{cases} \frac{dx_1}{dt} = -\frac{R_s}{L_d}x_1 - \frac{F_{maxl}}{F_{maxh}}\frac{\pi}{\tau_h}\frac{L_q}{L_d}x_2u_3 + \frac{1}{L_d}u_1 \\ \frac{dx_2}{dt} = \frac{F_{maxl}}{F_{maxh}}\frac{\pi}{\tau_h}\frac{L_d}{L_q}x_1u_3 - \frac{R_s}{L_q}x_2 + \frac{1}{L_q}u_2 + \frac{F_{maxl}}{F_{maxh}}\frac{\pi}{\tau_h}\frac{\psi_p}{L_q}u_3 \\ \frac{dx_3}{dt} = u_3 \end{cases} \tag{4.32}$$

Or (4.32) can be expressed as

$$\begin{cases} \dot{x} = f(x) + h_1u_1 + h_2u_2 + h_3u_3 \\ y = g(x) \end{cases} \tag{4.33}$$

where:

$$f(x) = \begin{bmatrix} -\frac{R_s}{L_d}x_1 \\ -\frac{R_s}{L_q}x_2 \\ 0 \end{bmatrix}; h_1 = \begin{bmatrix} \frac{1}{L_d} \\ 0 \\ 0 \end{bmatrix} \tag{4.34}$$

$$h_2 = \begin{bmatrix} 0 \\ \frac{1}{L_q} \\ 0 \end{bmatrix}; h_3 = \begin{bmatrix} -\frac{F_{maxl}}{F_{maxh}}\frac{\pi}{\tau_h}\frac{L_q}{L_d}x_2 \\ \frac{F_{maxl}}{F_{maxh}}\frac{\pi}{\tau_h}\frac{L_d}{L_q}x_1 + \frac{F_{maxl}}{F_{maxh}}\frac{\pi}{\tau_h}\frac{\psi_p}{L_q} \\ 1 \end{bmatrix} \tag{4.35}$$

$$\begin{cases} y_1 = g_1(x) = x_1 \\ y_2 = g_2(x) = x_2 \\ y_3 = g_3(x) = x_3 \end{cases} \tag{4.36}$$

Using exact linearization method, system described in (4.33) can be linearization to a linear system as

$$\begin{cases} \dot{z} = Az + Bw \\ y = Cz \end{cases} \tag{4.37}$$

(4.37) has feedback controller

$$u(x) = a(x) + L^{-1}(x)w \tag{4.38}$$

where vector $a(x)$ and matrix $L(x)$ can be look as follows

$$a(x) = -L^{-1}(x)\begin{bmatrix} L_fg_1(x) \\ L_fg_2(x) \\ L_fg_3(x) \end{bmatrix} \tag{4.39}$$

$$L(x) = \begin{bmatrix} L_{h1}g_1(x) & L_{h1}g_2(x) & L_{h1}g_3(x) \\ L_{h2}g_1(x) & L_{h2}g_2(x) & L_{h2}g_3(x) \\ L_{h3}g_1(x) & L_{h3}g_2(x) & L_{h3}g_3(x) \end{bmatrix} \tag{4.40}$$

where $L_f g(x) = \frac{\partial g(x)}{\partial x} f$, $L(x)$ can be achieved

$$L(x) = \begin{bmatrix} \frac{1}{L_d} & 0 & -\frac{F_{maxl}}{F_{maxh}} \frac{\pi}{\tau_h} \frac{L_q}{L_d} x_2 \\ 0 & \frac{1}{L_q} & \frac{F_{maxl}}{F_{maxh}} \frac{\pi}{\tau_h} \frac{L_d}{L_q} x_1 + \frac{F_{maxl}}{F_{maxh}} \frac{\pi}{\tau_h} \frac{\psi_p}{L_q} \\ 0 & 0 & 1 \end{bmatrix} \tag{4.41}$$

From (4.41) we have $det(L) = \frac{1}{L_d L_q} \neq 0$, it leads to

$$L^{-1}(x) = \begin{bmatrix} L_d & 0 & \frac{F_{maxl}}{F_{maxh}} \frac{\pi}{\tau_h} L_q x_2 \\ 0 & L_q & -\frac{F_{maxl}}{F_{maxh}} \frac{\pi}{\tau_h} L_d x_1 - \frac{F_{maxl}}{F_{maxh}} \frac{\pi}{\tau_h} \psi_p \\ 0 & 0 & 1 \end{bmatrix} \tag{4.42}$$

Determine $a(x)$ in (4.38)

$$\begin{aligned} a(x) &= -L^{-1}(x) \begin{bmatrix} L_f g_1(x), & L_f g_2(x), & L_f g_3(x) \end{bmatrix}^T \\ &= -L^{-1}(x) \begin{bmatrix} -\frac{R_s}{L_d} x_1, & -\frac{R_s}{L_q} x_2, & 0 \end{bmatrix}^T \\ &= \begin{bmatrix} R_s x_1 \\ R_s x_2 \\ 0 \end{bmatrix} \end{aligned} \tag{4.43}$$

Finally, obtained controller (4.38) in matrix form

$$\begin{bmatrix} u_1 \\ u_2 \\ u_3 \end{bmatrix} = \begin{bmatrix} R_s x_1 \\ R_s x_2 \\ 0 \end{bmatrix} + \begin{bmatrix} L_d & 0 & \frac{F_{maxl}}{F_{maxh}} \frac{\pi}{\tau_h} L_q x_2 \\ 0 & L_q & -\frac{F_{maxl}}{F_{maxh}} \frac{\pi}{\tau_h} L_d x_1 - \frac{F_{maxl}}{F_{maxh}} \frac{\pi}{\tau_h} \psi_p \\ 0 & 0 & 1 \end{bmatrix} \begin{bmatrix} w_1 \\ w_2 \\ w_3 \end{bmatrix} \tag{4.44}$$

Now (4.37) becomes

$$\begin{cases} \frac{dz}{dt} = \begin{bmatrix} 0 & 0 & 0 \\ 0 & 0 & 0 \\ 0 & 0 & 0 \end{bmatrix} z + \begin{bmatrix} 1 & 0 & 0 \\ 0 & 1 & 0 \\ 0 & 0 & 1 \end{bmatrix} w \\ y = \begin{bmatrix} 1 & 0 & 0 \\ 0 & 1 & 0 \\ 0 & 0 & 1 \end{bmatrix} z \end{cases} \tag{4.45}$$

where:

$$z = \begin{bmatrix} z_1 \\ z_2 \\ z_3 \end{bmatrix} = \begin{bmatrix} x_1 \\ x_2 \\ x_3 \end{bmatrix}; w = \begin{bmatrix} -\frac{R_s}{L_d} x_1 \\ -\frac{R_s}{L_q} x_2 \\ 0 \end{bmatrix} + L(x) \begin{bmatrix} u_1 \\ u_2 \\ u_3 \end{bmatrix} \tag{4.46}$$

The following transfer function for the TMGLM in new coordinated system is obtained

$$Y(s) = \begin{bmatrix} 1/s & 0 & 0 \\ 0 & 1/s & 0 \\ 0 & 0 & 1/s \end{bmatrix} W(s) \tag{4.47}$$

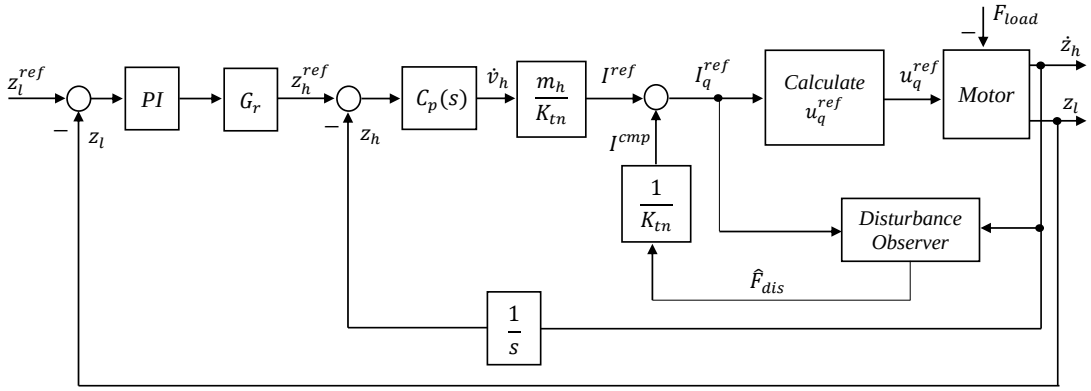

(a) Block diagram of the developed controller.

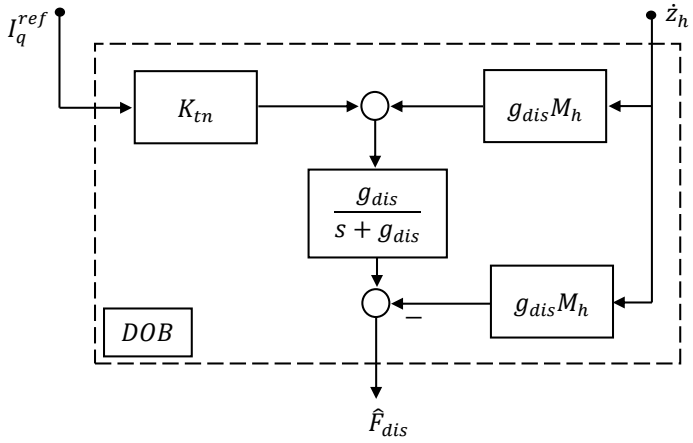

(b) Block diagram of disturbance observer controller.

Figure 4.4: Controller block diagram.

From (4.47), it can be seen that the output of a proportional transfer function with delay of 1^{st} order is not differentiable at t = 0 and the system has ability to decouple into independence channels.

In order to achieve accurate response value, displacements of both the low-speed and high-speed movers are required to feedback. The position of low-speed mover loop is designed by a PI controller. Meanwhile, a Disturbance observer (DOB) controller is chosen as position of high-speed mover loop. Fig. 4.4a and Fig. 4.4b show the principle block structure of the developed controller. Where K_{tn}, g_{dis}, and $C_p(s)$ denote force coefficient, cut-off frequency, and position controller on high-speed mover side, respectively. The $C_p(s)$ controller which aims to track the high-speed mover displacement can be expressed as follows:

$$C_p(s) = K_{ph} + K_{vh}.s \tag{4.48}$$

where K_{ph} and K_{vh} denote proportional and velocity gain of DOB controller, respectively.

Finally, the reference values of the controller can be obtained as follows.

$$z_h^{ref} = G_r(K_{pl} + \frac{K_{il}}{s})\Delta z_l \tag{4.49}$$

$$\dot{v}_h^{ref} = (K_{ph} + K_{dh}.s)\Delta z_h \tag{4.50}$$

$$i_q^{ref} = \frac{m_h}{K_{tn}} \dot{v}_h^{ref} + \frac{\hat{F}_{dis}}{K_{tn}} \tag{4.51}$$

$$\hat{F}_{dis} = (K_{tn} i_q^{ref} + g_{dis} M_h v_h) \frac{g_{dis}}{s + g_{dis}} - g_{dis} M_h v_h \tag{4.52}$$

$$u_q^{ref} = (R_s + L_q/s) i_q^{ref} + \pi \psi_p v_h / \tau_h \tag{4.53}$$

4.6 Results and Discussion

In this section, the presented motor model and controller are validated base on experimental and simulation results. Fig. 4.5a shows the experimental platform, it consists of six main components: a TMGLM, three-phase inverter, PE-Expert4 controller, force sensor, monitor, and two position sensors. Meanwhile, setup for load case is shown in Fig. 4.5b. Simulation is employed by MATLAB/Simulink in order to compare with experimental results. In addition, using finite element analysis (FEA), we can determine mutual inductance between winding coils, $M_s = 0$ mH, maximal transmission forces F_{maxl} and F_{maxh} equal to 103.41 N and 19.29 N, respectively. On the other hand, dynamic and static attrition coefficients of the movers determined: $K_{eh} = 0.5$, $K_{dh} = 6.5$, $K_{el} = 0.5$, $K_{dl} = 6.5$, $Z_{h0} = 0$ mm, $Z_{l0} = 1$ mm.

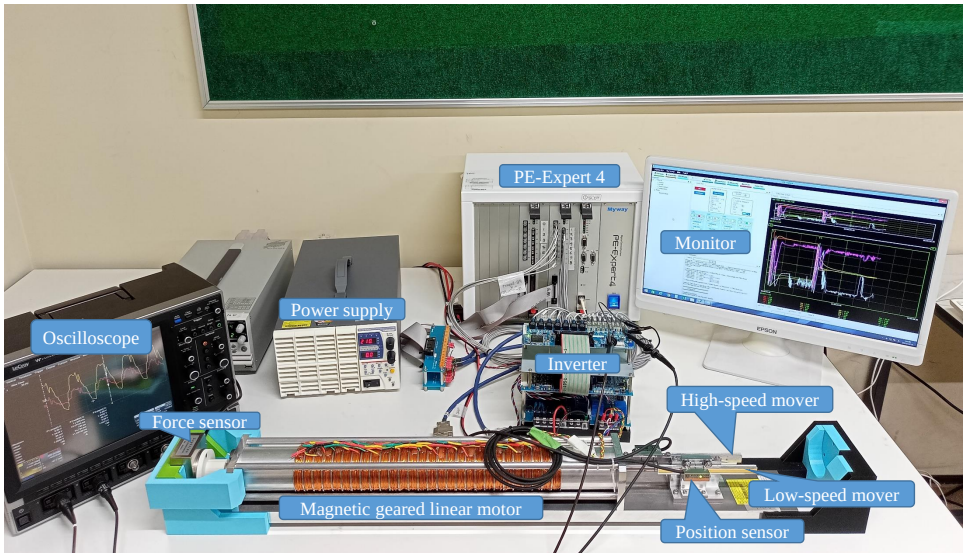

(a) Experimental model.

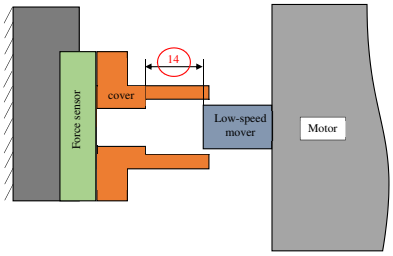

(b) Experimental setup of load.

Figure 4.5: Experimental platform

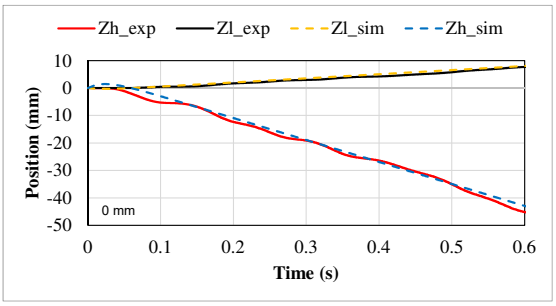

(a) z_{h0} = 0 mm.

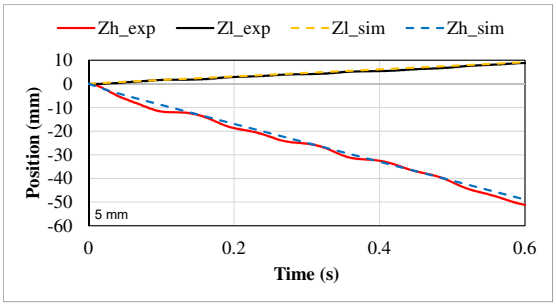

(b) z_{h0} = 5 mm.

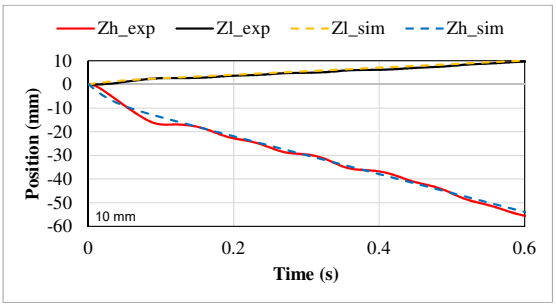

(c) z_{h0} = 10 mm.

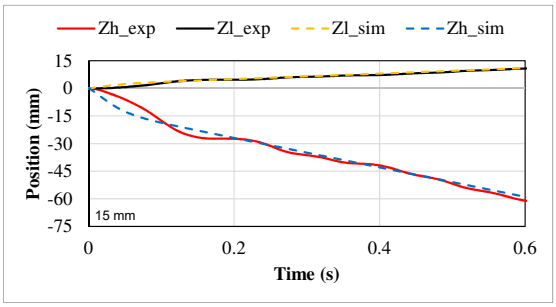

(d) z_{h0} = 15 mm.

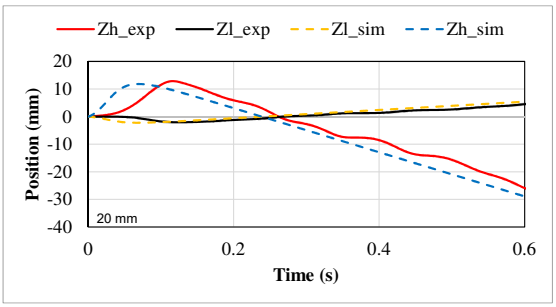

(e) z_{h0} = 20 mm.

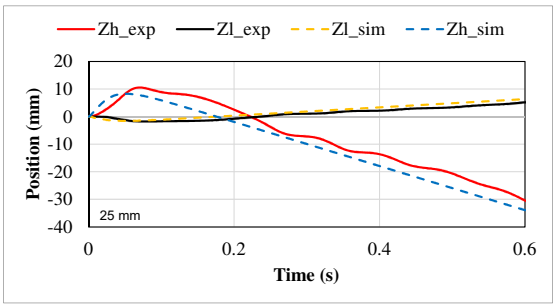

(f) z_{h0} = 25 mm.

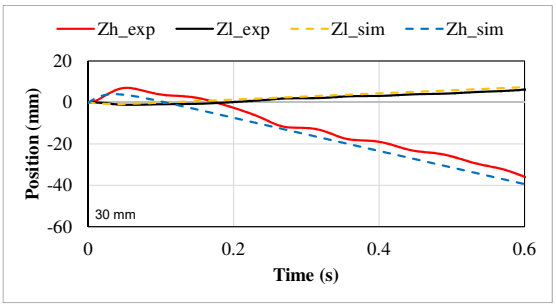

(g) z_{h0} = 30 mm.

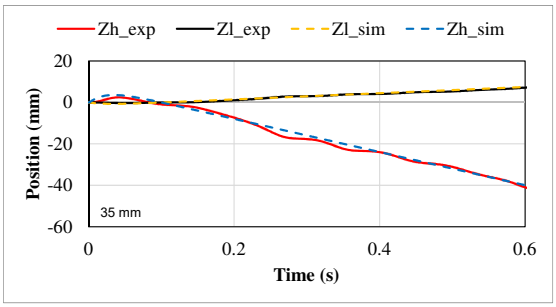

(h) z_{h0} = 35 mm.

Figure 4.6: Position of the two-movers.

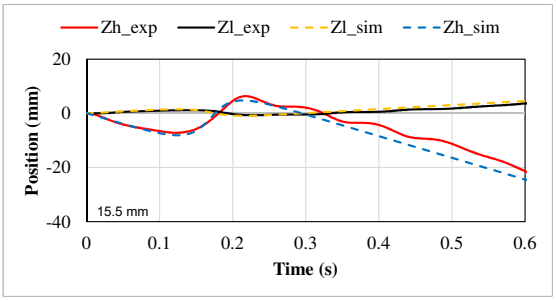

(a) z_{h0} = 15.5 mm.

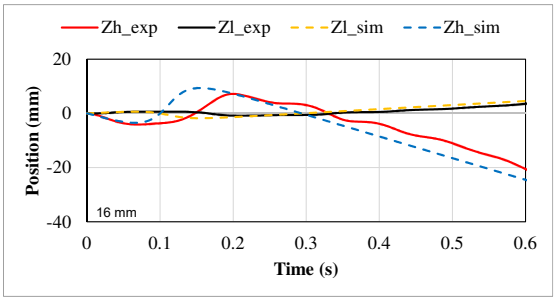

(b) z_{h0} = 16 mm.

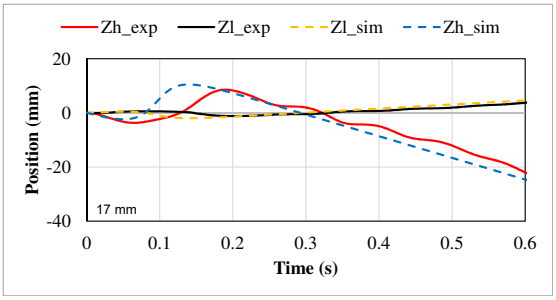

(c) z_{h0} = 17 mm.

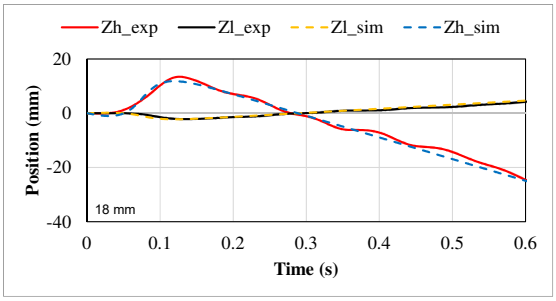

(d) z_{h0} = 18 mm.

Figure 4.7: Position of the two-movers at special displacements.

4.6.1 Motor Model Validation

To validate motor model, started-state characteristics of the motor in numerous difference initial positions of the high-speed mover are conducted. The simulation and experimental results are compared when a three-phase source (V_{rms} = 30 V, f = 2 Hz) is applied to the coils and motor works without load.

Fig. 4.6 shows the comparison between simulation and experimental results when initial position of the high-speed mover, z_{h0}, variables from 0 to 35 mm. There is a agreement between simulation and experimental results in both position of the low-speed and high-speed movers. From these results, it can be confirmed that started-state characteristic slightly changes in different initial positions. Fig. 4.6a shows the response position of the low-speed and high-speed movers when motor starts from 0 mm. There is a push force which made the movers move forward faster at z_{h0} belongs to [5, 15] mm (Fig. 4.6b to Fig. 4.6d). It is also found that the push forward force increases when z_{ho} leaves far from 0 mm. In contrast, existing a draw backward force which make the movers travel backward before moving toward when z_{ho} belongs to [20, 35] mm (Fig. 4.6e to Fig. 4.6h). The same phenomenon occurs when initial position of high-speed mover belongs to [-5, -35] mm

As can be seen from Fig. 4.6d and Fig. 4.7a to Fig. 4.7d, the started-state characteristic changes significantly when z_{ho} increases small distance from 15 mm. At z_{ho} = 15.5 mm, the high-speed mover moves forward and then backward before keeping forwarded instead of just moving forward. This phenomenon slightly changes when z_{ho} increases to 18 mm. The same circumstance happens when initial position of high-speed mover located in [-20, -25] mm.

4.6.2 Controller Validation

Table 4.1: Parameters of the controller

Controller	Symbol	Meaning	Value
DOB	K_{ph}	Proportional gain	350.0
	K_{vh}	Velocity gain	50.0
	K_{tn}	Force coefficient	12.5 N/A
	g_{dis}	Cut-off frequency	150.0 Hz
PI	K_{pl}	Proportional gain	1.6
	K_{il}	Integral gain	24.0

In order to evaluate the tracking performance of the developed controller, experimental was implemented in this section. The controller required to track a pulse and sinusoidal reference trajectory. The sampling time of the controller is 1 ms and term parameters is shown in Table 4.1.

Case 1: Motor works without load. Fig. 4.8a and Fig. 4.8b show response positions and tracking error when a reference displacement of low-speed mover is set by a pulse source (amplitude = 15 mm, period = 10 s, pulse width = 50 %). From these results, it can be seen that measured position tracked well the desired values. Additionally, transmission force from high-speed to low-speed movers (F_{lm}), reverse (F_{hm}), and estimated disturbance force on low-speed mover (F_{dis}) are shown in Fig. 4.8d. Meanwhile, Fig. 4.8e to Fig. 4.8h show response values under a sinusoidal source (amplitude = 15 mm, frequency = 0.05 Hz, initial phase = 0 deg). Again, well position tracking is obtained. However, there was a slight difference between transmission force which was calculated from displacement of the two movers (eq.(4.15)) and estimated force from Disturbance observer controller.

Case 2: The low-speed mover directly contacts to the force sensor when its displacement beyond 14 mm from start point (load configure is shown in Fig. 4.5b). Fig. 4.9 illustrates response positions, tracking errors, and estimated forces under the same references as in case 1. The experimental results show corresponded from response values to reference trajectory. The estimated forces have the same form, however, there was still slight differences between these forces.

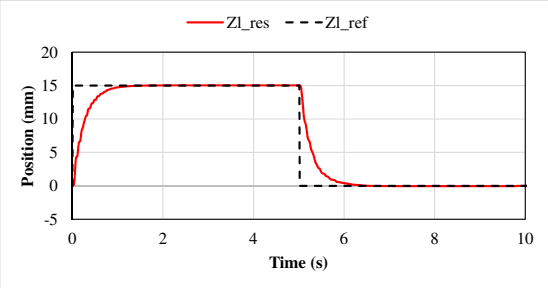

(a) Position of low-speed mover under pulse command.

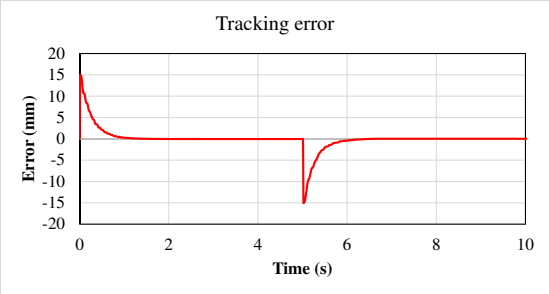

(b) Tracking error under pulse command.

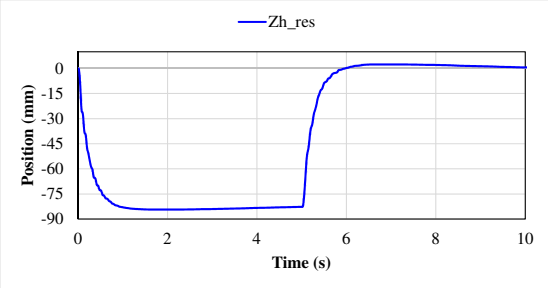

(c) Position of high-speed mover under pulse command.

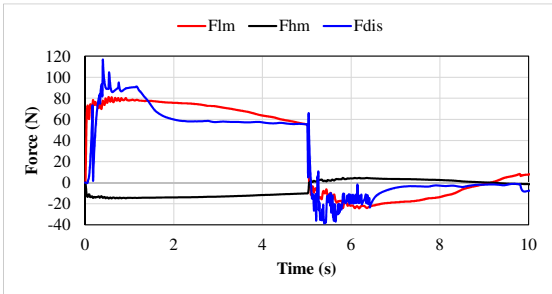

(d) Estimated force under pulse command.

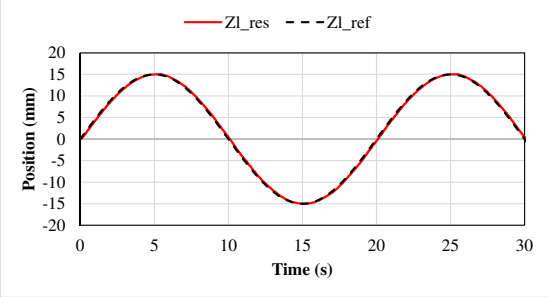

(e) Position of low-speed mover under sine command.

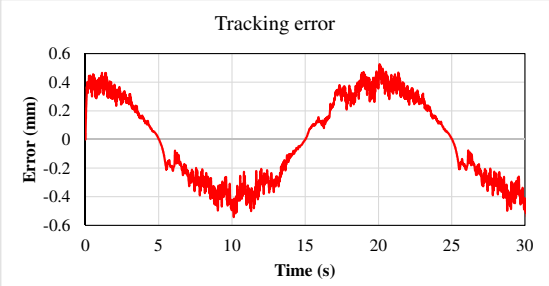

(f) Tracking error under sine command.

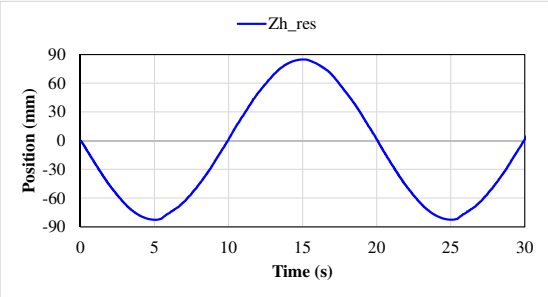

(g) Position of high-speed mover under pulse command.

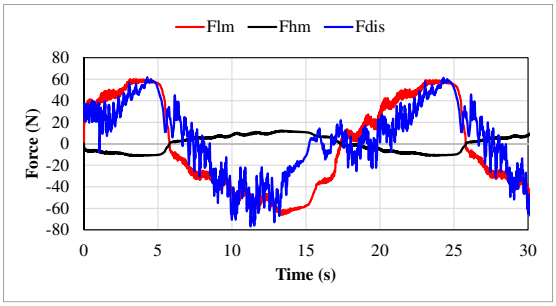

(h) Estimated force under sine command.

Figure 4.8: Experimental results under no-load.

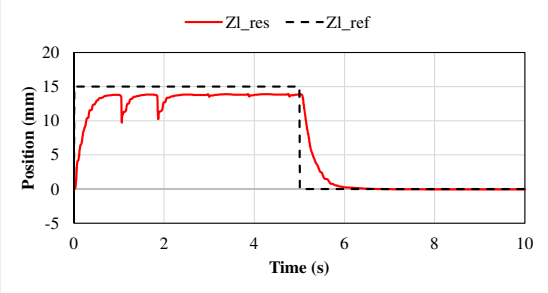

(a) Position of low-speed mover under pulse command.

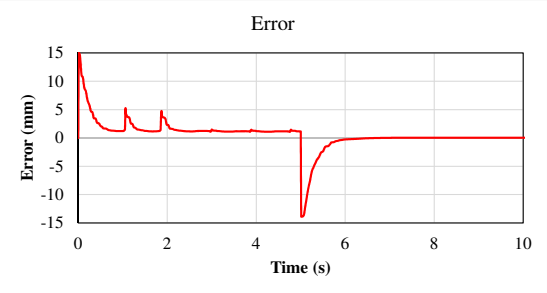

(b) Tracking error under pulse command.

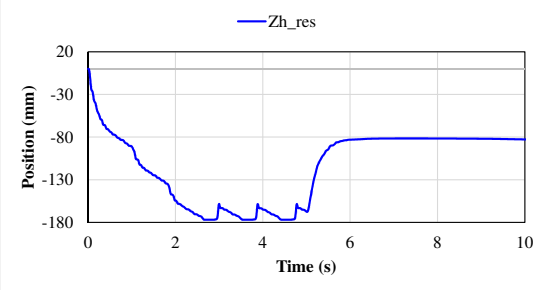

(c) Position of high-speed mover under pulse command.

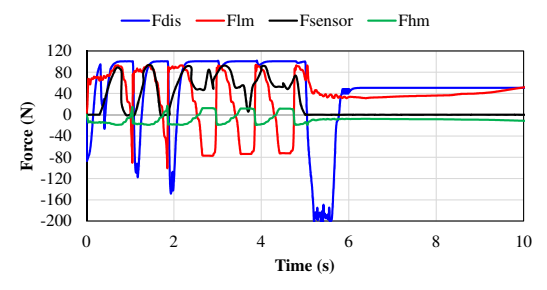

(d) Estimated force under pulse command.

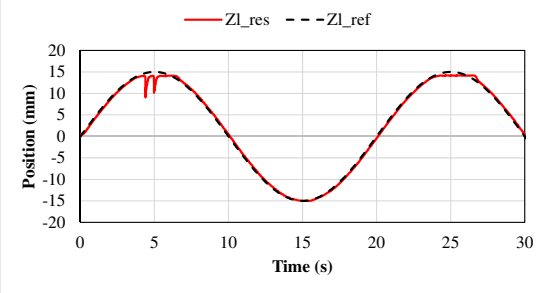

(e) Position of low-speed mover under sine command.

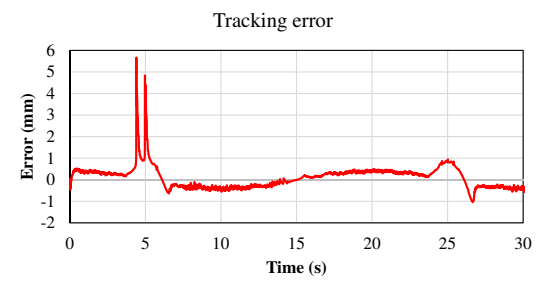

(f) Tracking error under sine command.

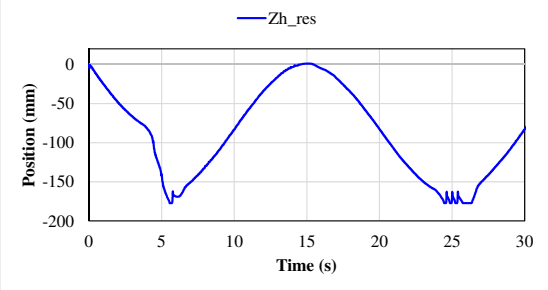

(g) Position of high-speed mover under pulse command.

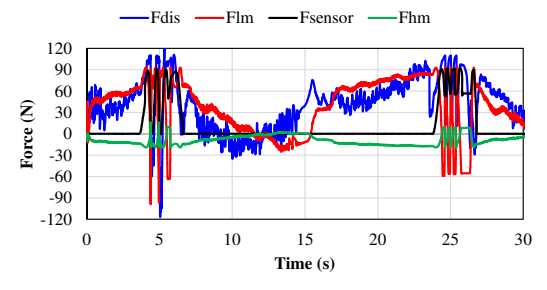

(h) Estimated force under sine command.

Figure 4.9: Experimental results when mover contacts to an obstacle.

4.6.3 Frequency Analysis

This section evaluates frequency analysis of the controller and the magnetic gear. Fig. 4.10a shows opened-loop bode diagram from reference to response displacement of low-speed mover. It can be observed that gain and phase margins are equal to around 6.5 dB and 45 degree, respectively. From the result, the both gain and phase margins are greater than zero, proves that the controller is stable.

Fig. 4.10b illustrates closed-loop Bode plot from command to response positions of the low-speed mover. At low frequency (less than 0.4 Hz), response value is very closes to reference value in the amplitude (magnitude approximates to 0 dB). Then, the magnitude slightly decreases when the frequency increases, reaching resonance around 4.5 Hz before increasing back. The same phenomenon occurs in phase-shift value.

Bode plot from displacement of high-speed mover to displacement of low-speed mover is shown in Fig. 4.10c. This result shows that the gear ratio G_r of the MG slightly increases from ideal value, approximate 5.33 (magnitude $\approx 20\log(1/G_r) \approx -14.54$ dB), to approximate 6.38 (magnitude ≈ -16.1 dB) when input frequency increases from 0.3 to 7.1 Hz, respectively. Then, magnitude significantly decrease when in frequency greater than 7.1 Hz. From this results, the maximal velocity of the movers can be estimated as $V_h = 28.4$ mm/s and $V_l = 4.45$ mm/s.

The Bode diagrams focus on analyzing frequency response of the mover's displacement (mechanical system), therefore frequency domain is in lower range than it in electronics system.

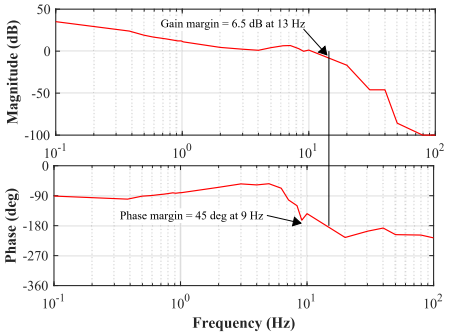

(a) Bode diagram of opened loop from Zl_{ref} to Zl_{res}.

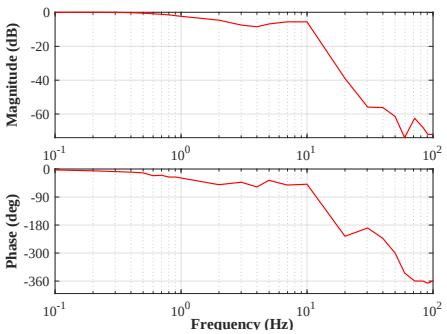

(b) Bode diagram of closed loop from Zl_{ref} to Zl_{res}.

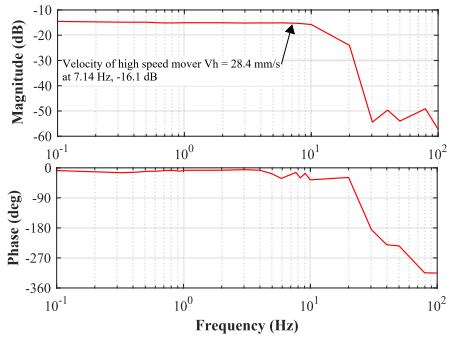

(c) Bode diagram of the gear from Zh_{res} to Zl_{res}.

Figure 4.10: Frequency characteristics.

4.7 Summary

This chapter presented a solution for modeling of a high thrust tubular magnetic geared linear motor aims to control the motor position. The motor's model established on the motion equation of the two movers. In comparison with traditional linear motors which have only one mover, there are reaction forces between the low-speed and high-speed movers. This reaction force was estimated basing on the difference position of the movers. In addition, a motion controller was developed by comparing PI and DOB methods. From simulation and experimental results, it was verified that the motor model is accurately. Effectiveness of the controller was confirmed by experimental results under both cases of pulse and sinusoidal references. Furthermore, frequency analysis of the controller and magnetic gear were investigated. However, there was a slight difference when estimated reaction forces.

Chapter 5

Conclusion and Future Work

5.1 Conclusions

The main contributions of this dissertation are:

- Newly establish a method to predict flux density distribution in high thrust force tubular magnetic geared linear motor.
- A solution for mathematical modeling of the motor which aims to control the motor position was developed.

In detail, chapter 3 presented a mathematical solution for calculating the flux density distributions in a tubular MGLM that generates a high thrust force. Using a 2-D model, the Laplace and Poisson equations were solved in cylindrical coordinates to predict the magnetic flux density distributions. The method consumes significantly less computing time than the finite element method and provides both axial and radial components of magnetic flux in comparison with previous methods. The force transmission capacity and thrust force were also calculated. The predicted results can be used as a simple tool for optimization geometrical parameters of the motor. The calculation, analysis, and experimental results show that the established method is suitable for predicting the flux density distribution in a tubular MGLM. However, there is a small difference between the experimental and calculated results because of the manufacturing factors of the motor.

Chapter 4 presented a solution for modeling a high-thrust tubular magnetic linear gear motor for the purpose of controlling the motor position. A controller was also developed by comparing the PI and DOB methods. Simulation and experimental results confirmed the accuracy of the motor model. The effectiveness of the controller was confirmed by both cases of pulse and sinusoidal references. Furthermore, the frequency analysis of the controller and magnetic gear was examined. However, there was a slight difference in the estimated reaction forces.

The motor expects to replace the traditional linear motor in the linear system which required high thrust, reduce the maintenance and extend the life such as small injection molding machines or medical assistance devices. In this stage, the presented motor is at the first step to be applied to real systems. The motor geometrical parameters, speed capacity, stroke length, and suitable controller must further study.

5.2 Future Work

This dissertation has described a solution for magnetic flux density distribution in a tubular magnetic gear and basic control the tubular magnetic geared linear motor. However, it is difficult to consider all the faced technical issues during the PhD program. Hence, the future work recommendation is as follows:

- The calculation method in this study is established when neglected magnetic saturation. To achieve higher flux density, magnetic material probably operates in saturation zone because of non-linear $B - H$ curve. If saturation occurs in pole-pieces (magnetic material), the resultant relative permeability is not a constant but a function of the movers displacement $\mu_r(z)$ or a function of the magnetic flux strength H. This complicate issue needs further study.

- The topology and test experimental of TMGLM as one of a potential solution for a high force density linear actuator system, the challenge is to make sure the structural integrity, manufacture ability, and satisfy the performance through comprehensive tests.

- This study mainly focuses on analysis of static characteristics. However, as the motivation component of a high thrust force density actuator in linear systems, the motor has to obtained not only high thrust force but also desirable dynamics to satisfy the requirements of suitable fields application. Thus, dynamic performance analysis of the TMGLM needs further research and experimental tests.

- Complicate issues such as vibration, friction in mechanical components, harmonic noise, losses, and end effect have not been conducted.

- In order to achieve high performance, it is necessary to investigate a comprehensive assessment and global optimization based the multi-physical field analysis.

- Magnetic gear in general can overcome overload circumstances. In this situation, the two movers/rotors will slide together. This phenomenon probably not so serious in rotary magnetic gear. However, overload circumstances maybe dangerous because of limited stroke length in the case of linear structure. This issue also need to further research.

Related Publications

Journal Paper

- Nguyen Duc Khuong, Tomoyuki Shimono, "Modeling, Analysis, and Experimental Validation of Magnetic Geared Linear Motor", *IEEJ Journal of Industry Applications*, DOI: 10.1541/ieejjia.22007992, Vol.12, no.03, pp.475-483, Jan. 2023

Conference Paper

- Nguyen Duc Khuong, Tomoyuki Shimono, "Modeling and Analysis of a Magnetic Geared Linear Motor", in proc. *The 2022 International Power Electronics Conference (IPEC2022)*, 16C2-3, Himeji, Japan, May. 2022

Bibliography

[1] J.-M. Jo, J.-H. Lee, Y.-J. Han, C.-Y. Lee, and K.-S. Lee, "Development of propulsion inverter control system for high-speed maglev based on long stator linear synchronous motor," *Energies*, vol. 10, no. 2, p. 170, 2017.

[2] M. Shujun, C. Jianyun, S. Xudong, and W. Shanming, "A variable pole pitch linear induction motor for electromagnetic aircraft launch system," *IEEE Transactions on Plasma Science*, vol. 43, no. 5, pp. 1346–1351, 2015.

[3] L. Lu, Z. Chen, B. Yao, and Q. Wang, "Desired compensation adaptive robust control of a linear-motor-driven precision industrial gantry with improved cogging force compensation," *IEEE/ASME Transactions on Mechatronics*, vol. 13, no. 6, pp. 617–624, 2008.

[4] M. Mutluer, "A new approach to increase the thrust force of tubular linear voice coil motor," *IEEE Canadian Journal of Electrical and Computer Engineering*, vol. 44, no. 4, pp. 509–515, 2021.

[5] C. Luo, Z. Lin, and J. Sun, "Design of linear voice coil motor with semi-closed structure," *IET Electric Power Applications*, vol. 13, no. 10, pp. 1574–1579, 2019.

[6] N. Baloch, S. Khaliq, and B.-I. Kwon, "A high force density hts tubular vernier machine," *IEEE Transactions on Magnetics*, vol. 53, no. 11, pp. 1–5, 2017.

[7] Z. Q. Zhu and X. Chen, "Analysis of an e-core interior permanent magnet linear oscillating actuator," *IEEE Transactions on Magnetics*, vol. 45, no. 10, pp. 4384–4387, 2009.

[8] X. Chen and Z. Q. Zhu, "Analytical determination of optimal split ratio of e-core permanent magnet linear oscillating actuators," *IEEE Transactions on Industry Applications*, vol. 47, no. 1, pp. 25–33, 2011.

[9] Z. Liu, W. Zhao, J. Ji, and Q. Chen, "A novel double-stator tubular vernier permanent-magnet motor with high thrust density and low cogging force," *IEEE Transactions on Magnetics*, vol. 51, no. 7, pp. 1–7, 2015.

[10] J. Ji, S. Yan, W. Zhao, G. Liu, and X. Zhu, "Minimization of cogging force in a novel linear permanent-magnet motor for artificial hearts," *IEEE Transactions on Magnetics*, vol. 49, no. 7, pp. 3901–3904, 2013.

[11] J. Ji, J. Zhao, W. Zhao, Z. Fang, G. Liu, and Y. Du, "New high force density tubular permanent-magnet motor," *IEEE transactions on applied superconductivity*, vol. 24, no. 3, pp. 1–5, 2013.

[12] L. Yan, L. Zhang, T. Wang, Z. Jiao, C.-Y. Chen, and I.-M. Chen, "Magnetic field of tubular linear machines with dual halbach array," *Progress In Electromagnetics Research*, vol. 136, pp. 283–299, 2013.

[13] T. Lubin, S. Mezani, and A. Rezzoug, "Development of a 2-d analytical model for the electromagnetic computation of axial-field magnetic gears," *IEEE Transactions on Magnetics*, vol. 49, no. 11, pp. 5507–5521, 2013.

[14] B. Praslicka, M. C. Gardner, M. Johnson, and H. A. Toliyat, "Review and analysis of coaxial magnetic gear pole pair count selection effects," *IEEE Journal of Emerging and Selected Topics in Power Electronics*, 2021.

[15] S. Niu, S. L. Ho, and W. Fu, "Performance analysis of a novel magnetic-geared tubular linear permanent magnet machine," *IEEE transactions on magnetics*, vol. 47, no. 10, pp. 3598–3601, 2011.

[16] S. Niu, S. L. Ho, and W. Fu, "Performance analysis of a novel magnetic-geared tubular linear permanent magnet machine," *IEEE transactions on magnetics*, vol. 47, no. 10, pp. 3598–3601, 2011.

[17] R. C. Holehouse, K. Atallah, and J. Wang, "A linear magnetic gear," in *2012 XXth International Conference on Electrical Machines*, pp. 563–569. IEEE, 2012.

[18] T. Lubin, S. Mezani, and A. Rezzoug, "Analytical computation of the magnetic field distribution in a magnetic gear," *IEEE Transactions on magnetics*, vol. 46, no. 7, pp. 2611–2621, 2010.

[19] L. Jian and K. Chau, "A coaxial magnetic gear with halbach permanent-magnet arrays," *IEEE Transactions on Energy conversion*, vol. 25, no. 2, pp. 319–328, 2010.

[20] L. Jian and K. Chau, "A coaxial magnetic gear with halbach permanent-magnet arrays," *IEEE Transactions on Energy conversion*, vol. 25, no. 2, pp. 319–328, 2010.

[21] G. Ruiz-Ponce, M. A. Arjona, C. Hernandez, and R. Escarela-Perez, "A review of magnetic gear technologies used in mechanical power transmission," *Energies*, vol. 16, no. 4, p. 1721, 2023.

[22] H. T. Faus, "Magnet gearing," May 27 1941, uS Patent 2,243,555.

[23] K. Ikuta, S. Makita, and S. Arimoto, "Non-contact magnetic gear for micro transmission mechanism," in *[1991] Proceedings. IEEE Micro Electro Mechanical Systems*, pp. 125–130. IEEE, 1991.

[24] X. Li, K.-T. Chau, M. Cheng, and W. Hua, "Comparison of magnetic-geared permanent-magnet machines," *Progress In Electromagnetics Research*, vol. 133, pp. 177–198, 2013.

[25] M. Baermann, "Magnetic worm drive," Jun. 4 1974, uS Patent 3,814,962.

[26] S. Kikuchi and K. Tsurumoto, "Design and characteristics of a new magnetic worm gear using permanent magnet," *IEEE Transactions on magnetics*, vol. 29, no. 6, pp. 2923–2925, 1993.

[27] K. Tsurumoto, "Improvement of the transmitted torque characteristics of a magnetic bevel gear. jiki kasa haguruma no dentatsu toruku tokusei kaizen ni kansuru kosatsu," *Nippon Oyo Jiki Gakkai-Shi;(Japan)*, vol. 18, no. 2, 1994.

[28] G.-H. Jang, C.-W. Kim, S.-W. Seo, K.-H. Shin, I.-J. Yoon, and J.-Y. Choi, "Torque characteristic analysis and measurement of magnetic rack–pinion gear based on analytical method," *IEEE Transactions on Magnetics*, vol. 55, no. 7, pp. 1–5, 2019.

[29] K. Tsurumoto and Y. Tanaka, "Prototype production of new magnetic planetary and differential gears and performance," *JOURNAL-MAGNETICS SOCIETY OF JAPAN*, vol. 26, no. 4, pp. 703–706, 2002.

[30] C.-C. Huang, M.-C. Tsai, D. G. Dorrell, and B.-J. Lin, "Development of a magnetic planetary gearbox," *IEEE Transactions on Magnetics*, vol. 44, no. 3, pp. 403–412, 2008.

[31] K. Atallah and D. Howe, "A novel high-performance magnetic gear," *IEEE Transactions on magnetics*, vol. 37, no. 4, pp. 2844–2846, 2001.

[32] S. Gerber, "Evaluation and design aspects of magnetic gears and magnetically geared electrical machines," Ph.D. dissertation, Stellenbosch: Stellenbosch University, 2015.

[33] M. C. Gardner, M. Johnson, and H. A. Toliyat, "Comparison of surface permanent magnet coaxial and cycloidal radial flux magnetic gears," in *2018 IEEE Energy Conversion Congress and Exposition (ECCE)*, pp. 5005–5012. IEEE, 2018.

[34] L. Jian, K. Chau, Y. Gong, J. Jiang, C. Yu, and W. Li, "Comparison of coaxial magnetic gears with different topologies," *IEEE Transactions on magnetics*, vol. 45, no. 10, pp. 4526–4529, 2009.

[35] X. Li, K. Chau, M. Cheng, W. Hua, and Y. Du, "An improved coaxial magnetic gear using flux focusing," in *2011 International Conference on electrical machines and systems*, pp. 1–4. IEEE, 2011.

[36] K. Atallah, J. Wang, and D. Howe, "A high-performance linear magnetic gear," *Journal of Applied Physics*, vol. 97, no. 10, p. 10N516, 2005.

[37] K. Atallah, S. Calverley, and D. Howe, "Design, analysis and realisation of a high-performance magnetic gear," *IEE Proceedings-Electric Power Applications*, vol. 151, no. 2, pp. 135–143, 2004.

[38] R. C. Holehouse, K. Atallah, and J. Wang, "Design and realization of a linear magnetic gear," *IEEE transactions on magnetics*, vol. 47, no. 10, pp. 4171–4174, 2011.

[39] W. Li, K. Chau, and J. Jiang, "Application of linear magnetic gears for pseudo-direct-drive oceanic wave energy harvesting," *IEEE Transactions on Magnetics*, vol. 47, no. 10, pp. 2624–2627, 2011.

[40] N. Feng, H. Yu, L. Huang, W. Zhong, and Z. Shi, "Performance analysis of a magnetic-geared linear permanent magnet generator for wave energy conversion," in *2015 IEEE International Magnetics Conference (INTERMAG)*, pp. 1–1. IEEE, 2015.

[41] W. Li, K. Chau, C. H. Lee, T. Ching, M. Chen, and J. Jiang, "A new linear magnetic gear with adjustable gear ratios and its application for direct-drive wave energy extraction," *Renewable Energy*, vol. 105, pp. 199–208, 2017.

[42] C. Liu, H. Zhu, R. Dong, S. Zhou, and L. Huang, "Sensitivity analysis and optimal design of a linear magnetic gear for direct-drive wave energy conversion," *IEEE Access*, vol. 7, pp. 73 983–73 992, 2019.

[43] S. Mezani, K. Atallah, and D. Howe, "A high-performance axial-field magnetic gear," *Journal of applied physics*, vol. 99, no. 8, p. 08R303, 2006.

[44] P. O. Rasmussen, T. O. Andersen, F. T. Jorgensen, and O. Nielsen, "Development of a high-performance magnetic gear," *IEEE transactions on industry applications*, vol. 41, no. 3, pp. 764–770, 2005.

[45] K. K. Uppalapati, M. D. Calvin, J. D. Wright, J. Pitchard, W. B. Williams, and J. Z. Bird, "A magnetic gearbox with an active region torque density of 239 n· m/l," *IEEE Transactions on Industry Applications*, vol. 54, no. 2, pp. 1331–1338, 2017.

[46] K. Halbach, "Design of permanent multipole magnets with oriented rare earth cobalt material," *Nuclear instruments and methods*, vol. 169, no. 1, pp. 1–10, 1980.

[47] J.-S. Choi and J. Yoo, "Design of a halbach magnet array based on optimization techniques," *IEEE Transactions on Magnetics*, vol. 44, no. 10, pp. 2361–2366, 2008.

[48] T. Fujita, Y. Ando, K. Nagaya, M. Oka, T. Todaka, M. Enokizono, and K. Sugiura, "Surface magnet gears with a new magnet arrangement and optimal shape of stationary pole pieces," 2013.

[49] D. Som, K. Li, J. Kadel, J. Wright, S. Modaresahmadi, J. Z. Bird, and W. William, "Analysis and testing of a coaxial magnetic gearbox with flux concentration halbach rotors," *IEEE Transactions on Magnetics*, vol. 53, no. 11, pp. 1–6, 2017.

[50] X. Liu, K. Chau, J. Jiang, and C. Yu, "Design and analysis of interior-magnet outer-rotor concentric magnetic gears," *Journal of applied physics*, vol. 105, no. 7, p. 07F101, 2009.

[51] J.-X. Shen, H.-Y. Li, H. Hao, and M.-J. Jin, "A coaxial magnetic gear with consequent-pole rotors," *IEEE Transactions on Energy Conversion*, vol. 32, no. 1, pp. 267–275, 2016.

[52] L. Jing, J. Gong, Z. Huang, T. Ben, and Y. Huang, "A new structure for the magnetic gear," *IEEE Access*, vol. 7, pp. 75 550–75 555, 2019.

[53] N. W. Frank and H. A. Toliyat, "Analysis of the concentric planetary magnetic gear with strengthened stator and interior permanent magnet inner rotor," *IEEE transactions on industry applications*, vol. 47, no. 4, pp. 1652–1660, 2011.

[54] N. W. Frank, S. Pakdelian, and H. A. Toliyat, "Passive suppression of transient oscillations in the concentric planetary magnetic gear," *IEEE transactions on energy conversion*, vol. 26, no. 3, pp. 933–939, 2011.

[55] A. Abdel-Khalik, S. Ahmed, and A. Massoud, "A bearingless coaxial magnetic gearbox," *Alexandria Engineering Journal*, vol. 53, no. 3, pp. 573–582, 2014.

[56] Y. Liu, S. L. Ho, and W. Fu, "A novel magnetic gear with intersecting axes," *IEEE Transactions on Magnetics*, vol. 50, no. 11, pp. 1–4, 2014.

[57] K. Aiso, K. Akatsu, and Y. Aoyama, "A novel reluctance magnetic gear for high-speed motor," *IEEE Transactions on Industry Applications*, vol. 55, no. 3, pp. 2690–2699, 2019.

[58] L. Yong, X. Jingwei, P. Kerong, and L. Yongping, "Principle and simulation analysis of a novel structure magnetic gear," in *2008 International Conference on Electrical Machines and Systems*, pp. 3845–3849. IEEE, 2008.

[59] S. Pakdelian, N. W. Frank, and H. A. Toliyat, "Analysis and design of the trans-rotary magnetic gear," in *2012 IEEE Energy Conversion Congress and Exposition (ECCE)*, pp. 3340–3347. IEEE, 2012.

[60] S. Pakdelian, Y. Deshpande, and H. A. Toliyat, "An electric machine integrated with trans-rotary magnetic gear," in *2012 IEEE Energy Conversion Congress and Exposition (ECCE)*, pp. 3356–3362. IEEE, 2012.

[61] S. Pakdelian and H. A. Toliyat, "Design aspects of the trans-rotary magnetic gear," in *IECON 2012-38th Annual Conference on IEEE Industrial Electronics Society*, pp. 1720–1725. IEEE, 2012.

[62] S. Pakdelian, N. W. Frank, and H. A. Toliyat, "Principles of the trans-rotary magnetic gear," *IEEE transactions on magnetics*, vol. 49, no. 2, pp. 883–889, 2012.

[63] J. Rens, R. Clark, S. Calverley, K. Atallah, and D. Howe, "Design, analysis and realization of a novel magnetic harmonic gear," in *2008 18th International Conference on Electrical Machines*, pp. 1–4. IEEE, 2008.

[64] J. Rens, K. Atallah, S. D. Calverley, and D. Howe, "A novel magnetic harmonic gear," *IEEE Transactions on Industry Applications*, vol. 46, no. 1, pp. 206–212, 2009.

[65] T. Andersen, F. Joergensen, and P. Rasmussen, "The cycloid permanent magnetic gear," in *IEEE Industial Applications Conference*, vol. 1, pp. 373–378, 2006.

[66] W. Li, K. Chau, and J. Li, "Simulation of a tubular linear magnetic gear using hts bulks for field modulation," *IEEE Transactions on Applied Superconductivity*, vol. 21, no. 3, pp. 1167–1170, 2010.

[67] J. Wang, G. W. Jewell, and D. Howe, "A general framework for the analysis and design of tubular linear permanent magnet machines," *IEEE Transactions on Magnetics*, vol. 35, no. 3, pp. 1986–2000, 1999.

[68] B. Gysen, K. Meessen, J. Paulides, and E. Lomonova, "General formulation of the electromagnetic field distribution in machines and devices using fourier analysis," *IEEE Transactions on Magnetics*, vol. 46, no. 1, pp. 39–52, 2009.

[69] J. Wang, D. Howe, and G. W. Jewell, "Fringing in tubular permanent-magnet machines: Part i. magnetic field distribution, flux linkage, and thrust force," *IEEE Transactions on Magnetics*, vol. 39, no. 6, pp. 3507–3516, 2003.

[70] J. Wang, G. Jewell, and D. Howe, "Design optimisation and comparison of tubular permanent magnet machine topologies," *IEE Proceedings-Electric Power Applications*, vol. 148, no. 5, pp. 456–464, 2001.

[71] J. Wang and D. Howe, "Tubular modular permanent-magnet machines equipped with quasi-halbach magnetized magnets-part ii: armature reaction and design optimization," *IEEE Transactions on Magnetics*, vol. 41, no. 9, pp. 2479–2489, 2005.

[72] J. Luo, B. Kou, X. Yang, H. Zhang, and L. Zhang, "Development, design, and analysis of a dual-consequent-pole transverse flux linear machine for direct-drive applications," *IEEE Transactions on Industrial Electronics*, vol. 68, no. 7, pp. 6097–6108, 2020.

[73] Y. Fujimoto, T. Mikami, and T. Suzuki, "Position and force control of spm-type high-thrust-force linear motor for assistive devices," in *2013 IEEE Region 10 Humanitarian Technology Conference*, pp. 23–28. IEEE, 2013.

[74] M. Zhao, Y. Wei, H. Yang, M. Xu, F. Han, G. Deng, D. Hou, and P. Zhang, "Development and analysis of novel flux-switching transverse-flux permanent magnet linear machine," *IEEE Transactions on Industrial Electronics*, vol. 66, no. 6, pp. 4923–4933, 2018.

[75] "Jmag version 20.1 user's manual (iron loss formulas)."

[76] S.-Y. Chen, H.-H. Chiang, T.-S. Liu, and C.-H. Chang, "Precision motion control of permanent magnet linear synchronous motors using adaptive fuzzy fractional-order sliding-mode control," *IEEE/ASME Transactions on Mechatronics*, vol. 24, no. 2, pp. 741–752, 2019.

[77] N. D. Khuong and T. Shimono, "Modeling and analysis of a magnetic geared linear motor," in *The 2022 International Power Electronics Conference (IPEC-Himeji -ECCE Asia-)*, pp. 260–267. IEEJ, 2022.